Impact of doping conditions on the Fermi level in lead-free antiferroelectrics

Zur Erlangung des akademischen Grades Doctor rerum naturalium (Dr. rer. nat.)
genehmigte Dissertation vorgelegt
von Lorenzo Villa
geboren in Mailand

Fachgebiet: Materialmodellierung
Fachbereich: Material- und Geowissenschaften
Technische Universität Darmstadt

Berichterstatter: Prof. Dr. rer. nat. Karsten Albe,
Technische Universität Darmstadt
Mitberichterstatter: Dr. Jürgen Spitaler
Materials Center Leoben Forschungs GmbH, Österreich
1. Prüfer: Prof. Dr. Jan Philipp Hofmann
Technische Universität Darmstadt
2. Prüfer: Prof. Dr. rer. nat. Wolfgang Donner,
Technische Universität Darmstadt

Tag der Einreichung: 09.05.2023
Tag der Prüfung: 26.07.2023
Jahr der Veröffentlichung: 2023

Darmstadt 2023

Please cite this document as:
URN: urn:nbn:de:tuda-tuprints-244811
URL: https://tuprints.ulb.tu-darmstadt.de/id/eprint/24481

Villa, Lorenzo: Impact of doping conditions on the Fermi level in lead-free antiferroelectrics
Darmstadt, Technische Universität Darmstadt
Jahr der Veröffentlichung auf TUprints: 2023
URN: urn:nbn:de:tuda-tuprints-244811
URL: https://tuprints.ulb.tu-darmstadt.de/id/eprint/24481
Tag der mündlichen Prüfung: 26.07.2023

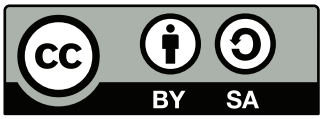

Erklärung laut Promotionsordnung

§8 Abs. 1 lit. c PromO

Ich versichere hiermit, dass die elektronische Version meiner Dissertation mit der schriftlichen Version übereinstimmt.

§8 Abs. 1 lit. d PromO

Ich versichere hiermit, dass zu einem vorherigen Zeitpunkt noch keine Promotion versucht wurde. In diesem Fall sind nähere Angaben über Zeitpunkt, Hochschule, Dissertationsthema und Ergebnis dieses Versuchs mitzuteilen.

§9 Abs. 1 PromO

Ich versichere hiermit, dass die vorliegende Dissertation selbstständig und nur unter Verwendung der angegebenen Quellen verfasst wurde.

§9 Abs. 2 PromO

Die Arbeit hat bisher noch nicht zu Prüfungszwecken gedient.

Darmstadt, September 6, 2023

Lorenzo Villa

Abstract

Extended research, aimed at improving the properties of dielectric capacitors for energy storage applications, has fostered the interest in antiferroelectric (AFE) materials. In this class of materials, sodium niobate ($NaNbO_3$, NN) and silver niobate ($AgNbO_3$, AN) are amongst the most promising alternatives to the toxic lead-containing compounds, such as $PbZrO_3$-based ceramics, due to the possibility to obtain double *P-E* loops at room temperature. Chemical modification has been extensively used in order to improve their antiferroelectric properties and energy efficiency. However, the defect chemistry and its connection with the AFE properties are still unknown, and a systematic approach for doping these systems is still missing. Moreover, while processing conditions and kinetics are known to play a role in the final properties of the material, their impact has not yet been systematically studied. Lastly, when impurities are introduced into a system, they will interact with the already present intrinsic defects and can lead to formation of defect dipoles, which will affect the switching behaviour of the electric dipoles and therefore the *P-E* loops. Nonetheless, their presence induced by doping has not yet been investigated.
The scope of this doctoral thesis is therefore to study with first-principles calculations the thermodynamics of point defects in NN and AN. We investigate with density functional theory (DFT) how doping and synthesis conditions modify the electronic properties of NN and AN, with focus on the Fermi level. In particular, we determine the thermodynamic defect equilibrium by solving the charge neutrality condition, accounting for the impact of extrisic defects on the compensation mechanisms. Moreover, we develop a novel scheme to account for quenching of defects within the established point defect thermodynamics.
In pure NN, the acceptor Na vacancies and donor O vacancies are present in large concentrations, thus dictating the position of the Fermi level. When doped with Sr and Sn, at high temperature and low oxygen partial pressure (p_{O_2}) NN is an n-type semiconductor, while for high p_{O_2} the system becomes p-type. At room temperature the material is p-type. Quenching from high temperature all defects, or just O vacancies, shifts the Fermi level towards the conduction band minimum (CBM), while quenching Na and Nb vacancies produces a less pronounced shift towards the valence band maximum (VBM). Four defect complexes are found to be stable and present in high concentrations. This suggests they play an important role in the field switching mechanism, ultimately influencing the AFE *P-E* loops.

In AN, the formation energies of the acceptor Ag vacancies are so low that the semiconductor is always p-type. For extremely low p_{O_2}, the material is found to be unstable due to the unphysically high concentration of Ag vacancies, which matches the experimental results reported in the literature. Doping with Mn and/or quenching does not produce a significant shift of the Fermi level, and the system remains p-type in all conditions.
In summary, our approach allows to systematically study defect thermodynamics and electronic properties in semiconductors, accounting for multiple compensation mechanisms as well as quenched defects that are motivated by the synthesis conditions.

Zusammenfassung

Antiferroelektrische (AFE) Materialien finden Einsatz in dielektrischen Kondensatoren mit hohen Energiedichten und -effizienzen, da sie doppelte *P-E*-Schleifen bei Raumtemperatur aufweisen. In dieser Materialklasse stellen Natriumniobat ($NaNbO_3$, NN) und Silberniobat ($AgNbO_3$, AN) die vielversprechendsten Alternativen zu toxischen bleihaltigen Verbindungen, wie zum Beispiel $PbZrO_3$-basierten Keramiken, dar. Chemische Modifikationen wurden umfangreich genutzt, um die antiferroelektrischen Eigenschaften und Energieeffizienz dieser Materialien zu verbessern. Die Defektchemie und ihre Verbindung zu den AFE-Eigenschaften sind jedoch weitestgehend unbekannt und ein systematischer Ansatz zur Dotierung in diesen Systemen fehlt bisher. Ebenso wurden die Auswirkungen von Prozessbedingungen und kinetischen Aspekten auf die endgültigen Eigenschaften des Materials noch nicht systematisch erfasst. Außerdem können die in das System eingeführten Verunreinigungen mit den bereits vorhandenen intrinsischen Defekten interagieren und zur Bildung von Defektdipolen führen, welche das Schaltverhalten der elektrischen Dipole und damit die *P-E*-Schleifen beeinflussen. Trotzdem wurden Defektdipole in bleifreien Antiferroelektrika noch nicht untersucht.

Das Ziel dieser Doktorarbeit ist es, die Thermodynamik von Punktdefekten in NN und AN mithilfe von first-principles Methoden zu untersuchen. Dazu werden Berechnungen basierend auf der Dichtefunktionaltheorie angewandt, um die Auswirkungen von Dotierung und Synthesebedingungen auf die elektronischen Eigenschaften von NN und AN zu analysieren, insbesondere mit Fokus auf das Fermi-Niveau. Dabei bestimmen wir das thermodynamische Defektgleichgewicht durch Lösung der Ladungsneutralitätsbedingung und berücksichtigen die Auswirkungen von extrinsischen Defekten auf die Kompensationsmechanismen. Darüber hinaus entwickeln wir ein neuartiges Verfahren innerhalb der etablierten Punktdefekt-Thermodynamik, das das Einfrieren von Defekten berücksichtigt.

Mit diesem Ansatz zeigen wir, dass in reinem NN Na-Vakanzen (Akzeptoren) und O-Vakanzen (Donatoren) in hohen Konzentrationen vorhanden sind und die Position des Fermi-Niveaus bestimmen. Bei Dotierung mit Sr und Sn ist NN bei hohen Temperaturen und niedrigem Sauerstoffpartialdruck n-leitend, während das System bei hohem Sauerstoffpartialdruck p-leitend wird. Bei Raumtemperatur ist das Material p-leitend. Das Einfrieren aller Defekte oder nur der O-Vakanzen bei hoher Temperatur verschiebt das Fermi-Niveau in Richtung des

Leitungsbandmaximums (engl. conduction band minimum, CBM), während das Einfrieren der Na- und Nb-Vakanzen eine weniger ausgeprägte Verschiebung in Richtung des Valenzbandmaximums (engl. valence band maximum, VBM) bewirkt. Vier Defektkomplexe stellen sich als stabil heraus und sind demnach in hohen Konzentrationen vorhanden. Dies legt nahe, dass sie eine wichtige Rolle im Schaltverhalten der Polarisation spielen und letztendlich die AFE *P-E*-Schleifen beeinflussen.
In AN sind die Bildungsenergien der Ag-Vakanzen (Akzeptoren) so niedrig, dass das Halbleitermaterial immer p-leitend ist. Bei extrem niedrigem Sauerstoffpartialdruck ist das Material aufgrund der unrealistisch hohen Konzentration an Ag-Vakanzen instabil, was mit den in der Literatur beschriebenen experimentellen Ergebnissen übereinstimmt. Die Dotierung mit Mn und/oder das Einfrieren führen nicht zu einer signifikanten Verschiebung des Fermi-Niveaus, und das System bleibt unter allen Bedingungen p-leitend.
Zusammengefasst ermöglicht unser Ansatz die systematische Untersuchung der Defektthermodynamik sowie der elektronischen Eigenschaften von Halbleitern, unter der Berücksichtigung einer Vielzahl von Kompensationsmechanismen und des Einfrierens von Defekten, welches durch die Synthesebedingungen motiviert wird.

Acknowledgements

Firstly, I would like to thank Prof. Dr. Karsten Albe for the chance he has given me. I have learned a lot during these years, both from a scientific and personal point of view. Without you, this work would have not been possible.
Special thanks go to Dr. Jürgen Spitaler, who volunteered his time and expertise to co-referee this thesis. I would also like to thank the other two members of the commission, Prof. Dr. Wolfgang Donner and Prof. Dr. Jan Philipp Hofmann.
Thanks to Dr. Elaheh Ghorbani for assisting and guiding me, especially at the beginning of this research.
Thanks to my colleagues in the Materials Modelling group, who have accompained me daily on this journey. We shared lots of good moments, both inside and outside of work.
Thanks to my colleagues in the FLAME project, for many useful scientific discussions, especially during frustrating times, and for all the fun during our trips.
Thanks to my friends in Germany, you have made me feel included from the start. You are one of the main reasons why moving to Darmstadt was a great decision.
Thanks to my friends in Italy, you are a part of who I am, even though we are not so geographically close anymore. Seeing you has made all the 7 am flights I took to visit worth it.
Thanks to my teammates at Darmstädter TSG 1846. You have made me feel a part of the team from the first day. We always share good moments both inside and outside the pitch, which give another flavour to my week. Also, I would not have learned german without you.
Special thanks to Sabine, for being always by my side and a constant support. You patiently listen to my rants when I am frustrated, you always give me fresh points of view and good advice, and you have always improved my days, even the worst ones.
Last, but absolutely not least, thanks to my family, especially to my parents Claudia and Giorgio. You gave me all the possibilities I could ask for. You gave me guidance and encouraged me to go through my studies and make new experiences, always without pressuring me. Without you, I would not be the man I am today.

Contents

1 Introduction to Antiferroelectricity

The aim of this chapter is to provide the scientific background and motivation of this doctoral thesis. Firstly, since this research is focused on antiferroelectric materials for applications in the field of energy storage, we present their definition and properties, with particular focus on the features which make them suitable and promising candidates for energy storage applications. Secondly, we review the current state-of-the-art approaches for doping antiferroelectric materials, with an emphasis on their successes in improving energy storage properties, as well as their shortcomings. Lastly, we summarize the open scientific questions, a hope to provide a transparent view of the scientific problems that are still unsolved, and a clear motivation behind this doctoral thesis.

1.1 Dielectric Capacitors for Energy Storage

In the modern world, storing energy is just as important as producing it. Because of the ever-increasing demand for smaller and lighter electronic devices, the development of advanced energy storage materials and associated technologies have long been areas of intense research interest for both the academic and industry communities. Fuel cells, Li-ion batteries, electrochemical capacitors, and dielectric capacitors have been regarded as the most promising four devices.[1] The relationship between energy storage density (ESD) and power density (PD) for the four devices is illustrated in Figure 1.1. Batteries are capable of converting electrical energy into chemical energy and typically possess the higher energy density ($\approx$ 100 Wh/Kg).[2] At the same time, however, they typically display limited electrical power output, due to the much slower movement of the charge carriers involved. Capacitors, on the other hand, can release stored charge within an extremely short time duration (<100 ns), thus creating very large currents

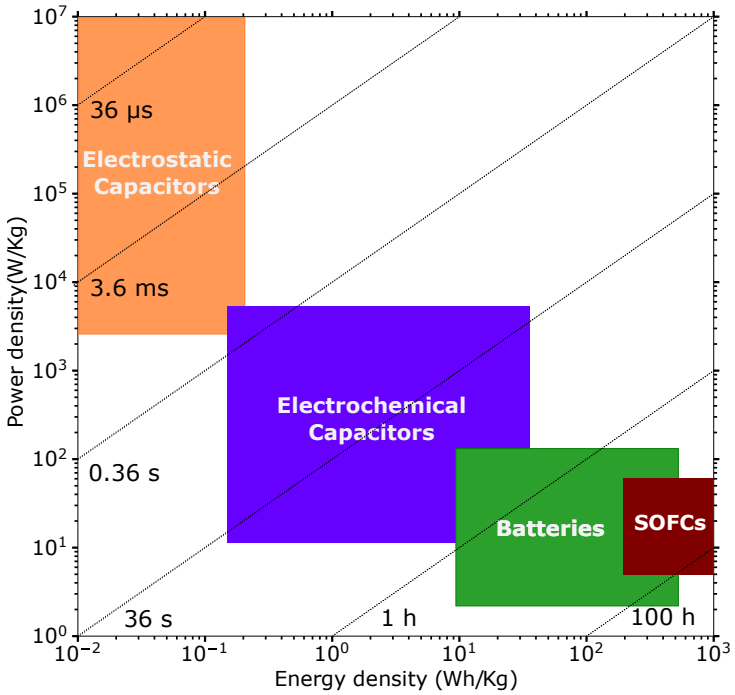

Figure 1.1: Ragone plot of different energy storage devices. The straight dash lines and the associated times correspond to the characteristic times. Adapted from Reference 1.

and power densities. Nevertheless, their total energy storage density is typically relatively lower than that achieved in batteries. For many practical applications, for example hybrid electrical vehicles, microwave communications, renewable energy storage, distributed power systems, high-power applications, etc. (Figure 1.2), not only relatively high energy storage densities but also high electrical power output is essential. The overall energy storage capabilities and electrical power output properties of special types of dielectric capacitors make them unique and potentially promising for use in the above-mentioned and other industrial areas. Currently, commercially available solid-state capacitors for high-power applications are dominated by polymer and dielectric ceramics, but they usually possess limited energy density of less than 2 J/cm^3. The challenge is therefore to design capacitors being able to reach higher energy densities. In fact, high energy density dielectrics would significantly reduce the device volume (increase the volumetric efficiency), thus benefiting many applications where miniaturization, light weight, low cost, and easy integration are desirable, e.g.

Figure 1.2: Application field of capacitors. Reprinted from Reference 1.

consumer electronics, pulsed power applications, and commercial defibrillators, to name a few.[3]

1.2 Recoverable Energy in Different Types of Dielectrics

In order to define quantities like the energy density and energy efficiency, we need to look at how a material responds to an external electric field. When an external electric field is applied, a polarization (P) can be induced. Among the several mechanisms that can cause polarization are the displacement of

the electron cloud with respect to the nucleus, the displacement of ions in the lattice, the displacement of electrons along chemical bonds, the reorientation of molecules, and the transport of mobile charges.[4] In linear dielectrics, the relationship between polarization P and applied field E is linear:

$$P = \chi_e \varepsilon_0 E, \tag{1.1}$$

where χ_e and ε_0 are the (dimensionless) electric susceptibility of the material and the dielectric permittivity of vacuum, respectively. The electric susceptibility and the relative permittivity,

$$\varepsilon_r = 1 + \chi_e, \tag{1.2}$$

are measures for both the level of polarization that the material experiences and the amount of energy it can store when used as a capacitor. There are also cases where the behavior differs from that of a linear dielectric, for example when the material already possesses permanent electric dipoles before it is subjected to an electric field. This is the case of Ferroelectric (FE) and Antiferroelectric (AFE) materials. Figure 1.3 shows the polarization-electric field (P-E) curves for linear dielectric, ferroelectrics and antiferroelectrics. The stored energy density and recoverable energy density can be calculated by the integration of electric field by polarization as follows,[2]

$$W_{st} = \int_0^{P_{max}} E dP, \tag{1.3}$$

$$W_{rec} = -\int_{P_{max}}^{P_r} E dP, \tag{1.4}$$

where, E is the external applied electric field, P_r and P_{max} represent the remanent polarization and maximum polarization, respectively. The ratio of the recoverable energy density to the stored energy density is defined as the energy efficiency (η)

$$\eta = \frac{W_{rec}}{W_{st}}, \tag{1.5}$$

while the energy loss is

$$W_{lost} = W_{st} - W_{rec}. \tag{1.6}$$

Since linear dielectrics show no hysteresis (Figure 1.3a), they are able to recover practically all the stored energy ($\eta \simeq 1$). Because of their relatively low dielectric constant and low polarization, however, the energy density of linear dielectrics

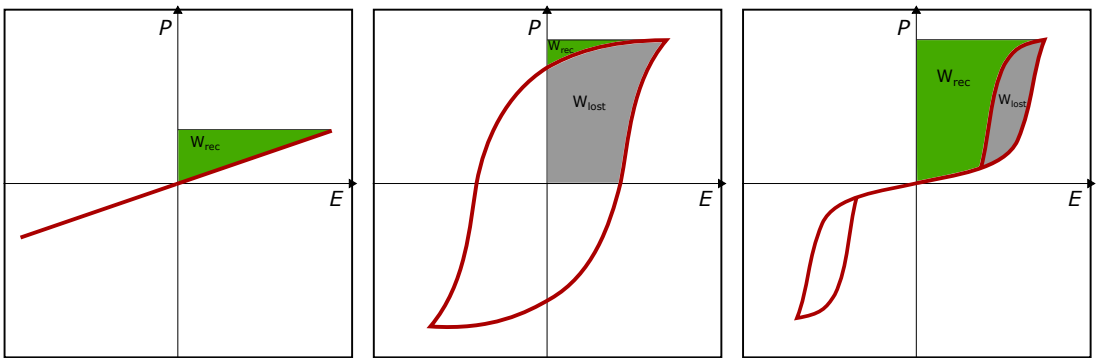

(a) (b) (c)

Figure 1.3: Characteristic P-E behaviour of linear dielectrics (**a**), ferroelectrics (**b**) and antiferroelectrics (**c**). The gray and green areas represent the energy loss (W_{lost}) and recoverable energy (W_{rec}), respectively.

is usually lower than 1 J/cm^3.[2] Ferroelectrics (Figure 1.3b), on the other hand, exhibit spontaneous electric polarization, whose direction can be switched by applying an external electric field. Therefore, they usually possess high dielectric constants, which means they are able to reach higher values of stored energy density (W_{st}). Nevertheless, they show high values of remanent polarization, which heavily limits the amount of energy that can be recovered (green area in Figure 1.3b) and causes high energy loss (W_{lost}, gray area in Figure 1.3b), due to the additional energy required to orient the spontaneous polarization in the direction of the field. The *P-E* behaviour of antiferroelectrics (Figure 1.3c) lies somewhere in between. In fact, they display the so-called double *P-E* loops, where two distinguished hysterisis are present at higher fields, with a region of linear behaviour in between. These features yield much higher stored energy densities than linear dielectrics, and at the same time limit the energy loss, due to the smaller hysterisis. For these reasons, AFEs display much higher efficiencies (η) than FE materials, which makes them perfect candidates for applications in energy storage. From this point on, we will refer to loops which have the same shape as Figure 1.3c as AFE loops.

So far, we have been treating only the behaviour on a macroscopic scale. In the following section, we present the origin of these particular hysteresis loops, focusing on models which have been developed to define and describe antiferroelectricity on an atomistic level.

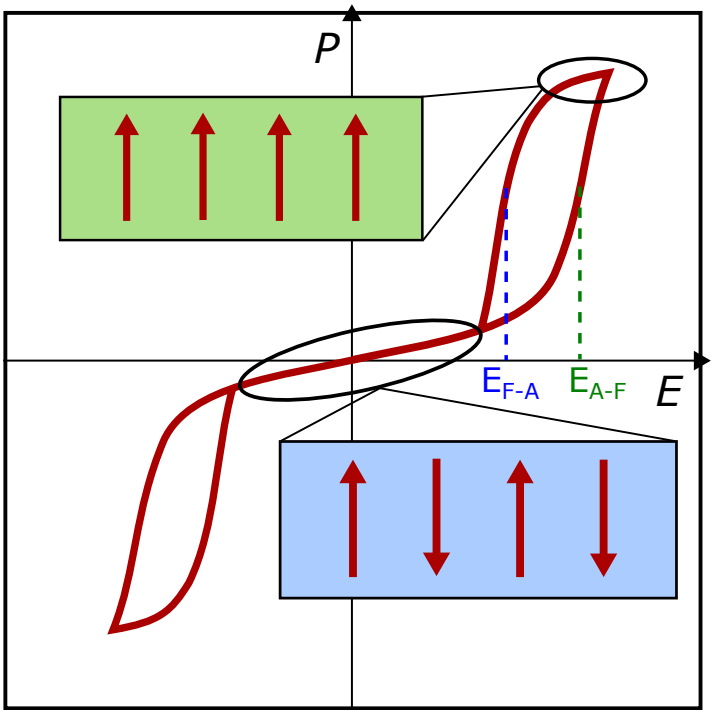

Figure 1.4: Origin of the double *P-E* loops in antiferroelectric (AFE) materials. For low fields the AFE is stable and $P(E)$ is linear. When the field increases up to the critical field E_{A-F}, a phase transition to the ferroelectric (FE) phase occurs, yielding a sudden increase in polarization. When the field is lowered, the reverse phase transition occurs at E_{F-A}, receding to the linear regime and leading to a double hysterisis loop.

1.3 Concept of Antiferroelectricity

The definition of antiferroelectricity has been a subject of some ambiguity, particularly with regards to the distinction between macroscopic and atomistic perspectives. From a macroscopic perspective, antiferroelectricity is defined as the behaviour of the electric polarization which produces double *P-E* loops, as described in the previous section.[2] This definition is based on the observed behavior of the material at the macroscopic scale, and is typically used to describe the electrical properties of materials. From an atomistic perspective, however, the definition of antiferroelectricity is somewhat different.
Before we present the theory of antiferroelectricity, we will introduce briefly the related concept of ferroelectricity. FE materials display parallelly oriented

adjacent electric dipoles within the crystal structure. The dipoles can interact with an external field and can be arranged according to the direction of the field.[5,6] When the field is removed, the minimum energy configuration is still with parallel dipoles, thus resulting in non-zero remnant polarization (P_r). When the direction of the field changes, additional energy is required to flip the orientation of the dipoles to follow the new electric field. These are the reasons behind the shape of the *P-E* loops in FE materials sketched in Figure 1.3b. The situation is different for AFE materials. This type of phenomenon was first predicted in 1951, by C. Kittel.[7] In his definition, the structure of an AFE material can be described by two sublattices. While the arrangement of permanent dipoles generates a net polarization in each sublattice, the polarization directions of the sublattices are antiparallel to each other. If the magnitude of both contributions is equal, they fully compensate each other. Therefore, the net macroscopic spontaneous polarization in the ground state is zero. A schematic representation of the origin of their *P-E* loops is shown in Figure 1.4. For low electric fields, the AFE ground state is stable, and the response is linear. When the field strength reaches a critical value (E_{A-F}), a structural phase transition from an antiferroelectric to a ferroelectric state occurs. The field-induced phase transition between the AFE and the FE state is typically characterized by ionic displacements, a change of the crystal symmetry, and an increase in the lattice volume.[8] After the phase transition, the FE state leads to a sudden increase in polarization. When the field is removed, the reverse transition from the unstable FE phase to the stable AFE phase can occur at field E_{F-A} (with $E_{F-A} < E_{A-F}$). These reversible phase transitions are responsible for the double *P-E* loops in Figure 1.4.

While the model proposed by Kittel provides a relatively simple qualitative explanation of the double P-E loops, it failes to describe the structure-property relations of most materials. In fact, no AFE structure is known that can actually be described as consisting of two sublattices of equal, but antiparallel polarization.[9] The first expansion to the Kittel model was made by G. Shirane when he introduced an energy criterion.[9,10] In his definition, the free energy difference between the AFE phase and the field-induced FE phase must be small. At room temperature, the AFE phase should therefore only be slightly more stable than the related FE phase, allowing the latter to be induced by an electric field. A more complete definition of AFE materials also takes symmetry arguments into account. The AFE and FE phases must be symmetry-related in order to allow for a rearrangement of the local dipoles when the electric field is applied. K. Rabe proposed the following definition:[9]

- The ground state of the material is a non-polar phase
- A close-in-energy polar phase exists
- The same high-symmetry structure is a parent of both phases
- A transition from the non-polar phase to the polar phase can be induced by the application of an electric field, which leads to the observation of double *P-E* loops

It should be noted that the presence of double *P-E* loops is not a sufficient condition for antiferroelectricity. For example, double *P-E* loops can be observed as a result of defects.[11,12] Coincidentally, the absence of double *P-E* loops does not always exclude antiferroelectricity. In fact, some materials can experience dielectric breakdown before the forward switching field is reached, making it impossible to measure double P-E loops, even if a related polar structure exists.[2] In other cases, the FE state is metastable, resulting in an irreversible phase transition. Once the electric field is applied and the transition has taken place, these materials will then exhibit FE-typical single P-E loops.[13] Therefore, the relative stabilities of the AFE and related FE phases determine whether a reversible phase transition can be induced by application of an electric field, and thus whether the favorable energy-storage properties of antiferroelectrics can be exploited.
In the next section, we will discuss which antiferroelectric materials are the most promising candidates in the context of energy storage properties, with particular focus on the two objects of this work: $NaNbO_3$ and $AgNbO_3$.

1.4 Lead-free Antiferroelectrics

Many materials which display antiferroelectric properties are based on the perovskite structure. The ABO_3 perovskite structure has a B-cation site that is octahedrally coordinated and an A-site cation site that is 12-fold coordinated. An example of the prototype cubic perovskite structure is shown in Figure 1.5a. Various cooperative displacements of cations and tilting of the O-octahedra develop through the phase transitions and can lead to lower symmetry phases: polar or non-polar. Ever since the 1960s, the main focus for devices based on antiferroelectric material has been on lead-based compounds. More specifically, the most performant devices are based on the solid solution $PbZrO_3$ - $PbTiO_3$ (lead zirconate titanate, or PZT). The capabilities can be further improved by doping with La on the A-site (PLZT) and/or Sn on the B-site (PLZST).[2] TDK Corporation

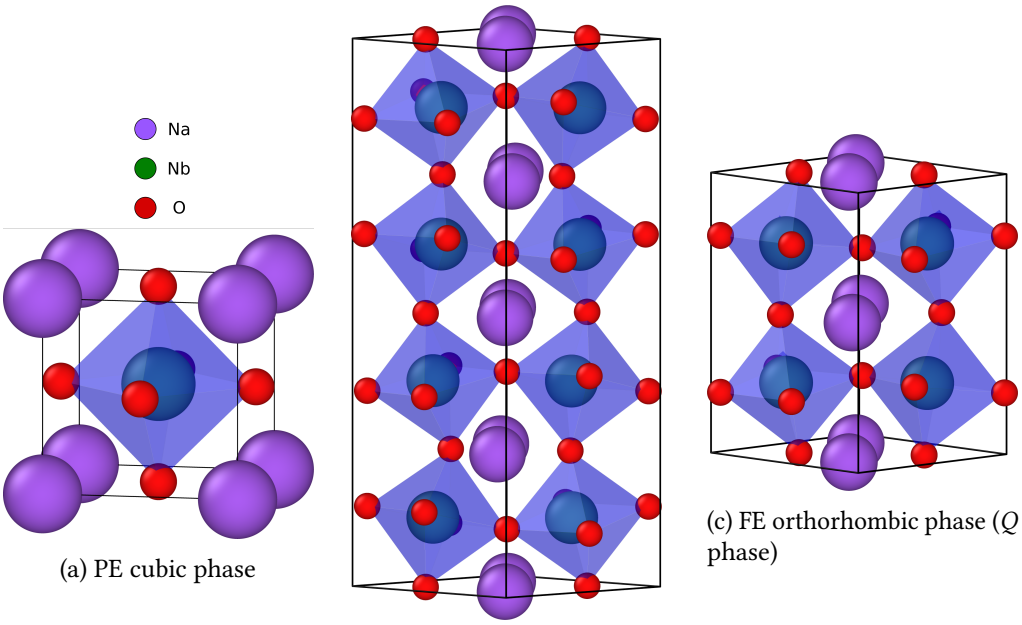

(a) PE cubic phase

(b) AFE orthorhombic phase (*P* phase)

(c) FE orthorhombic phase (*Q* phase)

Figure 1.5: Structures of the high temperature cubic phase and room temperature orthorhombic polymorphs of $NaNbO_3$.

has introduced a high-performance multi-layer ceramic capacitor made of AFE PLZT with copper electrodes called Ceralink™ that operates between -55 °C and 150 °C, at high voltages ~500 to 1000 volts, and ~10 µF, with high reliability.[14] The use of lead-containing compounds in various products has come under scrutiny in recent years due to concerns about lead poisoning and environmental pollution. According to the World Health Organization (WHO),[15] lead is a toxic substance that can cause serious health problems, especially in children, and it can persist in the environment for a long time. As a result, there has been a growing effort to find alternatives to lead-containing compounds and to phase out their use where possible. Lead-free systems have become increasingly necessary for environmental and health reasons. Lead-free solders, for example, are now widely used in electronics manufacturing to avoid the risk of lead contamination. In the plumbing industry, lead-free pipes and fittings have replaced traditional lead pipes to reduce the risk of lead contamination in drinking water. Lead-free paint and gasoline have also been introduced to reduce lead emissions into the environment. The transition to lead-free systems can be challenging, as lead-containing

compounds have been widely used for many years and have well-established applications. However, with continued research and development, alternatives to lead-containing compounds are becoming increasingly available, and their use is necessary to protect human health and the environment.
Two of the most promising lead-free AFE materials for energy storage applications are $NaNbO_3$ and $AgNbO_3$. Both are pervoskites with a cubic high temperature phase and an orthorhombic room temperature (RT) phase. In the following, we provide an overview of the structure and properties of these two materials.

$NaNbO_3$

Due to the volatilization of sodium oxide at high temperatures, synthesizing high-quality single-phase $NaNbO_3$ ceramics has been a long-standing problem.[16] Sodium niobate experiences a complex sequence of phase transitions as a function of temperature. The list of phase transitions with respective nomenclature is reported in Table 1.1.[16–20] The room-temperature orthorhombic *P* phase, with eight formula units per unit cell, features antiparallel displacements of both the sodium and niobium cations and is additionally characterized by octahedral tilting.[19,21] In both cases, the antiparallel cation displacements give rise to an antiparallel ordering of permanent dipoles that effectively compensate each other on a unit cell basis. At room temperature, the AFE *P* phase might coexist with a FE polymorph named *Q* phase (space group $Pmc2_1$). These two polymorphs are relatively close in energy and the phase transition from the *P* to the *Q* phase occurs by applying a sufficiently strong external field. Figure 1.5 shows the cubic parent structure, the AFE *P* phase, and the FE *Q* phase.
In $NaNbO_3$, the double *P-E* hysteresis loops are rarely observed, since the field-induced FE *Q* phase remains in a metastable state after the field is removed. As a consequence, the system preserves a spontaneous polarization even without applied field.[22] However, as mentioned in the previous section, materials displaying a narrow double *P-E* loop are of interest for energy storage applications. In order to reach this condition, the AFE phase needs to be stabilized over the FE phase, so that the AFE−FE phase transition is reversible, and the system does not show spontaneous polarization.[23] One way to achieve this, like for lead-bases systems, is chemical modification, which will be treated in Section 1.5.
In this work, the phases of interest are the trigonal *N* phase, the orthorhombic *P* phase, and the cubic *C* phase. Because the nomenclature used for sodium niobate can be confusing and is not always consistently used in literature, in this work we refer to the three phases by relying on their crystal system, naming therefore the

This work	Lit.	Crystal system	Space group	Temperature (K)	Behaviour
R	*N*	Trigonal	R3c	up to 173	FE
O	*P*	Orthorhombic	Pbcm	173 - 633	AFE
	R	Orthorhombic	Pmnm	633 - 753	AFE
	S	Orthorhombic	Pnmm	753 - 793	PE
	T_1	Orthorhombic	Cmcm	793 - 848	PE
	T_2	Tetragonal	P4/mbm	848 - 913	PE
C	*C*	Cubic	$Pm\bar{3}m$	from 913	PE

Table 1.1: List of phase transitions and respective nomenclature in this work and in the literature for $NaNbO_3$. The last column on the right indicates if the phase exhibits Ferroelectric (FE), Antiferroelectric (AFE) or Paraelectric (PE) behaviour.

This work	Lit.	Crystal system	Space group	Temperature (K)	Behaviour
O	M_1	Orthorhombic	Pbcm	up to 340	AFE
	M_2	Orthorhombic	Pbcm	340 - 540	AFE
	M_3	Orthorhombic	Cmcm	540 - 626	AFE
	O_1	Orthorhombic	Pmnm	626 - 634	PE
	O_2	Orthorhombic	Cmcm	634 - 660	PE
	T	Tetragonal	P4/mbm	660 - 852	PE
C	*C*	Cubic	$Pm\bar{3}m$	from 852	PE

Table 1.2: List of phase transitions and respective nomenclature in this work and in the literature for $AgNbO_3$. The last column indicates if the phase exhibits Ferroelectric (FE), Antiferroelectric (AFE) or Paraelectric (PE) behaviour.

low temperature trigonal phase as R phase, the room temperature orthorhombic as O phase, and the high temperature cubic as C phase.

$AgNbO_3$

The precursors for the synthesis of AN are Ag_2O and Nb_2O_5.[24] However, in the later stages of the reaction, the actual precursors are metallic Ag and Nb_2O_5. In fact, Ag_2O decomposes into metallic Ag (at circa 200 °C), but the kinetics of the reaction is accelerated by using Ag_2O in the initial stage. Most commonly, the synthesis has been carried out in oxygen atmosphere. In recent years, however, it has been shown that it is possible to synthesize AN in air atmosphere, while the reaction does not occur in O-poor atmosphere.[25] In general, it has been reported that kinetics plays a central role in this reaction, which increases the complexity of the studies on $AgNbO_3$, due to the difficulty in obtaining samples of consistent quality. Moreover, it intensifies the challenge also from a computational perspective, as we will address in Section 4.1. Last but not least, it has been discovered that, after the synthesis process, the resulting material has a propensity to exhibit non-stoichiometric behavior, which can be attributed to Ag deficiency.[26]
In spite of the numerous efforts dedicated to the structural investigation of $AgNbO_3$, there is still an ongoing debate on the structural details of AN. Sciau *et al*[27] have concluded that the average structure of the room temperature phase can be described by the *Pbcm* space group, attributing the origin of the weak antiferroelectric behaviour of room temperature phase to local structural changes. Based on the dielectric measurements and structural characterization, Kania *et al* summarized the phase transition sequence of $AgNbO_3$ as a function of increasing temperature, which is reported in Table 1.2. Also, Levin *et al*[28] have proposed the $Pmc2_1$ space group for the ferroelectric phase of AN, suggesting that weak ferroelectricity is due to local cation displacement disordering. The parent cubic, AFE and FE structures are therefore identical to the ones shown in Figure 1.5. Investigations by Niranjan and Asthana[29] using density functional theory have reported that the *Pbcm* and $Pmc2_1$ phases are very close in energy (difference of only 0.1 meV/f.u.), suggesting that the coexistence of the two phases would explain the experimental *P-E* loop, which exhibits antiferroelectric-like behavior with a small remnant polarization at zero field. Contrary to the case of $NaNbO_3$, the phase transition is reversible. Similarly to $NaNbO_3$, narrower *P-E* loops can be achived through chemical modification. The most common doping strategies and their role in the AFE properties are discussed in the next section.

1.5 Defects and Doping Strategies in Lead-free Antiferroelectrics

In order to expand the use of antiferroelectric (AFE) materials for energy storage, certain issues must be resolved. High energy density and efficiency are both necessary for practical applications. AFE materials with a high energy density require a large AFE-FE phase transition electric field and a substantial difference between remnant polarization and maximum polarization, as shown in Figure 1.4. To ensure high energy efficiency, these materials must also have a narrow hysteresis loop. Although AFE materials have significantly improved in energy density in recent years, their energy efficiency, typically less than 85 %, is still inferior to that of linear dielectric materials.[2] This not only results in energy loss, but may also generate heat during discharge and degrade the properties of the ceramics. The behavior of AFE materials during phase transition, including the critical electric transition field from AFE to FE, its reversibility and polarization values, depends heavily on the material's composition. Therefore, modifying the composition and doping the material have been identified as the most effective ways to tailor AFE materials and improve their energy storage properties. These techniques have been widely reported in the literature.[2]

One critical aspect of chemical modification that is too often overlooked is the conceptual difference between doping and substitution. Doping and substitution are two distinct processes in materials science that involve introducing impurities or foreign atoms into a host material. Doping is a process where, after introducing a substitutional defect, the charge state of the system is modified. In other words, the valences of the substituted and substituting atoms are different. Because this process introduces a charge that needs to be compensated, the Fermi level of the system is modified (more detailed thermodynamics will be discussed in Section 2.4). These defects can affect the material's electrical and optical properties, such as its conductivity and luminescence. On the other hand, substitution is a process where the introduction of the substitutional defect does not introduce any additional charge, thus not affecting the Fermi level of the material. In this situation, the valences of the substituted and substituting atoms are identical.

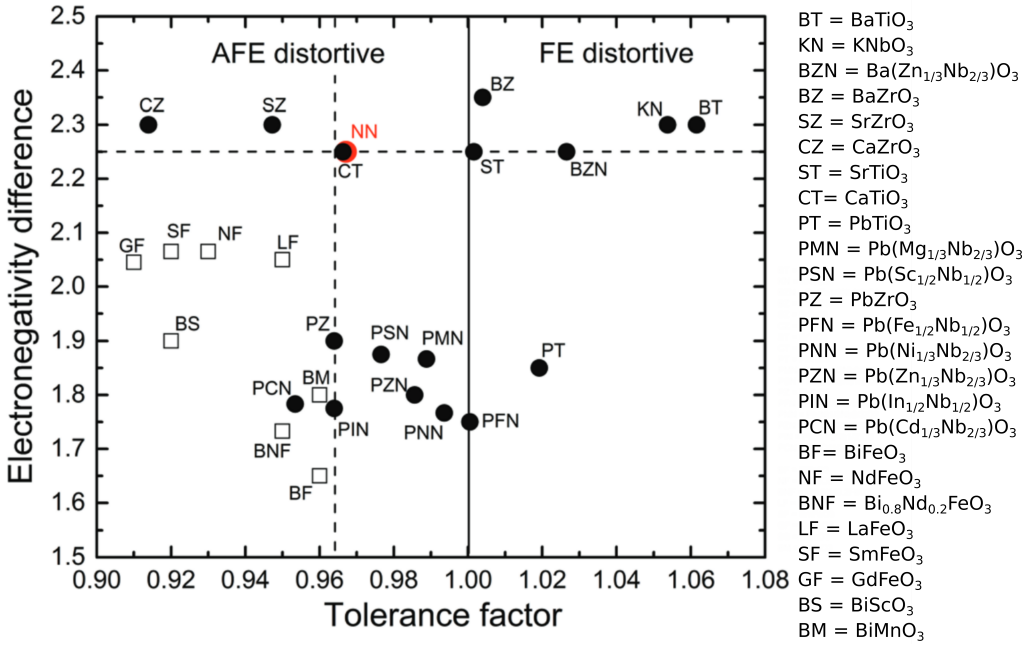

Figure 1.6: Tolerance factor versus averaged electronegativity difference for various perovskites, reproduced from Reference 30.

1.6 Tolerance Factor

A common guideline that is typically followed to adjust the composition and modify the energy storage properties of AFE materialsis is based on the Goldschmidt tolerance factor, t. The tolerance factor allows for a surprisingly accurate prediction about the preference for ideal cubic arrangements in perovskites and is given by[2,31]

$$t = \frac{r_A + r_O}{\sqrt{2}(r_B + r_O)}, \tag{1.7}$$

where, r_A, r_B, and r_O represent the radius of A-site, B-site, and oxygen ions. If the tolerance factor is approximately one, the ideal perovskite structure is often favored. This is reached for large A-site cations and B-O π bonding, stabilizing the cubic symmetry.[32] On the other hand, if t is not one, either the B ($t > 1$) or the A ($t < 1$) cation is too small.[33] Therefore, these cations will displace from their regular position to optimize their local bonding environment (increased overlap with the surrounding oxygen $2p$ orbitals). As a result, when the tolerance factor is greater than 1 (t > 1), the ferroelectric (FE) phase will be more stable, whereas

when the tolerance factor is less than 1 ($t < 1$), the antiferroelectric (AFE) phase will be more stable. As a consequence, the antiferroelectricity can be improved by substituting smaller ions in the A-site or larger ions in the B-site of the perovskite materials.
Moreover, Halliyal and Shrout[34] found that plotting the tolerance factor t versus the average electronegativity provides information on the stability of the perovskite family of compounds across different substitutions and solid solutions. The average electronegativity is expressed by

$$X = \frac{X_{AO} + X_{BO}}{2}, \tag{1.8}$$

where X_{BO} is the electronegativity difference between the B cation and the oxygen anion, while X_{AO} is the electronegativity difference between the A cation and the oxygen anion. Both these quantities give an indication of the ionicity of the $A - O$ and $B - O$ bonds. Figure 1.6 shows the relationship between t and X for various perovskite compounds, including a wide range of both simple and complex perovskites. Lead perovskite compounds that are characterized by low values of both t and X are known to have a tendency to form pyrochlore phases. However, the perovskite phase can be stabilized by creating solid solutions where either t or X is increased.

1.7 Fermi Level Engineering

While these two criteria can be surprisingly succesfull in predicting the behaviour of perovskite structures, they can be classified as a "rule of thumb", since they neglect many aspects of the physics involved. In fact, by considering only the radius of the ions, the effects of the chemical modification on the Fermi level are completely neglected. Moreover, while the electronegativy difference can be a good initial descriptor for the nature of the chemical bonding, it both fails to describe what is the connection between the band structure and the structural distortions, and to provide information on the oxidation states of the substituting elements.
In order to bridge this gap, much more in-depth studies need to be conducted. Firstly, the nature of the defects and the relative oxidation states of the elements need to be clarified (doping *vs* substitution) by evaluating the stability of all the possible defect charge states. Secondly, the equilibrium between all the charges (ionic and electronic) needs to be studied, in order to evaluate the impact of doping

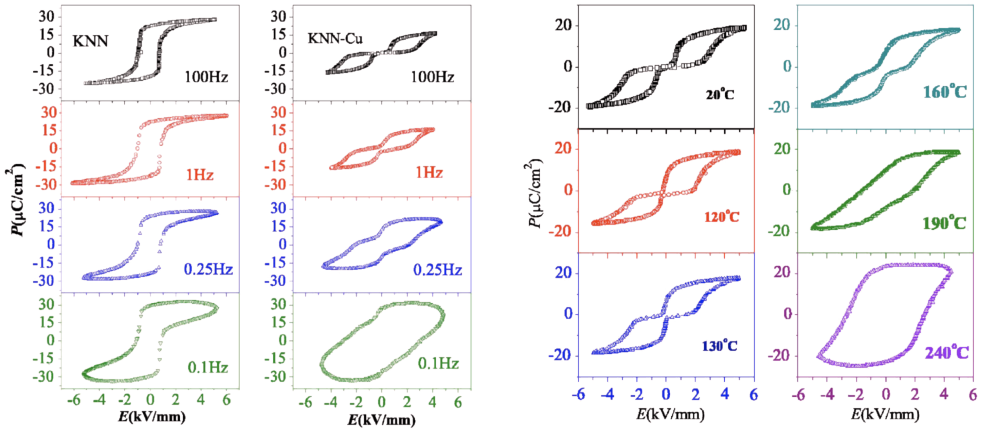

Figure 1.7: a) *P-E* loops of the KNN and KNN-Cu ceramics measured at different frequencies. b) P-E loops for the KNN-Cu ceramic measured at 100 Hz and different temperatures. Reprinted from Reference 36.

on the Fermi level. Understanding the Fermi level in these materials is crucial to understand the role of chemical modification in the AFE properties. Changes in the Fermi level affect other formation mechanisms and concentrations of defects. Depending on the compensation mechanisms, different defect species are involved in the reaction of the material on the insertion of a charged defect. The concept of Fermi level engineering utilizes the relation between defect concentrations and the Fermi level to select the desired compensation mechanism and to eventually control material properties. For example, controlled doping of semiconductors, which is the basis of semiconductor technology, can be considered as Fermi level engineering in order to realize a wide range of applications such as (light emitting) diodes, transistors, solar cells, sensors, varactors, microwave generators, and more.[35] In Chapter 2 we will show how to understand and predict, with computational methods, the effect of defects and synthesis conditions on the Fermi level.

1.7.1 Defect Dipoles

In addition to modifying the Fermi level and defect concentrations, doping can also impact other observables in the system, like the interacion with an external electric field. So far we have only been treating the impact of single defects on

the material properties. When defects are charged, however, they can associate and form a defect complex, if the new configuration is energetically favorable.[37] Since we have an association of charged defects, an electric dipole is formed. Defect dipoles can have a significant impact on the properties of ferroelectric and antiferroelectric materials. In ferroelectrics, defect dipoles can affect the orientation and stability of ferroelectric domains, as well as the overall ferroelectric polarization. For example, it has been shown that defect dipoles can affect the *P-E* hysterisis in $BaTiO_3$[38] and $BiFeO_3$.[12] Moreover, it has been reported that defect dipoles influence the switching mechanisms in $(K_{0.5}Na_{0.5})NbO_3 - Cu$ ceramics. Hysterisis loops of undoped and Cu-doped KNN, measured by Lin *et al*,[36] are reported in Figure 1.7. Because of the symmetry-conforming property, the acceptor dopant ions Cu^{2+} and O^{2-} vacancies form defect dipoles along the polarization direction, after the tetragonal-orthorhombic phase transition of the ceramic. As a result of the low defect migration rates, the defect dipoles remain in the original orientation and provide restoring forces to reverse the switched polarization, which results in the double *P-E* loop observed in the KNN-Cu ceramic. The same restoring force introduced by defect dipoles has been proposed by Hao *et al*[11] in aged KNN-Cu samples.
In light of these observations, it is clear that not only single defects but also defect dipoles need to be investigated, in order to have a complete picture of the connection between defects and antiferroelectric properties.

1.8 Chemical Modification in $NaNbO_3$ and $AgNbO_3$

In recent years, chemical modification has been heavily employed to modify the AFE properties of both $NaNbO_3$ (NN) and $AgNbO_3$ (AN). For NN, different approaches have been investigated.[40] Gao *et al* reported double *P-E* loops in the $(BiScO_3)_x - (NaNbO_3)_{1-x}$ solid solutions.[41] More specifically, they showed that doping $NaNbO_3$ with Bi and Sc stabilizes the antiferroelectric (AFE) phase without changing the crystal symmetry of $NaNbO_3$. Other works proposed various co-doping approaches, such as (Sr, Zr),[42] (Ca, Hf),[43] (Sr, Hf),[30] and (Ca, Sr).[44] The work which has inspired our studies has been conducted by Zhang *et al*,[23] who have found that the energy efficiency of $NaNbO_3$ can be significantly improved upon the addition of $SrSnO_3$. Figure 1.8a shows the *P-E* loops with different $SrSnO_3$ compositions. The optimal composition is found to be 5 wt%, as for larger concentrations phase segragation occurs. The plot reveals that the remnant

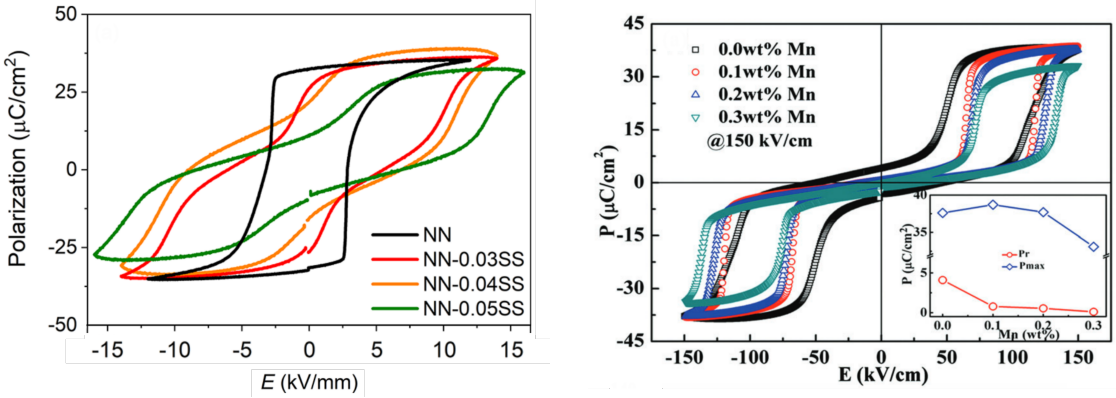

(a) (b)

Figure 1.8: Improved *P-E* loops upon chemical modification of $NaNbO_3$ (a) with $SrSnO_3$ (from Reference 23) and $AgNbO_3$ (b) with MnO_2 (from Reference 39).

polarization (P_r) is consistently lowered with increasing dopand concentration. The value of P_r is, however, still larger than zero, deviating from the ideal double *P-E* loop, like the one shown in Figure 1.4. This might indicate that, while chemical modification augments the reversibility of the AFE-FE phase transition, the complete reversibility in $NaNbO_3$ is not yet achieved.

The same approach has been employed for $AgNbO_3$. For example, it has been reported that doping with Bi (A-site) and W (B-site) has shown an improvement on the AFE properties.[45,46] The starting point of our work, however, is the research conducted by Zhao *et al*,[39] who have obtained considerably improved P-E loops by adding Mn into the system, as shown in Figure 1.8b. They have found the optimal concentration of Mn to be 0.3 wt%.

While these prove to be important achievements in the field of AFE materials, which have lead to a considerable improvement of the AFE properties of NN and AN, the physics behind these results is still unclear. Because these works have been guided by empirical guidelines, like the tolerance factor described in Section 1.6, the role that chemical modification has on the properties of NN and AN is still unraveled. In this context, the first problem to tackle is the impact of defects both from a thermodynamical and kinetical point of view. These observations raise a number of scientific questions, reported in the next section, which have motivated the work in this thesis.

1.9 Research Questions

In this section, we will summarize the questions that were raised in this chapter. The goal is to provide an outline of the open scientific problems, and to highlight the objectives of this doctoral thesis.

Which defects are forming in these materials?

If dopands are introduced into a system, they will interact with the present intrisic defects. Therefore, the first step of our study is to identify which intrinsic defects are forming in the material and in which concentrations. Additionally, since the behaviour of the extrinsic defects is unknown, it cannot be modelled *a priori*, rather it needs to be studied with the same approach as the intrinsic defects. In fact, the stable charge states of these defects needs to be determined, in an effort to understand their influence on defect equilibrium. In order to achieve this, the formation energies in all possible charge states need to be computed, which will give information on the defect concentrations and their charge transition levels.

Where is the Fermi level and what is the influence of doping conditions?

The determination of the Fermi level is the key step to know the concentrations of defects and charge carriers. In fact, the Fermi level controls the behaviour of the semiconductor (n-type or p-type) and influences the dopability limits of the system. Moreover, it is important to investigate the impact of doping on the Fermi level, which reveals what charges are introduced in the system, and how defects can modify the antiferroelectric properties. Another crucial problem is the influence of the synthesis conditions on the Fermi level. In fact, when diffusion of defects is particularly slow, it is possible that concentrations do not reach thermodynamic equilibrium after synthesis. Therefore, our interest is to understand how defect quenching affects the Fermi level, especially when combined with doping.

What role do defect associates play in the AFE properties?

Not only single defects, but also defect complexes have an impact on the antiferroelectric properties of the materials. When charged defects interact with each other and form associates, they form defect dipoles. These dipoles interact with the local spontaneous polarization and with an external electric field,

thus influencing the AFE-FE phase transitions and the *P-E* loops. Therefore, it is key to investigate whether doping introduces defect complexes, and in what concentrations, in order to assess if they consitute a factor which modifies the antiferroelectric behaviour of the materials of interest.

2 Methodology

In the following chapter, we present a brief overwiew of the fundamental theory and methodology which has been used in this work. In the first part, we review the basics of density functional theory, including the most important concepts such as exchange-correlation functionals, basis-sets and pseudo-potentials. In the second part, we present the formalism, procedure and challenges of thermodynamic calculations on point defects, highlighting how we have approached the currently established theory to account for the presence of dopants and quenched defects (Section 2.4.8). Finally, in the last part, we give a short overview of the workflow and tools we have developed to create and analyse the databases, with the aim to provide a framework to speed up the analysis of defect calculations.

2.1 Born-Oppenheimer Approximation

A quantum mechanical description (also known as first-principles or *ab initio*) of a system and of its properties requires the full account of the elementary constituents of matter, atomic nuclei and electrons, and of all the electromagnetic interactions they mutually exchange. According to the rules of quantum mechanics, the state of a system is then described by a single wavefunction which includes both the nuclear and electronic degrees of freedom. If we knew the form of this wavefunction, we could in principle solve the associated Schrödinger equation and calculate many equilibrium properties of materials. Unfortunately, the solution is very challenging, and in most cases still practically impossible even with the most powerful computers at hand. In the realm of solid state physics, an approximation is generally introduced to tackle the coupled nuclear-electronic problem, known as adiabatic Born-Oppenheimer (BO) approximation. The basic idea is that, since electrons are much lighter than ions, the electronic configuration instantaneously relaxes to its ground state for each position the ions assume during their motion. In this "decoupled" approach, the ground state en-

ergy of the electrons can then be calculated fully quantum mechanically, and the dynamical evolution of the nuclei takes place on the energy landscape (the BO potential energy surface, PES) that is determined by the electronic ground state at each atomic configuration. In mathematical language, the BO approximation relies on the factorization of the global nuclear-electronic wavefunction into a wavefunction for the nuclei only and a wavefunction for the electrons depending parametrically upon the ionic positions as

$$\Psi(\mathbf{R}, \mathbf{r}) = \Phi(\mathbf{R})\psi_{\mathbf{R}}(\mathbf{r}), \tag{2.1}$$

where $\mathbf{R} = \{\mathbf{R_I}\}$ is the set of all nuclear coordinates of the system, and $\mathbf{r} = \{\mathbf{r_i}\}$ is its electronic counterpart (the spin degrees of freedom are not explicitly indicated). Assuming this factorization in the general Schrödinger equation of the coupled system and neglecting the non-adiabatic terms coming from the kinetic operator for the nuclei acting on the electronic wavefunction $\psi_{\mathbf{R}}(\mathbf{r})$ (which depends parametrically on the nuclei coordinates), it is possible to split the initial complicated problem into two subproblems for the two degrees of freedom. This approach is usually a good approximation, since the mass of the nuclei is much larger than the ones of the electrons, but is known to perform poorly in those cases where non-adiabatic electron-vibron/phonon coupling becomes important. The nuclear problem can thus be written as

$$\left(-\sum_I \frac{\hbar^2}{2M_I}\frac{\partial^2}{\partial \mathbf{R}_I^2} + E(\mathbf{R})\right)\Phi(\mathbf{R}) = \epsilon\Phi(\mathbf{R}), \tag{2.2}$$

where M_I is the mass of the I^th nucleus and $E(\mathbf{R})$ is the Born-Oppenheimer potential energy surface corresponding to the energy of the electronic system with the nuclei clamped at configuration $\mathbf{R}$, obtained by solving a Schrödinger equation for the many-body electronic wavefunction $\psi_{\mathbf{R}}(\mathbf{r})$

$$\begin{aligned} -\frac{\hbar^2}{2m}\sum_i \frac{\partial^2}{\partial \mathbf{r}_i^2}\psi^\alpha_{\mathbf{R}}(\mathbf{r}) + \frac{e^2}{2}\sum_{i\neq j}\frac{1}{|\mathbf{r}_i - \mathbf{r}_j|}\psi^\alpha_{\mathbf{R}}(\mathbf{r}) - \sum_{iI}\frac{Z_I e^2}{|\mathbf{r}_i - \mathbf{R}_I|}\psi^\alpha_{\mathbf{R}}(\mathbf{r}) \\ + \frac{e^2}{2}\sum_{I\neq J}\frac{Z_I Z_J}{|\mathbf{R}_I - \mathbf{R}_J|}\psi^\alpha_{\mathbf{R}}(\mathbf{r}) = E_\alpha(\mathbf{R})\psi^\alpha_{\mathbf{R}}(\mathbf{r}), \end{aligned} \tag{2.3}$$

where eZ_I is the charge of the I^{th} nucleus, e and m are the electronic charge and mass, and α is an index for the electronic state. Eq. 2.3 suggests that the BO PES is not unique. In fact, there is a different PES (and a different nuclear wavefunction)

for each electronic state. In general (and in this work we comply with this point of view) the ground state PES is considered as the reference one. This separation of the electronic and ionic degrees of freedom is also a very useful simplification that allows to perform (classical or quantum-mechanical) molecular dynamics calculations once the reference PES is known. The calculation of the PES however remains a formidably hard task. In fact, the wavefunction of a system of interacting electrons cannot be factorized in single-electron terms and the direct solution of the many-body Schrödinger equation becomes a prohibitive task for almost all the systems. As result, in order to perform electronic structure calculations on materials of realistic complexity, we need an alternative approach based on a more tractable quantity than the many-body wavefunction. The density-functional theory (DFT) proved to be the most successful of such methods.

2.2 Density Functional Theory

2.2.1 Kohn-Sham Equations

The idea behind density functional theory is to reformulate the interacting electronic many-body problem, shifting the attention from the many-body wave function $\Psi(\mathbf{r_1}, \mathbf{r_2}, ..., \mathbf{r_n})$ (depending explicitly on 3N electronic Cartesian coordinates for a system of N electrons) to the electron density $n(\mathbf{r})$, which contains only one set of coordinates. By solving the respective Schrödinger-like equations, where $\widehat{H}$ is replaced by a more simple mean field Hamiltonian, one obtains a series of single particle eigenstates (ϕ_i) and their corresponding eigenenergies (ϵ_i). The foundation for the theory is contained in the original papers of Hohenberg, Kohn and Sham.[47,48] The two theorems state that:

- For any system of interacting electrons in an external potential V_{ext}, the potential is determined uniquely (up to a constant) by the ground-state density.
- A universal functional for the energy in terms of the density can be defined such that the exact ground-state energy is the global minimum of this functional and that the density that minimizes the functional is the ground-state density.

Since the external potential $V_{ext}(\mathbf{r})$ also determines the wave function, the wave function itself is implicitly but uniquely defined by the ground state electron

density. Therefore, a universal energy functional ($F[n(\mathbf{r})]$) exists which depends on the electron density and which, together with the system dependent energy contribution due to the external potential $\int V_{ext}(\mathbf{r})n(\mathbf{r})d\mathbf{r}$, minimizes the total energy $E[n(\mathbf{r})]$ when the ground state electron density $n_0(\mathbf{r})$ is given as the argument,

$$E_0 = \langle\Psi_0|\widehat{H}|\Psi_0\rangle = F[n_0(\mathbf{r})] + \int V_{ext}(\mathbf{r})n_0(\mathbf{r})d\mathbf{r}. \tag{2.4}$$

There is no unique prescription how the universal functional $F[n(\mathbf{r})]$ is to be constructed. The approach proposed by Kohn-Sham (KS) goes as follows. First, the universal functional is divided into parts which, from a physical viewpoint, are contributions to the total energy

$$F[n(\mathbf{r})] = T_S[n(\mathbf{r})] + \frac{e^2}{2}\int\int \frac{n(\mathbf{r})n(\mathbf{r}')}{|r-r'|}d\mathbf{r}d\mathbf{r}' + E_{XC}[n(\mathbf{r})]. \tag{2.5}$$

The first term represents the kinetic energy, whereas the second term, called the Hartree term, describes the Coulomb potential energy of a classical charge distribution $n(\mathbf{r})$. All remaining many-body contributions to the energy are grouped together in the last term, which is called the exchange correlation (XC) energy functional. Only for the Hartree energy an explicit expression can be given. In order to evaluate the kinetic energy functional in Eq. 2.5, the electron density is expanded in some fictional single particle orbitals ϕ_i,

$$n(\mathbf{r}) = \sum_i f_i|\phi_i(\mathbf{r})|^2, \tag{2.6}$$

with occupation numbers f_i. In this way the kinetic energy can be expressed in the usual way

$$T_S[n(\mathbf{r})] = \sum_i f_i\langle\phi_i| - \frac{\hbar^2}{2m_e}\nabla^2_{\mathbf{r}}|\phi_i\rangle. \tag{2.7}$$

Minimizing the KS energy functional with respect to individual orbitals under the constraint of mutual orthonormality of the orbitals results in the KS equations

$$\left[-\frac{\hbar^2}{2m_e}\nabla_{\mathbf{r}^2} + V_{eff}(n(\mathbf{r}))\right]\phi_i(\mathbf{r}) = \epsilon_i\phi_i(\mathbf{r}), \tag{2.8}$$

with

$$V_{eff}(\mathbf{r}, n(\mathbf{r})) = V_{ext}(\mathbf{r}) + e^2\int\frac{n(\mathbf{r}')}{|\mathbf{r}-\mathbf{r}'|}d\mathbf{r}' + \frac{\delta E_{XC}[n(\mathbf{r})]}{\delta n(\mathbf{r})}. \tag{2.9}$$

Due to their non-linearity, these equations have to be solved self-consistently. The external potential of the ion cores is constructed by the superposition of either the Coulomb potentials or the so called pseudo-potentials (PP). An initial charge density or set of KS orbitals is selected. This can either be a completely homogeneous charge density or a different guess based on earlier calculations. For the representation of the orbitals and density, a suitable basis set is selected (see Section 2.2.2). The Hartree and XC-potentials are calculated in order to set up the initial Hamiltonian of the system. The Hamiltonian is applied to the trial KS orbitals. Using an iterative matrix diagonalization procedure, the (at least) N lowest eigenvalues and eigenvectors of the system are determined. The new eigenvectors can be used to calculate a new electron density and construct a new Hamiltonian. This self-consistent cycle is usually terminated when the total energy difference compared to the previous cycle falls below a predefined limit. In any new cycle, the new charge density can be used as input, but is usually mixed with the old one to improve the convergence.

2.2.2 Basis Sets

In *ab initio* calculations the basis set is a choice of convenience, system type, accuracy and speed. A very intuitive expansion for the wave function is given by localized atomic orbitals. The wave functions can be represented by a linear combination of Gaussians (GTO), Slater type (STO) or numerical radial atomic-like orbitals.[49] A more systematic basis set is given either by the real-space basis or the plane wave basis, because they are orthonormal and complete so that any arbitrary function is representable without prior knowledge. Especially for spatially extended wave functions, like in solid crystalline systems, plane waves are a natural choice. Bloch's theorem states that the wave function in a crystal is the product of a periodic function u_n and a phase factor[50]

$$\psi_{n,\mathbf{k}}(\mathbf{r}) = u_{n,\mathbf{k}}(\mathbf{r}) e^{i\mathbf{k}\cdot\mathbf{r}}, \tag{2.10}$$

where $\mathbf{k}$ is a wave vector within the first Brillouin-zone. We expand u_n as a plane wave to obtain a sum over lattice vectors $\mathbf{G}$ for each single particle wave function

$$\psi_{n,\mathbf{k}}(\mathbf{r}) = \sum_{\mathbf{G}} c_{n,\mathbf{k}+\mathbf{G}}\ e^{i(\mathbf{k}+\mathbf{G})\cdot\mathbf{r}}. \tag{2.11}$$

The sum is truncated at a specific $\mathbf{G}$ and usually given in terms of a kinetic energy cutoff

$$E_{cut} = \frac{\hbar^2(\mathbf{k}+\mathbf{G})^2}{2m_e}, \tag{2.12}$$

so that the space resolution of the basis-set is independent of system volume for a given E_{cut}. The major strength of the plane wave basis is the efficient evaluation of the kinetic energy (Eq. 2.12) and the electrostatic energies in Fourier space. The drawback is that the size of the basis increases rapidly with cell volume (even for vacuum). Secondly, the rapidly oscillating wave functions in the core region make a large number of plane waves necessary. In practice this problem is circumvented by using effective core potentials, the so called pseudo-potentials (PP). PPs combine the potential due to the core electrons and the nucleus in an effective potential. This approach is justified, because the localized core electrons do not overlap with nearby atoms and have, therefore, no influence on bonding. The norm-conserving ab initio PP, for example, is constructed in such a way that a pseudo wave function has the same value as the true wave function outside a cut-off radius r_c around the core. A list of additional requirements was given by Hamann, Schlüter and Chiang.[51] The all-electron and pseudo valence eigenvalues should agree for the chosen atomic reference configuration, and the logarithmic derivatives of the all-electron and pseudo-wave functions should match at r_c. In addition, the integrated charge inside r_c for all-electron and pseudo wave functions should be equal (norm-conservation). The goal is to obtain smooth PPs in order to minimize the range of Fourier components needed to describe the valence properties to a given accuracy. By increasing the cut-off radius, for example, a greater part of the strongly oscillating wave function within the core region is avoided, and replaced by a smooth function. If the above mentioned criteria are fulfilled one has some freedom to obtain the smoothest function possible to represent the core region. Most recent approaches drop the requirement for norm conservation in order to retain more smoothness. These so called "ultra-soft" PPs proposed by Vanderbilt[52] keep the accuracy by transforming the problem in terms of a smooth function and an auxiliary function around each ion core that represents the rapidly varying part of the density. A related, but more general method is the projector augmented wave (PAW) method by Blöchl,[53] which also employs localized auxiliary functions. The difference is that all information on the core wave function is retained similar to linear augmented plane wave methods.[54] The PAW method strictly is an all electron approach, where the core part of the wave function is frozen.

2.2.3 Functionals for Exchange and Correlation

Local Approximations

In the local density approximation (LDA), the exchange correlation energy density at each point can taken to be the same as in a homogeneous electron gas with that density,

$$E_{XC}^{LDA}[n] = \int n(\mathbf{r})\epsilon_{hom}^{xc}[n(\mathbf{r})]d\mathbf{r}. \tag{2.13}$$

The correlation energy of the homogeneous electron gas can be obtained by highly accurate Quantum Monte-Carlo simulations,[55] while the exchange energy is known analytically. The LDA is sufficiently accurate for many problems in solid-state physics, especially for describing electrons in simple metals, which behave very much like free electrons. Because of its simplicity and limited computational costs, the LDA is very useful for describing large systems as well as for obtaining approximate energies and wave functions that can then be refined by more sophisticated levels of theory. An improvement of the LDA has been achieved by recognizing that the exchange-correlation energy can be described more accurately by including gradients of the electron density,

$$E_{XC}^{GGA}[n] = \int n(\mathbf{r})\epsilon_{xc}(n, \nabla n)d\mathbf{r} = \int n(\mathbf{r})\epsilon_{x}^{hom}(n)F_{xc}(n, \nabla n)d\mathbf{r}. \tag{2.14}$$

The most widely applied functionals were proposed by Perdew, Wang and Ernzerhof[56](PBE-GGA). Although improving on many calculated material properties in comparison with the local approximation, the GGA still has deficiencies in various aspects. Most importantly, both the LDA and the GGA fail to reasonably describe the fundamental band gap, which is generally underestimated (sometimes by more than 50%) in both approximations. This issue is known as the band-gap problem in DFT. Approaches to improve the exchange-correlation energy by including higher derivatives of the electron density have failed, and it is now generally accepted that improvements require to properly account for non-locality.

Hybrid Functionals

The LDA and the GGA functional underestimate the exchange energy, but properly account for the correlation energy. The Hartree-Fock method by definition properly accounts for the exchange interaction, but in turn can not access the correlation energy. The issue can be reformulated in terms of variation of the

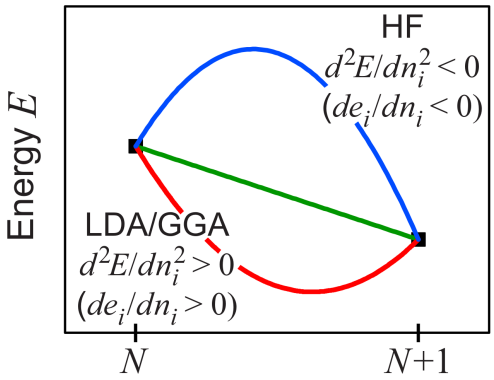

Figure 2.1: Energy *vs* occupation number for different density functional theory (DFT) functionals. In HF theory (blue) the energy is a concave function of the continuous occupation number n_i but a convex one in LDA or GGA (red). The exact functional should be linear with a discontinuous derivative at integer occupations

total energy with respect to fractional changes in the electronic occupations. An exact functional should lead to piecewise linear behavior with discontinuous derivatives at integer occupations.[57,58] DFT calculations based on semilocal XC functionals deviate from this requirement and overbind (concave dependence), whereas HF calculations tend to underbind (convex dependence), as shown in Figure 2.1. These opposite behaviors can be exploited in parametrizations of hybrid functionals that minimize the deviation from piecewise linearity.[59] The idea of hybrid functionals is therefore to mix the exchange-correlation energy of the traditional LDA or GGA functionals with a fraction of exact or Hartree-Fock exchange. In recent years, hybrid functionals have shown a better performance in terms of the description of the exchange and the correlation energy than traditional functionals. Moreover, the band gaps are significantly improved. These functionals, however, are computationally at least two orders of magnitude more expensive than their local or semi-local counterparts. Typical examples of hybrid functionals that have been engineered in such a way are B3LYP,[60] PBE0[61] and HSE06.[62,63]

Hybrid functionals can further be distinguished by whether they use a global approach to mix the exchange correlation energy E_{xc} from a non-local Hartree-fock type exact exchange $E_{\mathrm{x}}^{\mathrm{HF}}$ and a semi-local PBE-GGA contribution $E_{\mathrm{x}}^{\mathrm{GGA}}$, such as

$$E_{\mathrm{xc}}^{\mathrm{hybrid}} = E_{\mathrm{xc}}^{\mathrm{GGA}} + x_{\mathrm{HF}}(E_{\mathrm{x}}^{\mathrm{HF}} - E_{\mathrm{x}}^{\mathrm{GGA}}), \tag{2.15}$$

or whether a range-separated screened hybrid functional such as HSE06 is used.[64] This functional splits the electron-electron interaction into a short-range and a long-range part. For the short range part, 25 % short-range (SR) exact exchange is mixed with 75 % short-range GGA exchange, while the long-range part (LR) is treated purely on the basis of GGA

$$E_{\mathrm{xc}}^{\mathrm{HSE}} = \frac{1}{4} E_{\mathrm{x}}^{\mathrm{HF,SR}}(\omega) + \frac{3}{4} E_{\mathrm{x}}^{\mathrm{GGA,SR}}(\omega) + E_{x}^{\mathrm{GGA,LR}}(\omega) + E_{\mathrm{c}}^{\mathrm{GGA,LR+SR}}. \tag{2.16}$$

The range separaration can be tuned using the exchange screening parameter ω. HSE06 can be considered as a generalized functional in the sense that for $\omega = 0$ we obtain the PBE0 functional, and when ω approaches infinity the short-range non-local exact exchange vanishes and it reduces to standard PBE-GGA. The most notable success of HSE06 is the fact that it is able to give much better band gaps for solids compared to local and semi-local as well as to global hybrid functionals.[65]

2.3 The Nudged Elastic Band Method

In order to obtain the energy barriers for the diffusion of vacancies, the nudged elastic band (NEB) method was employed.[66] The NEB method is a way to obtain the minimum energy path (MEP) between two structures (initial and final structure) that correspond to local minima on the potential energy landscape of the system which are separated by an energy barrier, as shown in Figure 2.2. The energy barrier affects the probability that the system changes from one state to the other. In the NEB method the initial and final structure are interpolated to create a set of intermediate structures, called images. The energy of the images is then minimized, with the constraint that the images may not fall back in the direction of the initial or final structure. This constraint is implemented by subtracting from the forces that act on the particles the force component along the NEB path. In order to keep the images in approximately equal distances from each other, the images are connected by an artificial spring force. At the end of the NEB calculation the images lie along the MEP, and the energy barrier is the energy maximum along the MEP. Within this approach the images close to the saddle point tend to slide to lower energies. This is prevented in the climbing-image nudged elastic band method (CI-NEB).[67] This method converges the highest energy image exactly to the saddle point by zeroing the spring force on this image and including only the inverted parallel component of the true force.

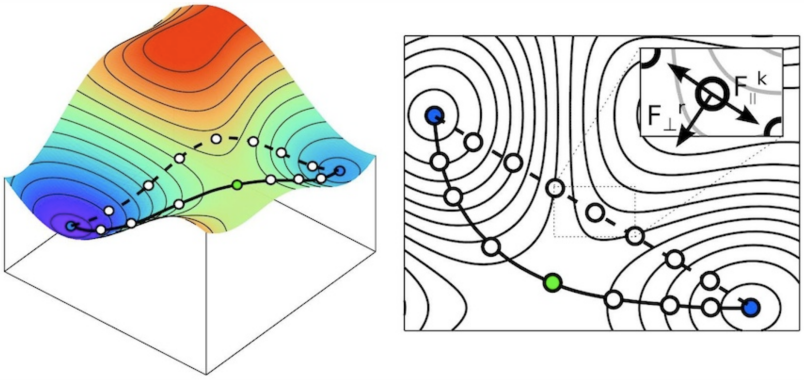

Figure 2.2: In the nudged elastic band (NEB) method, the intermediate configurations in the energy landscape are bonded together with springs, so that they are always constrained to remain between the configurations that precedes and follow them. Of the true force that applies to atoms, only the component normal to the reaction path is used ($F^r_\perp$). Along the reaction path it is the force due to the springs that applies to atoms ($F^k_\parallel$). The NEB calculation stops when the forces are smaller than the convergence criterion. Reprinted from Reference 68.

2.4 Thermodynamics and Kinetics

In the following section we review the current state-of-the-art to characterize defects in the framework of periodic boundary *ab-initio* calculations. In particular, we focus on the thermodynamics of point defects formation and thermodynamic defect equilibrium, with an overview on how to connect it to DFT. A summary of the most important relationships we will discuss in this section is shown in Table 2.1. Moreover, we show how we have extended this methodology to obtain defect concentrations outside thermodynamic equilibrium, *e.g.* when the defects do not thermalize, which requires to include on the role of kinetics in defect computations.

2.4.1 Defect Concentrations and Formation Energy

In order to understand and predict the properties of point defects, it is necessary to relate their concentrations to thermodynamic quantities that can be calculated or measured. Let us consider one defect species. We can write the Gibbs free energy associated with the formation of n defects as[69,70]

$$G = G_{bulk} + n(\Delta H^f - T\Delta S^f_{vib}) - TS^f_{conf}, \tag{2.17}$$

Defect formation energy	$\Delta G^f_{q,D}(P, T, \{\mu_s\}, \mu_e)$
Defect concentration	$[D_q] = gN_{sites} \exp\left(-\beta \Delta G^f_{q,D}\right)$
Electron/hole concentrations	$n = \int D(\epsilon) f(\epsilon) d\epsilon$
Charge neutrality	$\sum_{q,D} q \cdot [D_q] - n_e + n_h = 0$
Self-consistent solution	$\{\Delta G^f_{q,D}(\mu_e)\} \longrightarrow [D_q] \longrightarrow \mu_e$
Oxygen partial pressure	$\mu_O(T, p_{O_2}) = \mu_O(T, p^0) + \frac{1}{2} k_B T \ln\left(\frac{p_{O_2}}{p^0}\right)$

Table 2.1: Overview of the important relationships in point defect thermodynamics discussed in this section. The quantities which depend on the electron chemical potential (μ_e) are shown in red.

where G_{bulk} is the free energy of the system with no defects, ΔH^f is the formation enthalpy of the isolated defect, S^f_{conf} the configurational entropy and ΔS^f_{vib} the entropy change associated with the lattice vibrations. At a given temperature the free energy is at a minimum, which means that the variation of free energy associated with the defect is zero,

$$\frac{\partial G}{\partial n} = \Delta G^f - T \frac{\partial S^f_{conf}}{\partial n} = 0, \tag{2.18}$$

where $(\Delta H^f - T\Delta S^f_{vib})$ has been rewritten as the formation energy ΔG^f. The configurational entropy is given by,[71]

$$S_{conf} = k_B \ln W, \tag{2.19}$$

where W is the number of distinct ways (microstates) to arrange the defects, and for ideal solutions is

$$W = \frac{(gN)!}{n!(gN - n)!}. \tag{2.20}$$

Where N is the number of lattice sites and g is a degeneracy factor accounting for the internal degrees of freedom of the point defect. Using Stirling's approximation

($logx! \simeq xlogx - x$), and assuming that we are in the low concentrations regime ($n << N$), we get

$$\frac{\partial S^f_{conf}}{\partial n} \simeq k_B \ln\left(\frac{n}{gN}\right), \tag{2.21}$$

and

$$n = gN \exp\left(-\frac{\Delta G^f}{k_B T}\right). \tag{2.22}$$

If we express N in terms of concentrations of lattice sites N_{sites}, we can rewrite n and obtain an expression for the concentration at thermodynamic equilibrium,

$$c^{eq}(T) = gN_{sites} \exp\left(-\frac{\Delta G^f}{k_B T}\right). \tag{2.23}$$

It is clear from Eq. 2.23 that the key quantity to determine the concentration is the formation energy ΔG^f. Since the Gibbs free energy G can be expressed in terms of chemical potentials μ and number of particles N,[72]

$$G = \sum_i \mu_i N_i, \tag{2.24}$$

ΔG^f can be written as[70]

$$\Delta G^f_{q,D}(P,T) = F_{q,D}(V_D(P),T) - F_{bulk}(V_0(P),T) + P\Delta V^f(P) - \sum_s \Delta n_s \mu_s + q\mu_e, \tag{2.25}$$

where $F_{q,D}$ is the Helmholtz free energy of defect type D in charge state q, F_{bulk} is the reference energy of the bulk, Δn_s is the difference between the number of atoms of chemical species s in the defective system and in the bulk, and μ_e is the electron chemical potential. Moreover, V_D and V_0 are the volumes of the defective and the bulk cell, while ΔV^f denotes the defect formation volume (see Section 2.4.6). The free energies both include the contributions of vibrational, electronic, and magnetic entropy. However, these contributions are small compared to the configurational entropy and the computational cost to determine them is high. Therefore, they are typically neglected. Moreover, in Eq. 2.25, the thermal entropy contributions for the bulk and the defective system are assumed to be identical such that they completely cancel out, and the $P\Delta V^f$ term is neglected for solids.[73] In the following study, we will exclusively concentrate on the formation energy (zero temperature), where quasi-harmonic and anharmonic excitations are neglected. An accurate determination of these quantities not only requires

expensive calculations, but they are also assumed to be significantly smaller than the deviations introduced by the others approximations used to get to Eq. 2.25. Furthermore, in these materials, the defect concentration is primarily influenced by the configurational entropy.[74] In the following section we will address the current methodology to obtain formation energies with DFT.

2.4.2 The Supercell Method

The first requirement for obtaining the defect formation energies from Eq. 2.25 is to calculate the total energies of the defect and bulk configurations. In practice this can be achieved through a total energy calculation with DFT. Unlike the bulk case, the calculation of the defect provides several challenges. In fact, as we have seen in Section 2.2, the basis for the calculation is a unit cell which repeats periodically. Therefore, when we introduce a defect in the cell, we generate defect replicas as well, which will interact with each other (the finite-size effects will be discussed in more detail in Section 2.4.4). To circumvent the problem, the common approach is to perform the calculation in a supercell. A supercell describes a multiplication of the unit cell along its crystallographic axes, with periodic boundaries applied in all directions. In this way, the distance between the replicas is increased, thus decreasing the magnitude of their mutual interaction. On the other hand, this solution increases the computational cost, since calculations include a much larger number of atoms.
Once the total energies of the defect and bulk supercells have been computed, it is possible to obtain the formation energies. As we have addressed in Section 2.4.1, we can neglect the small contributions of electronic and vibrational entropy and the $P\Delta V^f$ term in Eq. 2.25, which allows to rewrite the formation energy in terms of the total energies obtained with DFT (E_D and E_{bulk})

$$\Delta E^f_{q,D}(\{\mu_s\},\mu_e) = E_D - E_{bulk} + E_{corr} + q(E_{VBM} + \mu_e) - \sum_s \Delta n_s \mu_s, \quad (2.26)$$

where E_{corr} is a correction term to account for the finite-size effects, which will be discussed in Section 2.4.4, and the μ_e has been referenced to the energy at the valence band maximum (E_{VBM}), obtained from the DFT eigenvalue of the highest occupied orbital.[75]
So far, we have only been addressing individual point defects, but single defects can also interact with each other and associate, thus forming a defect complex. The same formulation of the formation energy (Eq. 2.26) can be extended for defect complexes as well.[70] Another key quantity for complexes is their binding

energy, *i.e.* the energy difference between formation energy of the complex (C) and the sum of the formation energies of its isolated constituents (D),

$$E_b = \Delta E_C^f - \sum_D \Delta E_D^f. \tag{2.27}$$

A negative binding energy implies that the energy to create isolated defects is higher than that for forming a complex, which means that the interaction between defects is attractive and complex formation becomes thermodynamically advantageous. However, a negative binding energy indicates only that complexes can in principle be formed, but not necessarily that they will occur in sizable concentrations. The reason is the different configurational entropy of a pair of isolated defects versus that of a complex. For example, a complex consisting of two constituents can be formed in $\propto N_{sites} \cdot g$ configurations, where g is the number of equivalent configurations in which the defect can be incorporated (see Eq. 2.23), whereas if the two constituents are independently formed they can be created in $\propto N_{sites}^2$ configurations. It should also be noted that complex formation does not change the number and nature of participating species. Thus, the complex binding energy is independent of the chemical potential, which is confirmed by the formulation in Eq. 2.27.

2.4.3 Charge-Transition Levels

While formation energies are the essential quantity for the determination of equilibrium defect concentrations, charge-transition levels (also called ionization levels or thermodynamic transition levels) provide information about the charge state stability of the defect level with respect to the electron chemical potential. These quantities are useful to explain a temperature-dependent conductive behavior, including a change of the defect mobility with various charge states[76] or the formation of defect associates, where binding energies sensitively depend on the electrostatic and elastic interaction of the individual point defects.
The charge transition level refers to the electron chemical potential at which the formation energy of a given defect becomes equal at charge states q_1 and q_2, and is given by[70]

$$\varepsilon(q_1/q_2) = -\frac{\Delta E_{q_1,D}^f(0) - \Delta E_{q_2,D}^f(0)}{q_1 - q_2}, \tag{2.28}$$

where $\Delta E_{q,D}^f(0)$ is the formation energy of defect D in charge state q when the electron chemical potential is at the valence band maximum (VBM), μ_e = 0. This

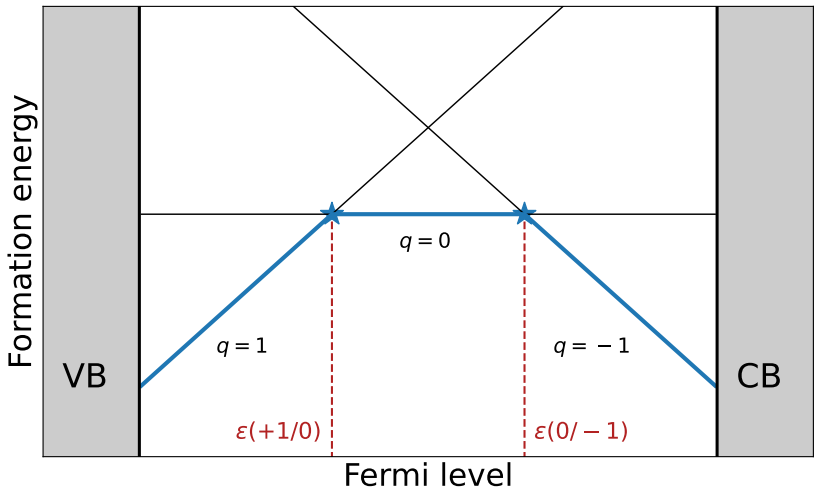

Figure 2.3: Schematic illustration of a formation energy plot for a single defect species in three different charge states ($q = +1, 0, -1$). The formation energies are shown as a function of the Fermi level. The thick blue line indicates the energetically most favorable charge state for a given Fermi level. The stars represent the charge transition levels. Conventionally, only the thick blue line is shown for a given defect specie.

value corresponds to the μ_e where the charge state stability of a defect species changes.

In the community, the electron chemical potential μ_e is also very often called "Fermi level" and the two names are absolutely equivalent. This, however, is often confused with the term "Fermi energy", which is the value of μ_e at 0 K ($\lim_{T\to 0K} \mu_e = \varepsilon_F$).[50] Conventionally, formation energies (Eq. 2.26) and charge-transition levels (Eq. 2.28) are plotted as a function of μ_e, as illustrated in Figure 2.3. In order to be consistent with the nomenclature used in other works regarding defect computations,[70,77,78] we choose to refer to μ_e as "Fermi level" (E_F), which in this context is a free parameter. We will refer to it as "electron chemical potential" when we treat it not as a free parameter, but a fixed value which determines the defect concentrations, derived self-consistently starting from the charge neutrality condition (see Section 2.4.7). From the dependency in Eq. 2.26, we obtain a line for every charge state, with slope equal to the charge q. For clarity, at each Fermi level value, only the line of the most stable charge state is shown, with the charge transition levels indicated by stars. If the charge transition level is located close to the conduction or valence band edge, it is called shallow. Otherwise, if $\epsilon(q_1/q_2)$ occurs at Fermi levels around the middle of the band gap, it is said to be a deep

charge transition level. We also notice from Eq. 2.28 that charge transition states do not depend on the chemical potentials $\{\mu_s\}$.

2.4.4 Finite-Size Effects

In the previous section, we have addressed the problems arising from the finite size of the supercell in defect calculations. In fact, the periodicity results in an artificial sublattice of defects with a lattice constant equal to the supercell's length. This has several consequences. Firstly, the point charge lattice leads to unphysical long-range Coulomb interactions between the images, imitating an exceedingly high defect concentration.[70,79] Secondly, a dense defect grid leads to elastic interactions and might allow for an artificial overlap (hybridization) between the wavefunctions of the periodic defect images. Lastly, a compensating background charge density has to be included such that a divergence of the energy is avoided. Several methods were proposed in order to deal with the various finite-size effects of point defects.[76,79–82] Most of the methods aim at obtaining the correct energies with already small supercell sizes in order to reduce the computational cost. Recently, two elegant methods have been proposed to calculate a correction in an *ab initio* fashion, using output data from the DFT calculation. The approach proposed by Freysoldt *et al*[83] expresses electrostatic interactions in terms of the unscreened charge density and the electrostatic potential. The defect potential is expressed as a sum of a long-range and a short-range part. The long-range contribution is associated to macroscopic screening, which is set to decay as $1/\varepsilon r$. The long-range electrostatic energy correction is thus determined by the summation of the Fourier transform of the long-range potential in real space over the reciprocal lattice vectors. Quantum effects are accounted for in the short-range part associated to microscopic screening. This is obtained by subtracting the long-range part to the electrostatic potential difference between defect and pure structures, obtained from the DFT calculations. The methodology is illustrated in Figure 2.4. If the defect is well localized in the supercell and a bulk-like macroscopic screening is achieved, the short-range potential will reach a plateau in between replicas of defects. The value of the potential in this plateu determines the potential alignment correction. The total correction to the formation energy is thus given by the sum of the alignment correction and the long-range electrostatic correction. This method has mainly two shortcomings. Firstly, aligning the planar-averaged electrostatic potential to the defect-induced potential works well when the atomic positions are fixed in unrelaxed crystalline positions. In fact, the defect-induced potential strongly fluctuates when the atomic displacements are

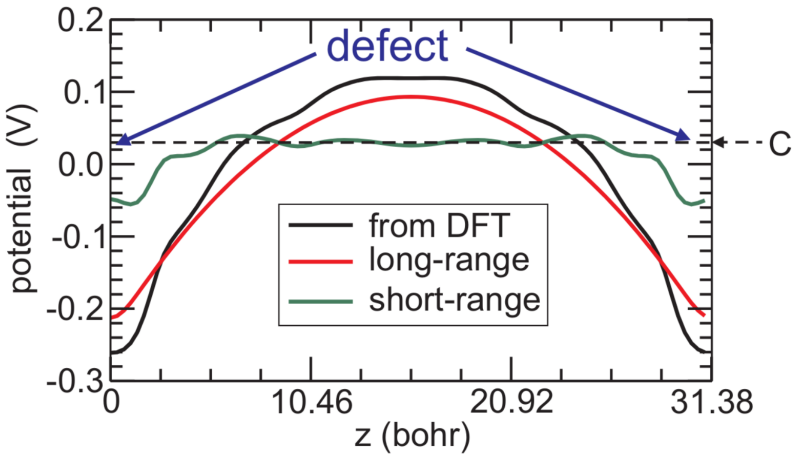

Figure 2.4: Example of the finite-size correction method proposed by Freysoldt *et al.* The x-axis is the distance between defect replicas, the defect is located at z = 0 bohr with a periodic image at z = 31.38 bohr. The defect potential is expressed as a sum of short- and long-range parts. The long-range screening is set to decay as $\propto 1/r$, the short-range quantum oscillations are obtained from DFT calculations. More details can be found in the original work in Reference 83.

large even far from the defect in the supercell. Since defect calculations require relaxation of atomic positions, the method needs to be applied using preliminary calculations as input, where the atomic positions are not relaxed. Secondly, the long-range Coulomb interaction is calculated with a macroscopic scalar dielectric constant. This is acceptable when diagonal components of a dielectric tensor are close to each other and off-diagonal components are relatively small.

To overcome these shortcomings, Kumagai *et al*[84] have extended the Freysoldt (FNV) approach. Their idea is to employ the atomic site potential for determining the potential offset between the defect-induced potential and point charge (PC) potential, as opposed to the planar-averaged potential. The atomic site potential is also a product of DFT. The potential is averaged at the atomic positions in the region outside of the sphere that is in contact with the Wigner-Seiz cell with radius R_{WS}, as illustrated in Figure 2.5. This region is denominated "sampling region". This approach also has the advantage that, if the Bravais lattice is unchanged, the sampling region does not depend on the choice of the supercell. Moreover, they describe a point charge model with a dielectric tensor for evaluating long-range Coulomb interactions, which accounts for anisotropy, whereas in the FNV scheme the long-range Coulomb interaction is screened by a scalar

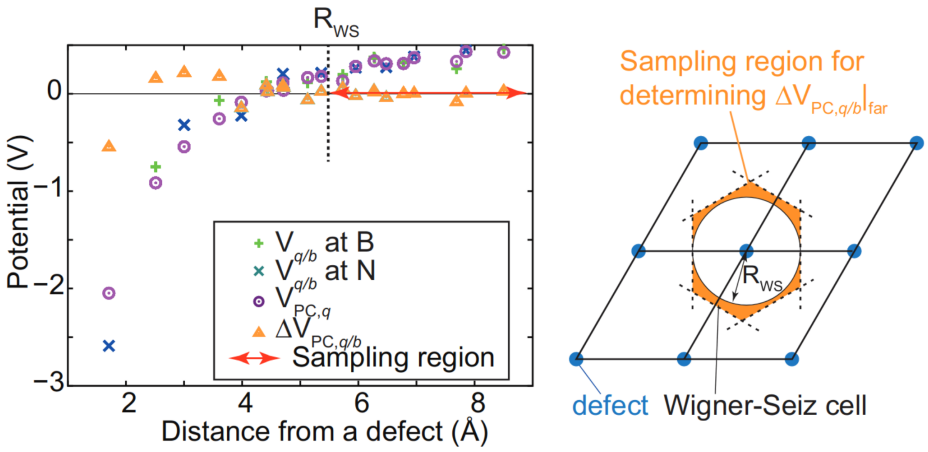

Figure 2.5: Example of the finite-size correction method proposed by Kumagai *et al.* The atomic site potential is used instead of the planar-averaged potential adopted by Freysoldt *et al.*[83] The potential is averaged at the atomic positions in the region outside the sphere that is in contact with the Wigner-Seiz cell with radius R_{WS}. More details can be found in the original work in Ref 84.

dielectric constant in an isotropic medium. In this work, we employed mainly the Kumagai method, while the FNV scheme was used to determine corrections for the cubic phase of $NaNbO_3$ (Section 3.1).

2.4.5 Chemical Reservoirs and Stability Diagram

The calculation of defect formation energies in Eq. 2.26 requires the definition of the set of chemical potentials $\{\mu_s\}$. The chemical potential of a species s is defined as the variation of a thermodynamic potential of the system with respect to a change in particle number of the given species[72]

$$\mu_s = \left(\frac{\partial U}{\partial N_s}\right)_{S,V,N_{i\neq s}} = \left(\frac{\partial H}{\partial N_s}\right)_{S,P,N_{i\neq s}} = \left(\frac{\partial F}{\partial N_s}\right)_{T,V,N_{i\neq s}} = \left(\frac{\partial G}{\partial N_s}\right)_{T,P,N_{i\neq s}}, \tag{2.29}$$

where N_s is the total number of particles of species s. The chemical potential can be rewritten as

$$\mu_s = \mu_s^{ref} + \Delta\mu_s, \tag{2.30}$$

where μ_s^{ref} denotes the chemical potential of the constituent element in its stable elemental phase, which can be calculated with DFT by dividing the total energy

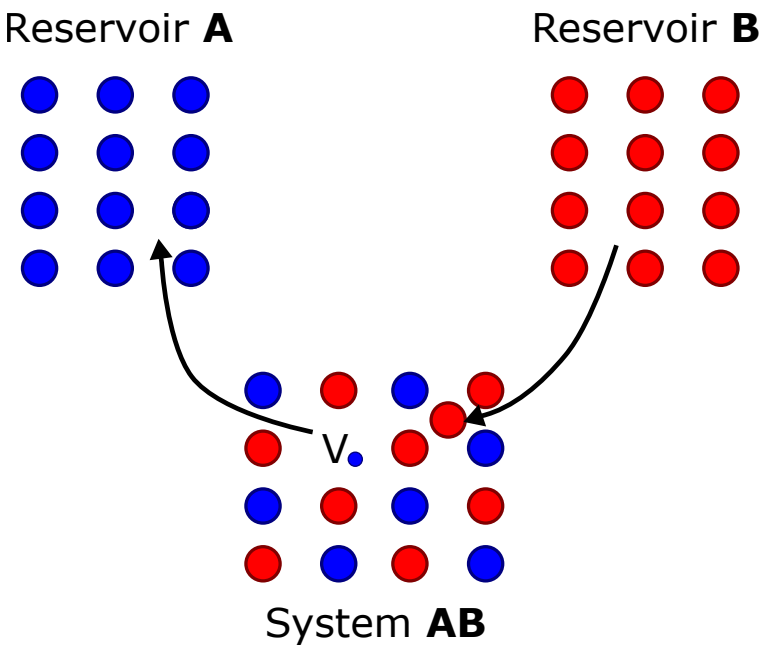

Figure 2.6: Sketch of the particle exchange in the process of defect formation. The atom of type A leaves a vacancy in the system AB and moves to reservoir A (Δn_A = -1). Similarly, an atom of type B leaves the reservoir B to create an interstitial in the system AB (Δn_B = +1). In both cases the chemical potential of the elements are defined by the reservoirs the system is in contact with.

by the number of particles in the unit cell. The term Δn_s in Eq. 2.26 refers to an exchange of particles between our system and the thermodynamic reservoirs that it is in contact with, as sketched in Figure 2.6.

One possible way to define the chemical reservoirs is to look at the limits of stability of the phase of interest. In order to achieve this, we need to know the phase stability as a function of the chemical potential of the constituents, which means we need to calculate the phase diagram. The starting point is the calculation of the formation energies of all possible competing phases, which is the difference in total energy between the phase of interest and the elemental phases

$$\Delta E^f = \epsilon - \sum_s c_s \epsilon_s, \tag{2.31}$$

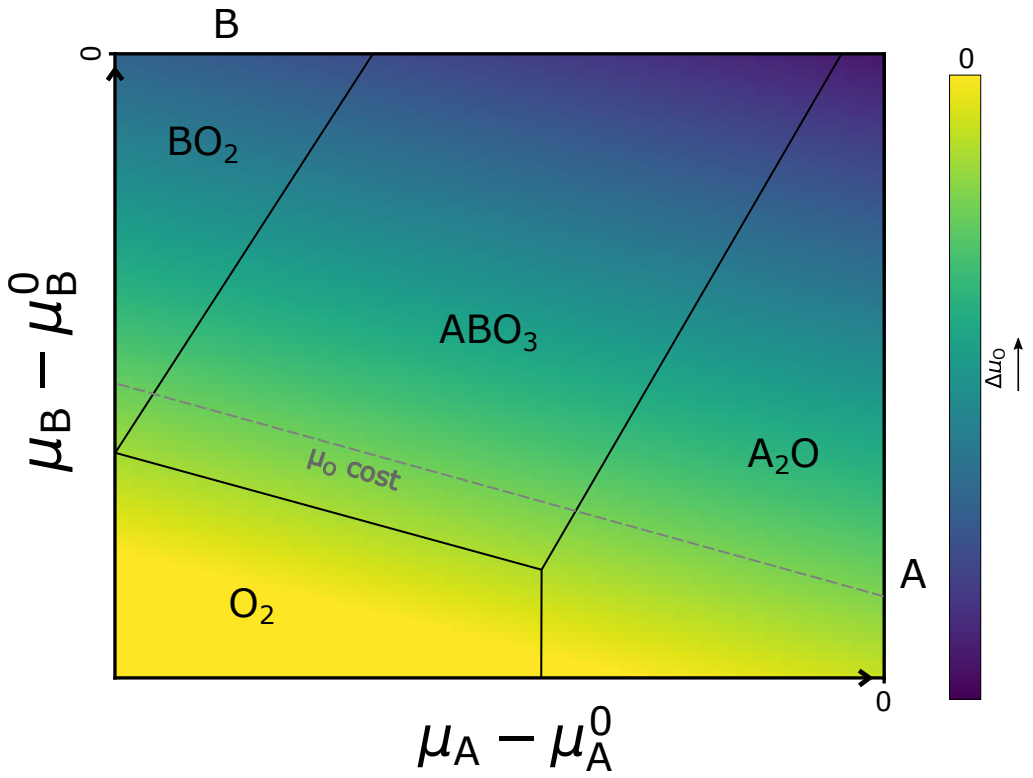

Figure 2.7: Example of a stability diagram for a generic ternary compound ABO_3. The two axis are the chemical potentials of A and B referenced to their elemental phases (Eq. 2.30), which by definition range from zero to negative values. The heatmap shows the chemical potential of the element O, which for fixed μ_A and μ_B is determined by Eq. 2.32. The labelled regions indicate the regions of stability of each phase, while the lines indicate the zone of coexistence of two or more phases. Fixing a value of one chemical potential removes one degree of freedom, yielding a linear dependency between the other chemical potentials, as shown by the dashed grey line.

where s indicates the elements in the target phase, c_s represents the stoichiometric coefficients, and ϵ is the total energy per formula unit. The formation energy can be written also in terms of the chemical potential of the constituents (Eq. 2.30)

$$\Delta E^f = \sum_s c_s \Delta\mu_s, \tag{2.32}$$

which introduces a condition in the range of the chemical potentials for the stability of the target phase. Moreover, the stability range is further limited by

the presence of competing phases. More specifically, the chemical potentials have to satisfy the condition

$$\sum_s c_s \Delta\mu_s \leq \Delta E^f[c.p.] \ , \quad \forall \ c.p. \ , \tag{2.33}$$

where $c.p.$ indicates any competing phase. These relations allow to predict which phase is stable for a given set of chemical potentials. Or, to put it differently, they permit to determine the range of chemical potentials for which our target phase is stable. We can visualize these stability regions by constructing the stability diagram. An example for a generic ternary diagram with elements A, B and O is shown in Figure 2.7. Because of the condition in Eq. 2.32, for our ternary system we have only two degrees of freedom, *i.e.* once we choose $\Delta\mu_A$ and $\Delta\mu_B$, $\Delta\mu_O$ is obtained from the value of ΔE^f. Conventionally, if we are in presence of oxygen, μ_O will be the chosen one to be excluded from the plot. Because of the way $\Delta\mu$ is defined (Eq. 2.30), the two axis can range from zero to negative values. If $\Delta\mu$ is zero, it means the reference elemental phase is stable. The labelled regions in the plot indicate the range of chemical potentials in which each phase is stable. The lines separating the regions give the chemical potential values in which two or more phases can coexist. Moreover, if we choose to fix the value of one chemical potential, $\Delta\mu_O$ for example, we are left with only one degree of freedom, and Eq. 2.32 restricts the possible values to a line (as shown by the grey dashed line in Figure 2.7). Lastly, for completeness, the heatmap indicates the values of $\Delta\mu_O$, which for each point in the diagram are determined by the other two chemical potentials.

As mentioned previously, a possible approach to define the set of chemical potentials for defect calculations is to choose the stability boundary in the target phase. In our example, choosing ABO_3 as the target phase, this means four different sets of μ for every corner of the quadrilateral where ABO_3 is stable. The motivation is to provide a complete picture of the edges of stabilty of the target phase, knowing that the situation in the experiment will lie somewhere in between.

It is also of interest to evaluate the formation energies using a thermodynamic reservoir that represents as much as possible the experimental conditions. The methodology to achieve this is described in the next paragraph.

Oxygen Chemical Potential

In the case of oxides, the parameters controlled experimentally are usually temperature and oxygen partial pressure (p_{O_2}). For a reversibly compressed ideal gas, we can express the chemical potential as[85]

$$\mu(T,p) = \mu(T,p^0) + k_B T \ln\left(\frac{p}{p^0}\right), \tag{2.34}$$

where k_B is the Boltzmann constant, T the temperature, p^0 is a reference value for the pressure and $\mu(T,p^0)$ is the chemical potential value at pressure equal to p_0. This relation can be used to relate the oxygen chemical potential with temperature and partial pressure, still keeping in mind that we are approximating oxygen to an ideal gas. Therefore, Eq. 2.34 becomes[86,87]

$$\mu_O(T,p_{O_2}) = \mu_O(T,p^0) + \frac{1}{2}k_B T \ln\left(\frac{p_{O_2}}{p^0}\right), \tag{2.35}$$

where p_{O_2} is the oxygen partial pressure, and the factor $1/2$ accounts for the fact that oxygen is a biatomic molecule. Following Ref. 86, we write the temperature dependence of the reference chemical potential $\mu_O(T,p^0)$ as

$$\mu_O(T,p^0) = \mu_O(0\ K,p^0) + \Delta\mu_O(T,p^0), \tag{2.36}$$

where $\mu_O(0K,p^0)$ is half the computed energy of the isolated O_2 molecule at 0 K, and $\Delta\mu_O(T,p^0)$ is the variation in chemical potential with temperature at standard pressure. The latter can be determined using thermochemical tables,[88] as shown by Reuter *et al.*[86] They have extracted the values of $\Delta\mu_O(T,p^0)$ at different temperatures, which we report here in Table 2.2 and show in Figure 2.8. With a linear fitting we can then extrapolate the value for the desired temperature. Therefore, with these tools it is possible to obtain the oxygen chemical potential starting from its partial pressure in the experimental conditions, or alternatively to evaluate the defect concentrations and the electron chemical potential as a function of the oxygen partial pressure, which is useful to compare the results with experimental data.

2.4.6 Relaxation Volume

Similarly to the formation energy, the formation volume is an important characteristic, influencing the concentration, the diffusion, the segregation of a defect,

Temperature (K)	$\Delta\mu_O(T, p^0)$ (eV)
100	-0.08
200	-0.17
300	-0.27
400	-0.38
500	-0.50
600	-0.61
700	-0.73
800	-0.85
900	-0.98
1000	-1.10

Table 2.2: Variation with temperature of the chemical potential at standard pressure, as determined from thermochemical tables by Reuter *et al* from Reference 86. The value for the desired temperature can be extrapolated with a linear fitting.

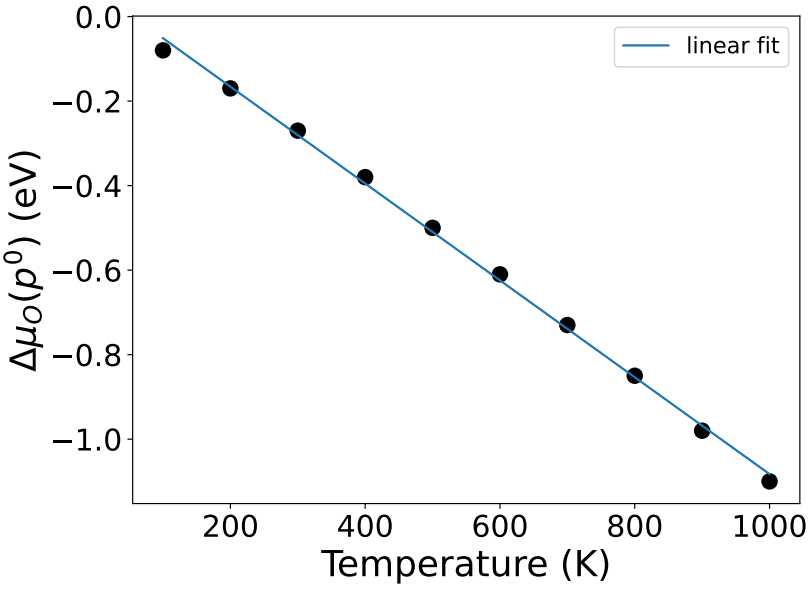

Figure 2.8: Variation with temperature of the oxygen chemical potential at standard pressure, as determined from thermochemical tables by Reuter *et al* from Reference 86.

or, more generally, the evolution of the microstructure.[89] Its general definition can be derived from the formation energy (Eq. 2.25) as

$$\Delta V^f = \left(\frac{\partial \Delta G^f(P,T)}{\partial P} \right)_T . \tag{2.37}$$

The formation volume describes a finite, macroscopic volume change after introducing a defect D of charge state q into the system. It can also be defined as

$$\Delta V^f = V(D_q) - V_{bulk} \pm V_0, \tag{2.38}$$

where V_{bulk} is the volume of the host, $V(D_q)$ is the equilibrium volume of the defective cell, and V_0 is the volume of a single atom in the pristine supercell. The plus sign applies in the case of a vacancy, while the negative sign refers to interstitials. We can express V_f in terms of the relaxation volume ΔV^r,

$$\Delta V^r = V(D_q) - V_{bulk}, \tag{2.39}$$

$$\Delta V^f = \Delta V^r \pm V_0. \tag{2.40}$$

These two quantities relate to different properties: the relaxation volume can be related to the lattice parameter change induced by a point defect, whereas the formation volume is related to the macroscopic volume change induced by the defect. For non-elemental solids, formation volumes of composite intrinsic defects such as Frenkel pairs, Schottky defects, etc., can be defined by relevant combinations of relaxation volumes. Moreover, the relaxation volume gives an estimate on the elastic interaction with other defects or external strain.[89] If we limit the equation of state of the system to its bulk modulus (B) dependence, and assuming that the effect of the defect on the bulk modulus is negligible, the relaxation volume can be calculated as follows,[90]

$$\Delta V^r \approx \frac{P\, V_{bulk}}{B}, \tag{2.41}$$

where P is the internal pressure calculated at the equilibrium volume of the host. The pressure of a system with charge state q is defined as

$$P(q) = -\frac{\partial E(q)}{\partial V}, \tag{2.42}$$

where $E(q)$ is the total energy of the system with charge q. Since q values are relatively small, we can write the total energy as a Taylor expansion with respect to the charge

$$P(q) = -\frac{\partial}{\partial V}\left(E(0) + q\frac{\partial E}{\partial q} \right). \tag{2.43}$$

The term $-\partial E(0)/\partial V$ is the pressure of the neutral cell $P(0)$. We can rewrite the second term using the relation $q = Z - N$, where Z is the number of positive charges from the nuclei and N is the number of electrons

$$\frac{\partial E}{\partial q} = -\frac{\partial E}{\partial N}. \tag{2.44}$$

The derivative of the energy with respect to N can be expressed using Janak's theorem[75]

$$\frac{\partial E}{\partial n_i} = \epsilon_i, \tag{2.45}$$

where n_i is the occupation of Kohn-Sham eigenstate i and ϵ_i its energy. We obtain

$$P = P(0) + q\frac{\partial \epsilon_i}{\partial V} = P(0) + \frac{q}{V}\frac{\partial \epsilon_i}{\partial \ln V}. \tag{2.46}$$

We call the last term deformation potential

$$a_i = \frac{\partial \epsilon_i}{\partial \ln V}, \tag{2.47}$$

which gives

$$P(q) = P(0) + \frac{q}{V}\, a_i. \tag{2.48}$$

Because of the impossibility of uniquely defining the electrostatic potential within periodic boundary condition, the origin of the energy scales for the eigenvalues is arbitrary. Its variation with respect to the volume is also arbitrary. As a consequence, the deformation potentials in Eq. 2.47 are convention dependent, which increases the complexity of the problem. One possible solution is the definition of an absolute deformation potentials (ADP) using the natural band offset approach.[91] More recently, Bruneval *et al*,[90] proposed an alternative procedure to calculate defect relaxation volumes without prior knowledge of the absolute deformation potential. Their approach relies on the formation of a charge-neutral group by including charge compensating defects, for instance, free holes or electrons, self-trapped holes, and charged vacancies.
So far, we have only presented an introduction to the complexity of the problem of computing relaxation volumes for charged defects with DFT. In this thesis, the effects of defects on strain and elastic properties is not the main focus. We have therefore limited the analysis on the relaxation volumes for neutral defects, where the calculation of a_i is not needed. For a more comprehensive overview of

the theory and methodology, we recommend looking into Ref. 89–93.
The pressure can be computed from the residual stress tensor, which is a by-product of a standard DFT calculation. However, to ensure that the point defect solely causes residual stress after atomic relaxation and largely exclude numerical errors, the residual stress of the bulk cell should be subtracted from the tensor of the defective cell. This quantity is further used to determine the elastic dipole tensor[94]

$$P_{ij} = -V_0 \langle \sigma_{ij} \rangle, \tag{2.49}$$

where $\langle \sigma_{ij} \rangle$ is the residual stress tensor, and V_0 is the supercell volume, which can then be used to determine the relaxation volume in Eq. 2.41.

2.4.7 Charge Neutrality Condition

As previously discussed in Section 2.4.1, in spite of the methodology for plotting the formation energies, μ_e is not a free parameter. The determination of this quantity is a key aspect of a defect thermodynamics study. In fact, its value determines the defect concentrations, the concentration of charge carriers, the conductivity, the charge transition levels, etc. We can compute μ_e by solving the charge neutrality condition[50]

$$n_e + n_A = n_h + n_D, \tag{2.50}$$

where n_e and n_h are respectively the electron and hole carrier concentrations, and n_D and n_A are respectively the concentrations of donors and acceptors. This equation essentially imposes that the system as a whole is not charged, and positive and negative charges compensate themselves. The motivation is that a charged system would be energetically unfavorable. Given different defect species (D) in different charge states (q), Eq. 2.50 can be expressed as

$$\sum_{q,D} q \cdot [D_q] - n_e + n_h = 0, \tag{2.51}$$

where $[D_q]$ is the concentration of defect D in charge state q, defined in Eq. 2.23. The concentrations of intrinsic carriers are derived by integrating the number of unoccupied states up to the VBM ($\mathrm{E_{VBM}}$) for holes[50]

$$n_h = \int_{-\infty}^{E_{VBM}} D(\epsilon)[1 - f(\epsilon)]d\epsilon, \tag{2.52}$$

and the number of occupied states from the conduction band minimum (CBM) (E_{CBM}) for electrons

$$n_e = \int_{E_{CBM}}^{+\infty} D(\epsilon) f(\epsilon) d\epsilon, \tag{2.53}$$

where $f(\epsilon)$ is the occupancy probability and $D(\epsilon)$ is the density of states. Since electrons are fermions, the occupancy function is the Fermi-Dirac distribution,[50]

$$f(\epsilon, \beta, \mu_e) = \frac{1}{e^{\beta(\epsilon - \mu_e)} + 1}, \tag{2.54}$$

where β is $1/k_B T$. The density of states $D(\epsilon)$ is the number of states available for occupation for each energy value per unit volume, and can be calculated with DFT. Having linked the concentration of charge carriers to temperature and electron chemical potential, we can rewrite Eq. 2.50 as a function of T and μ_e

$$\sum_{q,D} q[D_q](T, \mu_e) - n_e(T, \mu_e) + n_h(T, \mu_e) = 0, \tag{2.55}$$

$$\sum_{q,D} q N_D e^{-\beta \Delta E^f_{q,D}(\mu_e)} - \int_{E_{CBM}}^{\infty} D(\epsilon) f(\epsilon, \beta, \mu_e) d\epsilon \tag{2.56}$$

$$+ \int_{-\infty}^{E_{VBM}} D(\epsilon)[1 - f(\epsilon, \beta, \mu_e)] d\epsilon = 0. \tag{2.57}$$

Knowing the value of the temperature, we can solve this equation self-consistently, which determines the value of μ_e for which the charges are balanced. More details on how to do this in practice will be given in Section 2.5. Once we have solved the equation and know μ_e, we can determine the equilibrium concentrations of defects and charge carriers.

In order to better correlate with the experiments, this analysis is usually carried out at different oxygen partial pressures (p_{O_2}), using the correlation between chemical potential and partial pressure described in Section 2.4.5. Therefore, equilibrium concentrations of defects and charge carriers are usually visualized as a function of p_{O_2}. These graphs are called Brouwer diagrams (sometimes also called Kröger and Vink diagrams).[95–98] A generic example is shown in Figure 2.9. This case involves a doubly negatively charged acceptor defect (A) and a doubly positively charged oxygen vacancy (V_O). In low p_{O_2} regimes, the formation energy of V_O is lower than for A. Thus, oxygen vacancies dominate and the concentrations of electrons (n_e) is bigger than the concentration of holes (n_h). The electron chemical potential will therefore be closer to the CBM than

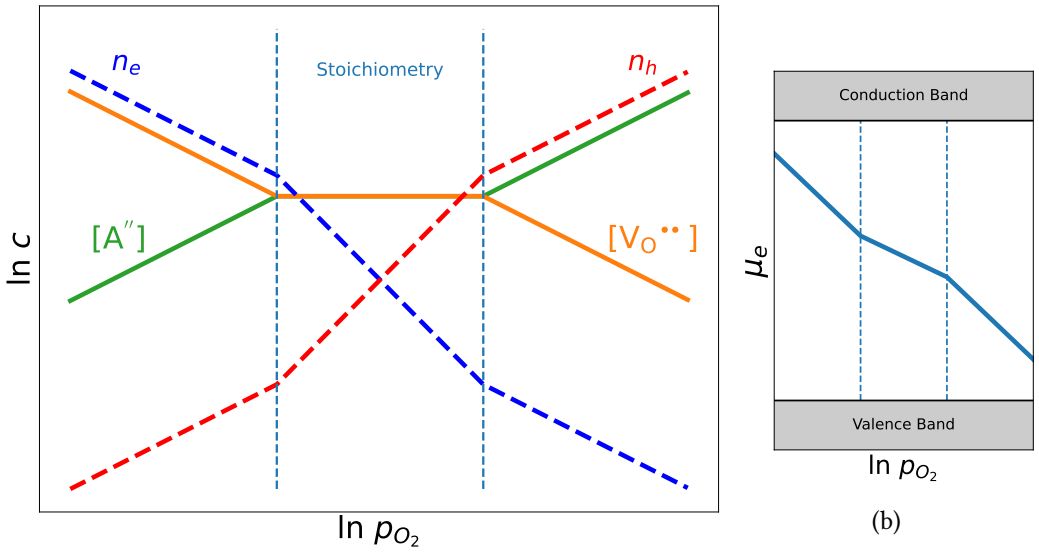

Figure 2.9: **a)** Example of a Brouwer diagram involving an acceptor A ($q = -2$) and donor V_O ($q = +2$) and **b)** electron chemical potential μ_e as a function of the oxygen partial pressure. At low p_{O_2}, the formation energies of V_O are smaller than for A, which means the concentrations of electrons exceeds the one of the holes ($n_e >> n_h$), and μ_e is pushed close to the CBM. For high p_{O_2} the situation is the opposite ($n_h >> n_e$), and μ_e is pushed towards the VBM. In the middle region we have $[A] = [V_O]$, which means the equilibrium μ_e is in the middle of the gap.

the VBM, meaning the semiconductor is n-type.[50] The exactly opposite situation occurs in high p_{O_2} regions. The concentration of acceptor dominates, $n_h >> n_e$, and the semiconductor is p-type. In the middle region, A and V_O can form with equal probability, meaning that they are present in equal concentration, as for the concentrations of electrons and holes. Consequently, in this region μ_e will be close to the middle of the band gap.
It is worth noticing that, in our didactic example in Figure 2.9a, the linearly dependent concentrations and the distinguished p_{O_2} regions are a consequence of approximations. In fact, in the method proposed by Brouwer and extended by Kröger and Vink,[95] some approximations are made in order to facilitate the solution of the charge neutrality equation. In particular, based on the p_{O_2} region, some concentrations are assumed to be large enough to make the others negligible. The validity of these approximations must be then verified *a posteriori*. We

have shown this version of the diagram to simplify the explanation of how defect equilibrium changes with p_{O_2}, keeping in mind that this is the example often used in the literature.[95] In this work, however, we have no need to employ any concentration approximation, as we can solve the charge neutrality equation including all defects and all charge states simultaneously, and knowing the density of states from DFT we can compute accurately the concentrations of electrons and holes.

2.4.8 Defect Quenching

In the methodology we have described in the previous section, the defect concentrations in the charge neutrality equation (Eq. 2.50) depend exclusively on temperature and electron chemical potential (Eq. 2.57). Therefore, the treatment of defect populations that has been presented so far is based on the hypothesis that the material and the reservoirs are in thermodynamic equilibrium. This means that the mobility of defects is large enough to allow compositional variations to be brought about by diffusive processes in the bulk.[95] It is generally accepted that the respective time constants required to achieve equilibration of atomic and electronic defects are comparatively long and short. Thus, in quenched systems, materials may retain the atomic defect concentrations imposed at high temperature, while the electronic defects continue to equilibrate.[98] Experimentally, the synthesis of materials often relies on quickly cooling down the sample, in order to preserve its high temperature state down at room temperature. This requires that quenching is accounted for in a theoretical and computational model which studies defect thermodynamics. A first possible approach to tackle the problem is to compute μ_e at high temperature, compute the defect charges in the high temperature equilibrium and fix them at low temperature, as proposed by Canepa *et al.*[99] The problem with this approach is that the charge states of the defects are assumed to be constant. Since charge carriers have enough mobility to diffuse and equilibrate when temperature is decreased, shifting μ_e due to a temperature change and/or a phase transformation can affect the charges the defects can assume. Hence, even if their concentration is fixed, their contribution to the charge neutrality can be completely different from one condition to the other.
We encounter a similar problem when treating extrinsic defects. In the experimental world, when chemical doping/substitution is performed, the concentration of extrinsic defects inside the sample is going to be fixed from the synthesis stage. The common approach, in this context, is to guess the charge state of the

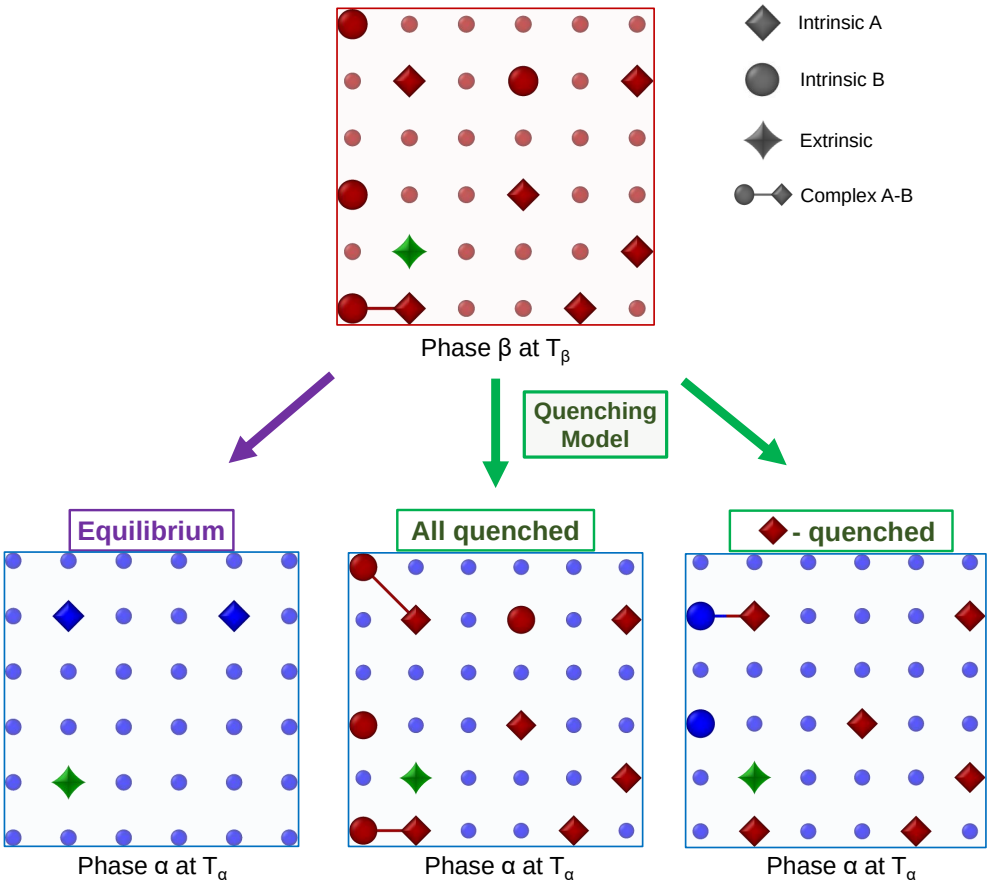

Figure 2.10: Schematic representation of the different conditions our quenching model can explore. A defect distribution equilibrated in an initial phase β at temperature T_β can be quenched in a different phase α at temperature T_α. Quenching can involve all defect species or just a subset, letting the rest equilibrate in the target conditions. The charge states of the quenched defects still depend on temperature and electron chemical potential in the target phase. Defect complexes depend on the concentrations of single defects but are still allowed to associate and dissociate, with probability depending on their binding energy in the target phase. The concentrations of extrinsic defects are fixed to the experimental values, but their charge states still depend on temperature and electron chemical potential in the target phase as for intrinsic defects.

doped system, by referring to chemical reactions derived from the most common oxidation states of the substituting element. Subsequently, its contribution to the charge neutrality condition is added as $q \cdot [D_{fix}]$, where q is the charge of the extrinsic defect and $[D_{fix}]$ is the fixed concentration.[87] Also in this case, the charge state dependency on T and μ_e of the extrinsic defect has been completely neglected. While generally the oxidation states can be a proper descriptor, we might also encounter a situation where the dopant's charge behaves in an unexpected way, or simply the assumed charge is not the most stable one for all T and μ_e values.
In this work, we have employed a novel scheme to solve both of these problems, namely to allow to fix defect concentrations (both intrinsic and extrinsic) without neglecting the dependency of the charge states on phase, temperature and electron chemical potential. We start from the approach employed by Shousha *et al*[100] and Lee *et al*,[101] and we show how this model can be extended to account for extrinsic defects and defect complexes as well, without introducing additional *a priori* assumptions.
As already introduced in Section 2.4.7, the total charge associated with a generic defect species D is given by

$$Q_D = \sum_q q \cdot [D_q], \tag{2.58}$$

where q is the charge state and $[D_q]$ is the concentration of defect D in charge state q. We introduce the quantity $[s]$, which is the total concentration of element s (or a vacancy of the element) across all defect species. Therefore, it is the sum of the concentrations of defect species d which contain s, in all of their possible charge states q

$$[s] = \sum_{d,q} [d_q] = \sum_{d,q} N_d e^{-\beta E_{d,q}}, \tag{2.59}$$

where β is equal to $1/k_B T$ and $E_{d,q}$ is the formation energy of defect d in charge state q, as defined in Section 2.4.1, (the symbol "Δ^f" has been removed to lighten the notation). If we divide and multiply $[D_q]$ by $[s]$ we can explicate the term

$$w_{D,q}(\mu_e, T) = \frac{[D_q]}{[s]} = \frac{N_D e^{-\beta E_{D,q}}}{\sum_{d,q} N_d e^{-\beta E_{d,q}}}, \tag{2.60}$$

which depends on temperature and μ_e and represents the weight of the concentration of defect D in charge state q with respect to the total concentration of the element. Having rewritten $[D_q]$ as $w_{D,q}(\mu, T)\,[s]$, it is possible now to assume

that, in "fixed" conditions, the total concentration of the element s is equal to the target value of $[s^{fix}]$, which in practice might be a high-temperature concentration value arising from quenching, or the fixed concentration of a dopant. In this way it is possible to compute the concentration of defect D in charge state q in "fixed" conditions, without neglecting its temperature and μ_e dependence and/or performing further assumptions,

$$[D_q^{fix}] = w_{D,q}(\mu, T)\ [s^{fix}] = [D_q] \cdot \frac{[s^{fix}]}{[s]}. \tag{2.61}$$

By doing so we rely on the behaviour that the defect would show if it was allowed to equilibrate with its reservoir, but we constrain its concentration to a target value.
The same approach can be extended to describe defect complexes. The complex is treated as an independent defect specie. Like in Eq. 2.58, the charge associated to complex C in charge q is given by

$$Q_C = \sum_q q \cdot [C_q], \tag{2.62}$$

and its concentration in equilibrium conditions, following Eq. 2.23, is given by $N_C e^{-\beta E_{C,q}}$, where $E_{C,q}$ is the formation energy and N_C is the site multiplicity of the complex. It is possible to write $[C_q]$ in terms of the formation energy of the single defects (E_D) that constitute the complex and its binding energy (Eq. 2.27). We add and subtract to $E_{C,q}$ the term $\sum_D E_{D,q}$,

$$[C_q] = N_C \exp\left[-\beta(E_{C,q} - \sum_D E_{D,q} + \sum_D E_{D,q})\right]. \tag{2.63}$$

We can thus substitute the expression of the binding energy:

$$E_b = E_{C,q} - \sum_D E_{D,q}. \tag{2.64}$$

We obtain

$$[C_q] = N_C\ e^{-\beta E_b} \prod_D e^{-\beta E_{D,q}} = N_C\ e^{-\beta E_b} \prod_D \frac{[D_q]}{N_D}. \tag{2.65}$$

It is worth noticing that the charge states of the single defects chosen for the expression of the binding energies are equivalent, as long as they are consistent

in the definition of the binding energies. Following the same approach used for single defects in Eq. 2.60, we can rewrite $[C_q]$ as

$$[C_q] = N_C \, e^{-\beta E_b} \prod_D [s] \frac{w_{D,q}}{N_D}. \tag{2.66}$$

Out of the species from which the complex is made, we define the subset of defects whose concentrations need to be fixed (named D^f). In this way, we can perform the same assumption as in the case of single defects, namely we substitute $[s]$ with $[s^{fix}]$ for the species belonging to the subset D^f, while nothing changes for the remaining subset of species which are allowed to equilibrate with the reservoir (D^e). We obtain

$$[C_q^{fix}] = N_C e^{-\beta E_b} \prod_{D \in D^e} [s] \frac{w_{D,q}}{N_D} \prod_{D \in D^f} [s^{fix}] \frac{w_{D,q}}{N_D}. \tag{2.67}$$

Comparing Eq. 2.66 and Eq. 2.67, we can rewrite $[C_q^{fix}]$ as

$$[C_q^{fix}] = [C_q] \cdot \prod_{D \in D^f} \frac{[s^{fix}]}{[s]} = N_C e^{-\beta E_{C,q}} \cdot \prod_{D \in D^f} \frac{[s^{fix}]}{[s]}. \tag{2.68}$$

By expressing $[C_q^{fix}]$ as in Eq. 2.68, we leave the expression for the concentration of the complex unchanged, still depending on its formation energy and without relying explicitly on the binding energy. Simply, it is enough to correct the equilibrium value with the factor $[s^{fix}]$ / $[s]$ for the species with fixed concentration, in a similar fashion to Eq. 2.61.
Figure 2.10 summarises all the different conditions this model can explore. The schematic lattice in the top figure represents the starting conditions, which in the case of quenching is usually a phase stable at high temperature (phase β at temperature T_β). Once the defect distribution in this system has been computed, it can be used to evaluate how a different phase (α) at a lower temperature (T_α) reacts when all defects, or a subset of defects, are frozen in from the high temperature phase. In fact, following Eq. 2.61 and Eq. 2.68, it is possible to quench only a subset of defects, while letting the rest equilibrate. This can be particularly useful in case some defects are particularly mobile, and therefore the original defect distribution is not preserved during the cooling process. Moreover, even if the concentrations of single defects are fixed, defect complexes can still form and dissolve, and the association probability is dependent implicitly on the binding energy, as computed in the target phase (phase α at temperature T_α). Lastly, the

concentration of extrinsic defects is hold constant to the experimental value in all conditions, but their charge state is allowed to equilibrate with temperature and electron chemical potential.

2.5 Analysis Framework

In the following section we provide a brief overview of the workflow to perform *ab initio* defect calculations and analysis. In most cases, these computations are systematic, *i.e.* the same procedures are used independently of the specific material of interest. Therefore, during this doctoral work, we have developed a set of tools to provide a systematic and rapid framework to study defect thermodynamics. The code is based on the language `python`, and it can be found on GitHub and the Python Package Index (PyPI). The library is largely based on the pymatgen package.[102]
The workflow is shown in Figure 2.11. The physics involved in these methods is summarised in Section 2.2 and 2.4. The starting point is the computation of the bulk phase, in order to obtain the relaxed structure with DFT (atomic positions and lattice parameter). Moreover, a static calculation with a more dense k-mesh is required to get a more accurate band gap (E_g) and density of states (DOS). Lastly, if finite-size corrections are needed, the calculation of the dielectric constant (FNV method) or the dielectric tensor (Kumagai method) is required (Section 2.4.4). Starting from the relaxed bulk structure, we create the supercell structures for the defects of interest, setting up one separate calculation for every desired charge state. We then perform total energy calculations, relaxing the atomic positions while keeping the lattice parameter fixed. Additionally, since we need the chemical potentials of the atomic species involved in the defects, we calculate the stability diagram of the phase of interest. At this point, the remaining parts of the workflow are just to analyse the DFT data and do not involve other DFT calculations. Once we possess both the relaxed bulk and defect structures, we can compute the finite-size corrections. In this work we have used the FNV and Kumagai methods, but also other methods can be used (Section 2.4.4). Finally, we can combine all of these results to compute our database of formation energies, which is the building block for the subsequent analysis. In fact, by solving the charge neutrality equation (Eq. 2.57), we calculate the electron chemical potential and defect concentrations at thermodynamic equilibrium. Last but not least, we can generate a new set of chemical potentials corresponding to a different oxygen

partial pressure (p_{O_2}) and repeat the whole procedure. In this way, we obtain the concentration and μ_e profiles as a function of p_{O_2} to generate the Brouwer diagram.
It is also possible to go one step further, and compute the diffusion barriers of the defects with the NEB method (Section 2.3), which can then be used to compute the conductivity of the system. This, however, goes beyond the scope of this work and will not be treated in this thesis.
In the following, we give a short introduction on how to handle the workflow with `pynter`. If the reader has no interest in understanding and/or using the software, we recommend skipping the next section entirely and moving directly to next section (Section 2.6).

DFT - Inputs and Outputs

In this work, all the calculations have been performed using the Vienna *ab-initio* simulation package (VASP),[103–106]. The `vasp` module allows to handle VASP calculations directly with python. The central module is `vasp.jobs` which allows to set up, read and run VASP jobs with the `VaspJob` class and the `VaspJobNEB` class for NEB calculations. Input files can be prepared using the `vasp.default_inputs` module. Moreover, if more complicated calculation schemes are involved, a set of calculations can be set up automatically with the `vasp.schemes` module. Useful schemes for defect calculations can be set with the `AdvancedSchemes` class. Since almost all DFT calculations need to be run on multiple cores, given the required computational power, we have developed an `ssh` interface with a cluster which uses the `slurm` queuing system. Once calculations are performed, the `VaspJob` objects can be extracted directly from the calculations directories. When multiple calculations in subdirectories are involved, they can be handled (both for inputs and outputs) simultaneously with the `Dataset` class in the `data.datasets` module. Lastly, the `vasp` module includes tools for analysis and plotting, *e.g.* DOS, band structure, Birch-Murnaghan fits, k-points and energy cutoff convergence, *et cetera*. For convenience, the job objects can be saved as `json` files, which allows to quickly recall them without needing to access the original data again.

Defects Database

The `defects` module collects the tools to organize and analyse defect calculations. Schematics of the most important classes and relative workflow are

shown in Figure 2.12. The first step is to create defect entries from the DFT data, using the `DefectEntry` class. The class can either be initialized by inserting the data directly by hand, or automatically from `VaspJob` objects. Any correction to the total energy needs to be included at this stage. The module `defects.corrections` provides functions which allow to compute FNV or Kumagai corrections using pymatgen,[102] which can also be run automatically starting from the job objects of defects and the bulk phase.
Defect entries are then organized into a database with the `DefectsAnalysis` class, which is the central class for the whole workflow. This contains functions to compute and plot quantities both dependent and independent of the chemical potential (charge transition levels, defect complex binding energies, electron chemical potential and formation energies). The electron chemical potential can be computed both in equilibrated and quenched/doped conditions (Section 2.4.8) with the `solve_fermi_level` function. Both `DefectEntry` and `DefectsAnalysis` objects can be stored as `json` files to be quickly recalled.

Reservoirs

The `phase_diagram` module provides the tools to analyse phase diagrams and organize the chemical potential data. The `PhaseDiagram` class in pymatgen plays a central role for the computation, the analysis and plotting of the PD data. The `PDHandler` class in the `phase_diagram.chempots` module contains functions which help to speed up the workflow. Once the desired reservoirs, with relative chemical potentials, are extracted, they can be organized and stored with the `Reservoirs` class, which behaves like a python dictionary and provides functions to quickly handle dictionaries of chemical potentials, and can be saved as `json` file. The link with oxygen partial pressure-dependent calculations is provided by the `phase_diagram.thermodynamics` module, which provides functions to create `Reservoirs` objects containing sets of chemical potentials for each oxygen partial pressure, which can then be used to compute Brouwer diagrams.

Defect Thermodynamics

The `defects.thermodynamics` module provides the tools to perform p_{O_2}-dependent analysis. Starting from a `DefectsAnalysis` object, an object of the `PressureAnalysis` class can be set up to solve the charge neutrality equation and extract electron chemical potential, conductivity and concentrations of

defects, as well as electrons and holes, for each p_{O_2} (`get_concentrations` function). The output data is organized through the `ThermoData` class, which can be stored as `json`. The data can be generated both in equilibrated and quenched/-doped conditions. The object can later be used as input for the `PressurePlotter` class in the `defects.plotter` module, which provides functions to create Brouwer diagrams and plot μ_e as a function of p_{O_2}.

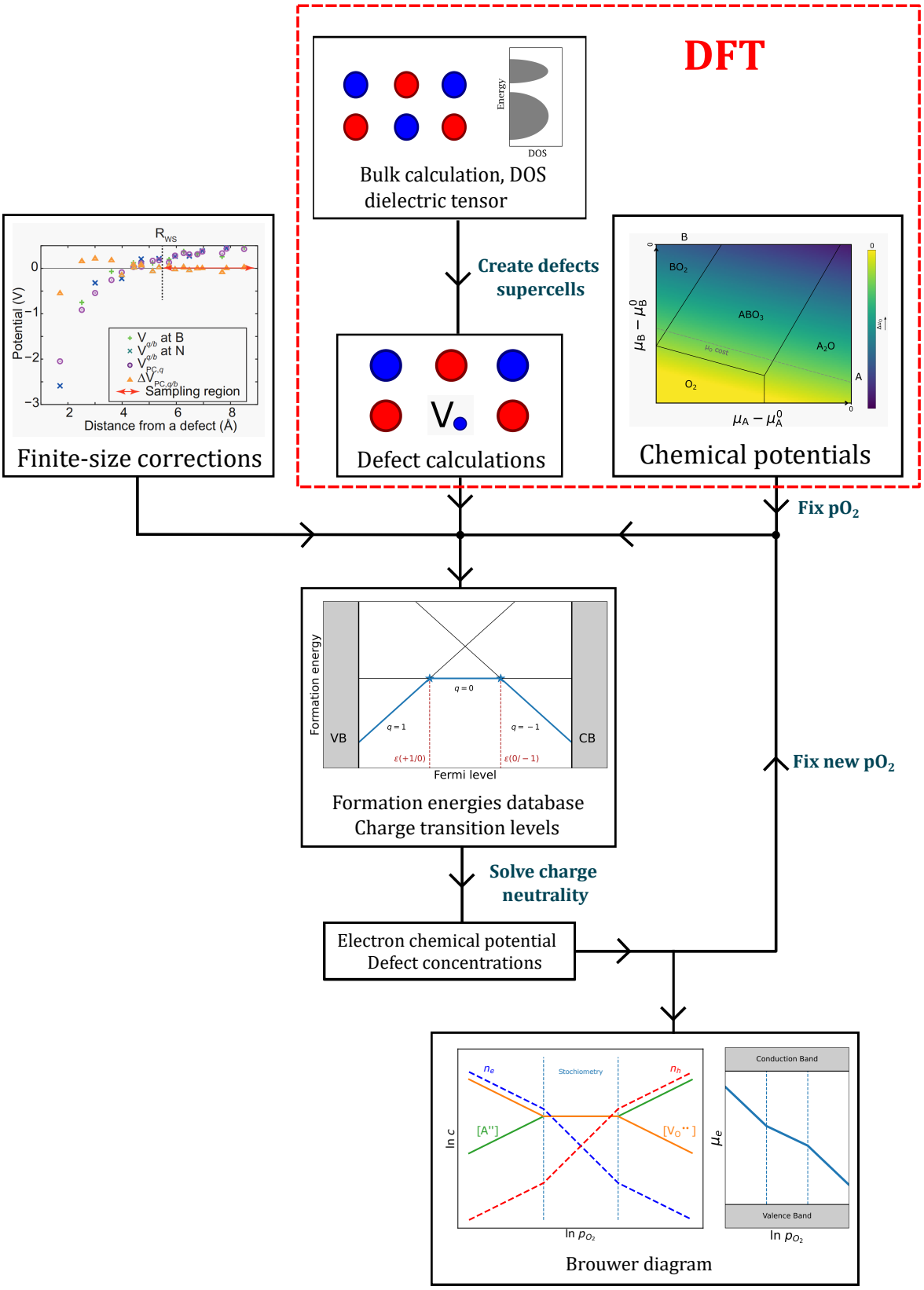

Figure 2.11: Workflow for basic *ab initio* defect thermodynamics calculations. In this work, we have developed the pynter library to systematically handle every step of this workflow.

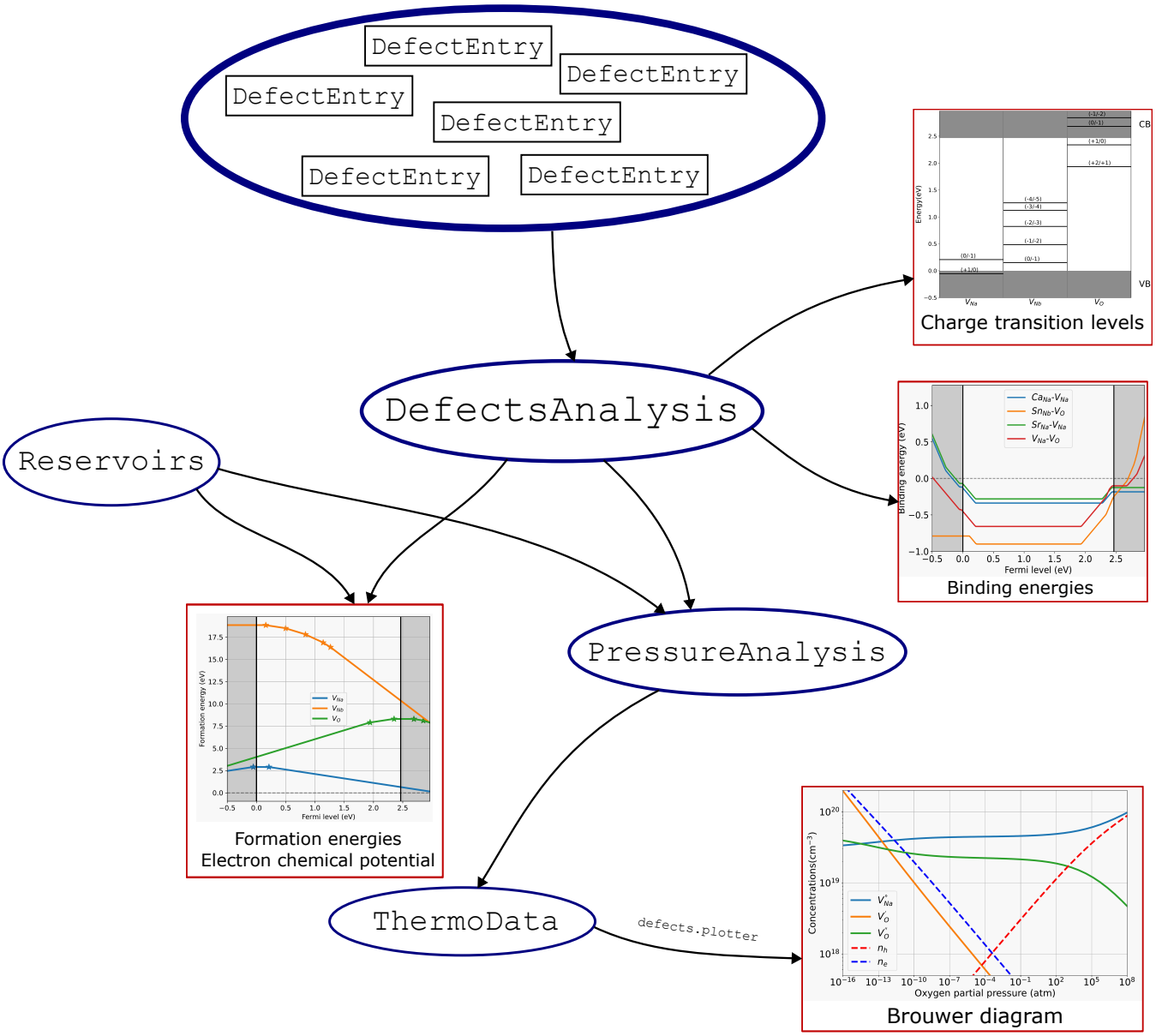

Figure 2.12: Workflow to analyse point defects with the pynter library. Defect entries are created from each DFT calculation, and organized in a database with the `DefectsAnalysis` class. Chemical potentials are stored with the `Reservoirs` class, and used to plot formation energies. The charge neutrality equation (both for equilibrated and quenched/doped conditions) is solved for different oxygen partial pressures. The output is stored with the `ThermoData` class and is used to generate Brouwer diagrams.

2.6 Conclusion

In summary, density functional theory allows to solve the quantum mechanical problem in a periodic crystal, by shifting the attention from the many-body wave function to the electron density, which permits to reformulate the many-body Schrödinger equation as a set of single-particle equations. With this approach, it is possible to compute the formation energies of charged point defects, and to solve the charge neutrality equation to calculate the position of the Fermi level at thermodynamic equilibrium. Using the connection between the chemical potential and the partial pressure of oxygen, it is possible to compute defect concentrations as a function of the oxygen partial pressure (Brouwer diagrams), which are useful to compare the computational results with the experiments. This methodology constitutes a major step forward with respect to the traditional approach to defect chemistry.[97] In fact, instead of relying on assumptions to solve the equilibrium constant of arbitrary chemical reactions, all the defect species in all charge states are considered simultaneously, including the dependency of their formation energies on the Fermi level. This allows to have a complete picture of the thermodynamics of defects, without the risk of neglecting important contributions that are not straightforward to predict. In this work, we have brought this approach one step further, by developing a novel scheme to account for quenching of defects, within the established point defect thermodynamics.

3 Sodium Niobate

The results presented in Section 3.1 are published in:

> [107] "L. Villa, E. Ghorbani, and K. Albe, *Role of intrinsic defects in cubic $NaNbO_3$: A computational study based on hybrid density-functional theory*, Journal of Applied Physics 131, 124106 (2022)."

while the results in Section 3.2 are published in:

> [108] "L. Villa and K. Albe, *Role of doping and defect quenching in antiferroelectric $NaNbO_3$ from first principles*, Physical Review B 106, 134101 (2022), Publisher: American Physical Society."

$NaNbO_3$ is one of the best candidates for lead-free antiferroelectric materials for applications in energy storage, due to the possibility of obtaining douple *P-E* loops at room temperature (see Chapter 1). In order to understand the role of doping on its antiferroelectric properties, we have studied the influence of intrinsic and extrinsic defects. This will provide insight on which defect species most likely form, the main compensation mechanisms, the influence of oxygen partial pressure on defect concentrations and electron chemical potential. Since $NaNbO_3$ is sintered at high temperature, upon cooling it undergoes many phase transitions. The equilibrium defect distribution at room temperature will be therefore a combination of thermodynamic and kinetic effects, where the contribution of kinetics gets particularly decisive if the mobility of the defects is low. We have therefore chosen to study defects in three phases of interest: the high temperature cubic phase (space group $Pm\bar{3}m$), the low temperature trigonal phase (*R3c*) and the room temperature orthorhombic phase (*Pbcm*), with additional focus on the latter. The goal is therefore to compare the defect formation energies in the three different phases, to evaluate the influence of the crystal structure (the phase) on the final defect distribution.

3.1 Cubic Phase

3.1.1 Computational Details

All calculations were performed based on density functional theory (DFT) using the Vienna *ab-initio* simulation package (VASP).[103–106] The electronic wave functions were described using the projector augmented-wave method,[53,109] which includes both valence and core states. To study pure $NaNbO_3$, the exchange-correlation effects were treated using the Perdew-Burke-Ernzerhof (PBE)[56] formalism of the generalized-gradient approximation (GGA), the Dudarev version[110,111] of GGA+U with a Hubbard correction term of 6 eV on Nb d-states, and the HSE06 hybrid functional,[62,112] with standard mixing and screening parameters of 25% and 0.2 $Å^{-1}$, respectively. All defect calculations were performed using a $3\times3\times3$ supercell, containing 135 atoms. The plane wave basis set was expanded up to a 500 eV cutoff energy. The Brillouin zone integration was performed using a Γ-centered $6\times6\times6$ k-mesh for unit-cell calculations and a $2\times2\times2$ k-mesh for supercell calculations. The atomic positions were relaxed until the Hellmann-Feynman forces on each atom were below 0.05 eV/Å. Without temperature contributions, the high temperature phases will be unstable with respect to the structure stable at 0 K. Therefore, in the absence of symmetry constraints, the high temperature phases would relax to the 0 K structure. For these reasons, when we compute the high temperature phases, we constrain the symmetry to that of the input structure space group, as implemented by VASP. We expand on this topic in Section 3.5. The lattice constant was determined by calculating the total energy at different cell volumes and fitting the data to the Birch-Murnaghan equation of state.[113,114] The density of states (DOS) were calculated using a Γ-centered $16\times16\times16$ k-mesh.

3.1.2 Lattice Constant and Electronic Structure

As previously outlined in Section 2.5, the first step is the study of bulk properties. The first dilemma we must face is the choice of the exchange-correlation (XC) functional, which we have seen plays a very important role in the determination of many properties we are interested in (Section 2.2.3). One of the most common choices is the PBE functional. This approach tends to yield slightly overestimated lattice parameters, to over-delocalize the charge with respect to the real behavior, and to severely underestimate the band gap (usually by almost a factor of 1/2). One method to correct for the two latter shortcomings is called DFT+U,[110,115] which includes a correction term to account for the self-interaction error, and

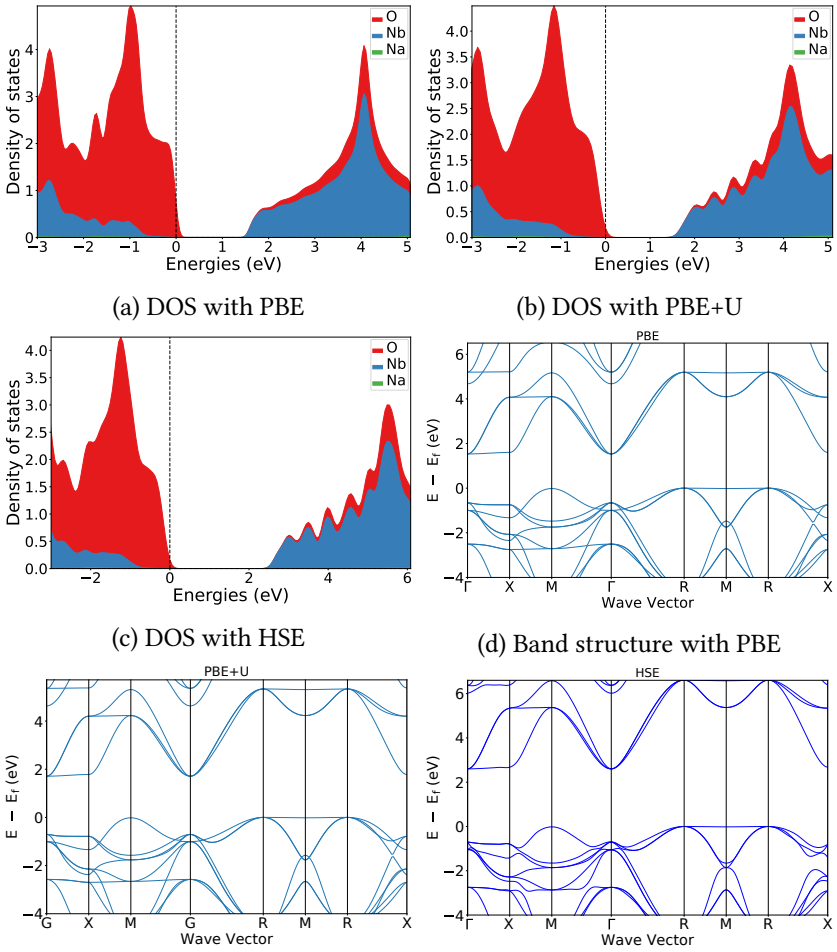

(a) DOS with PBE

(b) DOS with PBE+U

(c) DOS with HSE

(d) Band structure with PBE

(e) Band structure with PBE+U

(f) Band structure with HSE

Figure 3.1: Density of states and band structure of cubic NN with different XC-functionals.

is usually applied where the electrons are more strongly correlated, like d and f orbitals. While this method improves the description of the band gap, many properties depend on the magnitude of the correction (Hubbard parameter or U parameter). This constitutes a problem, as a universal criterion for the choice of the U parameter is to this day still missing. Hybrid functionals methods constitute a great improvement with respect to the previously mentioned approaches. They are, however, computationally at least two orders of magnitude more expensive than PBE or PBE+U, which constitutes a problem in case of defect calculations, where many calculations involving supercells are needed.

	a(Å)	$E_g^{ind}(eV)$
PBE	4.008	1.601
PBE+U	4.052	1.954
HSE06	3.967	2.927
Ref PBE [18]	3.975	1.652
Ref PBE0 [18]	3.931	3.756
MP Database (PBE) [116,117]	4.009	1.531
Exp	[21] 3.960	[118] 3.290

Table 3.1: Values of lattice constant a (Å) and energy gap E_g (eV) of cubic NN, calculated with different exchange-correlation functionals and confronted with computational data by D.Fritsch,[18] the Materials Project database [116,117] and experimental data.

In order to assess the performance of the aforementioned functional, we have run preliminary calculations for all of them. In particular, we have determined the lattice constant by fitting the dependency of the total energy on the cell volume to the Birch-Murnaghan equation of state.[113,114] Moreover, we have run density of states (DOS) and band structure (BS) calculations to accurately determine the electronic structure, with particular focus on the band gap. The results are reported in Table 3.1, Figure 3.1, and compared with other values reported in the literature. As expected, the computationally more expensive HSE06 functional is the better performing. Moreover, PBE overestimates the lattice parameter, while the band gap is severely underestimated. These results are not considerably improved with the introduction of the Hubbard correction, even though the band gap is closer to the experimental value. As it can be seen from Table 3.1, the hybrid functional can reproduce much more accurately the experimental data. The lattice parameter is almost exactly reproduced, and the indirect energy gap is also much closer to the experiment. Excluding the energy gap, the DOS and band structure are not heavily influenced by the choice of the functional. In the case of the PBE functional, the states are more delocalized with respect to the PBE+U and HSE06 functionals, as expected given its semi-local nature. The main contribution to the top of the valence band (VB) is given by the oxygen *p* orbitals, while the main contribution to the bottom of the conduction band (CB) is mainly associated with the niobium *d* orbitals.
As first step in the analysis of defect equilibrium in $NaNbO_3$, we will examine

the formation energies of the vacancies, only. Consequently, we can afford to employ hybrid functionals. In the next steps, when a much larger number of defects (including extrinsic defects and complexes) is involved, given the high number of calculations necessary, employing solely PBE will be necessary.

3.1.3 Chemical Potentials

The next step in the calculation of defect properties is to define the thermodynamic reservoirs. This requires the calculation of the semi–grandcanonical phase diagram, which shows the stability areas as function of the chemical potentials of the constituents (Section 2.4.5). We have computed the phase diagram starting from the stable phases reported in the Materials Project database.[116,117] The list of computed phases with relative formation energies is reported in Table 3.2. In order to evaluate the range of stability of cubic $NaNbO_3$, which is the phase of interest for defect properties, we have replaced the trigonal low-temperature phase with the high-temperature cubic phase. For the total energy calculations, both the atomic positions and the cell volume were fully relaxed. All calculations were performed with the HSE06 hybrid functional.
The defect formation energies were computed for different thermodynamic reservoirs, represented in Figure 3.2 by the labels from A to E and X1, X2, X3. Regions from A to E are generic limits of stability, which space from O-rich conditions (point C) to Na-rich and Nb-rich conditions (point A). It is also of interest to evaluate the formation energies using thermodynamic reservoirs that represent the experimental conditions. In particular, we fix the oxygen chemical potential ($\Delta\mu_O$) to its value at the conditions of temperature and partial pressure that can be found experimentally[17] (T = 950K, p_{O_2} = 0.2 atm). To calculate it we refer to Eq. 2.35, described in Section 2.4.5. With this procedure, we obtain $\Delta\mu_O$ = -1.09 eV. The points X1, X2 and X3 in Figure 3.2 are the regions where the oxygen chemical potential is constant and equal to -1.09 eV, in which the conditions go from Na-poor and Nb-rich (X1) to Na-rich and Nb-poor (X3). The chemical potential values associated to the labeled regions in the stability diagram are reported in Table 3.3.

3.1.4 Relaxation Volumes

In order to compute the total energies of the defective systems, the atomic positions in all the supercell structures have been optimized (Section 3.1.1). Since the cubic phase is stable at high temperature, its structure will be unstable at a DFT

Phase	Structure	Formation energy (eV/atom)
$NaNbO_3$	Cubic ($Pm\bar{3}m$)	-2.73
NaO_2	Orthorhombic (Pnnm)	-0.98
Nb	Cubic ($Im\bar{3}m$)	0.0
NbO_2	Tetragonal ($I4_1$)	-2.83
Na	Cubic ($P4_132$)	0.0
$Na_2Nb_3O_6$	Trigonal ($P\bar{3}1c$)	-2.61
Na_2O	Cubic ($Fm\bar{3}m$)	-1.41
Na_8NbO_6	Triclinic (P1)	-1.80
Na_7NbO_6	Triclinic (P1)	-1.95
Nb_2O_5	Monoclinic (C2/m)	-2.92
Na_2O_2	Hexagonal ($P\bar{6}2m$)	-1.35
O_2	Monoclinic (C2/m)	0.0
$Na_8Nb_5O_{14}$	Triclinic ($P\bar{1}$)	-2.45
$NaNb_{10}O_{18}$	Monoclinic ($P2_1/c$)	-2.71

Table 3.2: Formation energy per atom for all the compounds used to compute the stability diagram.

Reservoir	$\Delta\mu_{Na}$ (eV)	$\Delta\mu_{Nb}$ (eV)	$\Delta\mu_{O}$ (eV)
A	-0.5	-2.52	-3.54
B	-1.69	-1.56	-3.47
C	-3.43	-10.22	0
D	-1.85	-9.25	-0.85
E	-1.8	-6	-1.95
X1	-2.89	-7.55	-1.09
X2	-2.32	-8.13	-1.09
X3	-1.74	-8.7	-1.09

Table 3.3: Values of the chemical potentials of Na, Nb and O for each of the labelled regions in the stability diagram (Figure 3.2).

level (0 K), and only symmetry constraints within the calculations prevent it from relaxing to the low temperature phase. It is therefore interesting to investigate the relaxation mechanisms once we introduce a big perturbation to the lattice, such as point defects and even a complex of defects. The local environment of neutral single vacancies in the relaxed structures is shown in Figure 3.3a, as represented by the software OVITO.[119] By analysing the bond lengths and the

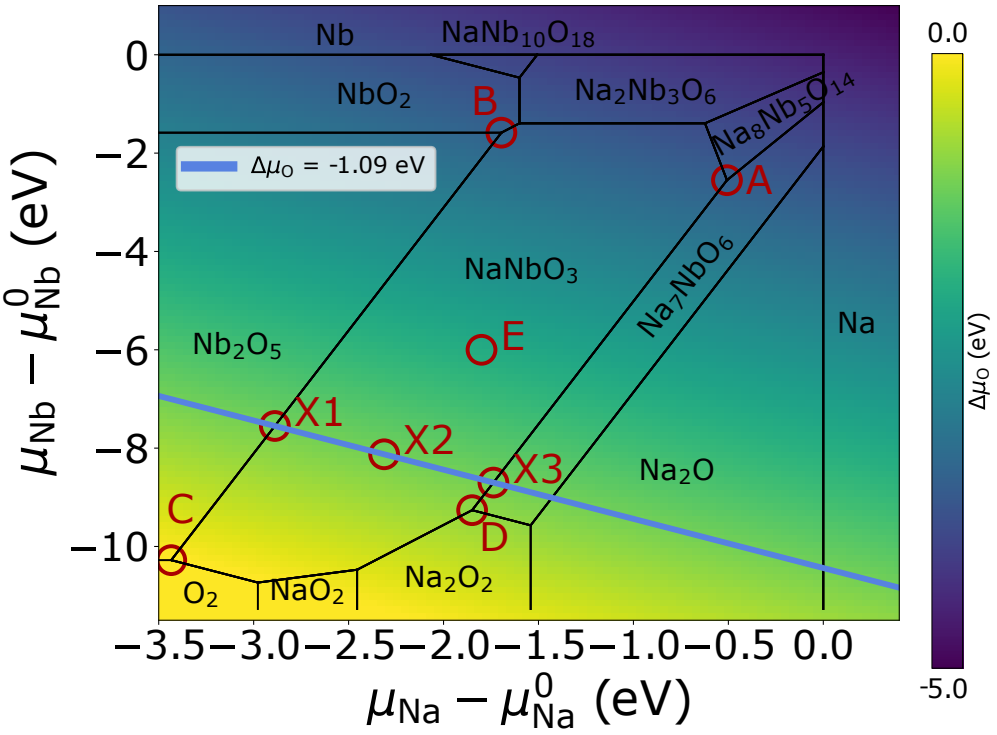

Figure 3.2: Stability diagram of the ternary Na-Nb-O system, as derived from the data in Table 3.2. The defect formation energies are discussed in terms of the chemical potentials at the points from A to E and from X1 to X3, reported in Table 3.3.

atomic displacements (with respect to the bulk structure), it can be concluded that the three defect species have different effects on the local environment. In fact, in the presence of the oxygen vacancy, the structure is stabilized via tilting of the oxygen octahedra in the vicinity of the defect, shown by the large displacements of the neighbouring oxygen atoms. As a matter of fact, all the lower temperature phases of $NaNbO_3$ display O-octahedra tilting. Additionally, the O-octahedra are distorted, which is highlighted by both the atomic displacements and the deformation of the Nb-O bond lengths. The sodium vacancy does not induce any significant rearrangement of the lattice. The neighbouring oxygen atoms deviate towards the other Na atoms, but the Nb-O bond length deviates only slightly from the bulk value. The effect on the local structure is certainly different in the case of niobium vacancies, where the Na atoms rearrange by shrinking towards the Nb vacancy. The neighbouring Na-O bonds decrease significantly

	P_{11} (eV)	P_{22} (eV)	P_{33} (eV)	P_{12} (eV)	P_{13} (eV)	P_{23} (eV)	ΔV (Å^3)
V_{Na}	2.37	2.37	2.37	-0.00	-0.00	0.00	1.9
V_{Nb}	-21.11	-21.11	-21.11	-0.00	0.00	-0.00	-16.7
V_O	12.80	12.80	-8.90	-0.49	-1.75	-1.75	4.4
$2V_{Na}$ - V_O (np)	0.25	0.25	17.27	-0.85	-0.00	-0.00	4.7
$2V_{Na}$ - V_O (p)	-31.69	28.04	15.29	-0.00	-0.00	-0.00	3.1

Table 3.4: Elastic dipole tensor and relaxation volumes in the neutral case of single vacancies and the defect complex formed by two sodium vacancies and one oxygen vacancy in the non-polar (np) and polar (p) configurations.

(up to -17%), as highlighted by the additional bonds in the figure.
In addition to single vacancies, we have studied the defect complex formed by two Na vacancies and one O vacancy in two different configurations (named polar and non-polar), whose schematic representations are shown in Figure 3.3b. In the polar configuration the two Na vacancies are non-centrosymmetric with respect to the O vacancy, while the alternative centrosymmetric case gives the non-polar configuration. Figure 3.3c shows the local structure around the complex after relaxation. In both cases, the presence of the defect complex introduces tilting of the oxygen octahedra, like in the case of O vacancy. In the polar case, the O-octahedra undergo greater distortions than the non-polar case, which can be seen by the greater displacements of the adjacent O-atoms and large changes in the Nb-O bond lengths.
In order to extend this analysis to quantitative data, we have evaluated the effects of the computed vacancies in the neutral case on the elastic dipole tensor and on the cell volume, as outlined in Section 2.4.6. To perform this analysis, the atomic positions were further relaxed until the Hellmann-Feynman forces on each atom were below 0.001 eV/Å in the cases of single vacancies and 0.005 eV/Å for the defect complexes. A bulk modulus of $202.5\mathrm{GPa}$ has been obtained by calculating the total energy at different cell volumes and fitting the data to the Birch-Murnaghan equation of state (Section 3.1.1). The computed components of the symmetric elastic dipole tensor and relaxation volumes (ΔV) for the different defect species are reported in Table 3.4.
The value of ΔV is positive for all defect species except for Nb vacancies, which shows that the defects are overall a positive dilatation center. This might seem counter-intuitive for vacancies (where one would expect a shrinking of the lattice) but in this case it is to be attributed to the local structural rearrangement (especially in the case of O-octahedra tilting). It is also important to remember

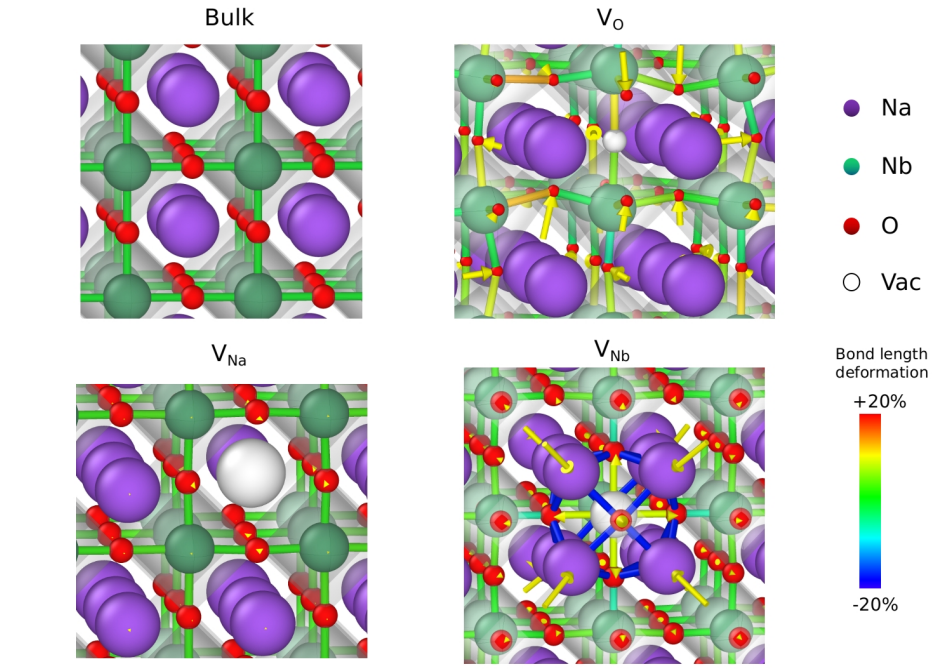

(a)

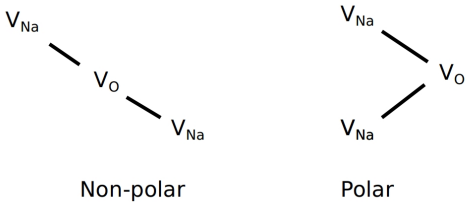

(b)

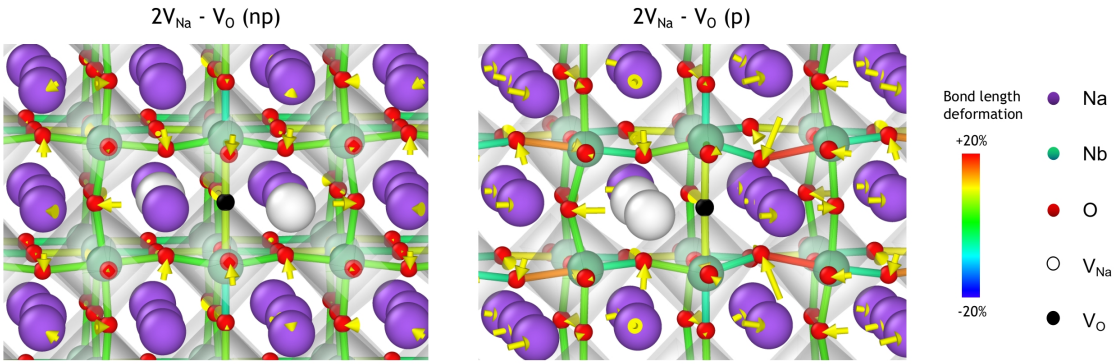

(c)

Figure 3.3: **a)** Local structures after relaxation around single vacancies. **b)** Vacancy sites chosen for the defect complex were formed by two Na vacancies and one O vacancy. The non-polar configuration is given when the two Na sites are centrosymmetric with respect to the O site. In the polar configuration, however, the two Na vacancies are non-centrosymmetric with respect to the O site. **c)** Local structure around the vacancy complex in the two configurations after relaxation.

that the cubic phase of $NaNbO_3$ is not the stable phase at 0 K, which means that O-octahedra tilting reduces the total energy of the structure. The only situation where we find negative values of ΔV is for Nb vacancies. This is easily explained by looking at Figure 3.3a. In fact, it can be seen that the missing Nb atom produces a shrinkage of Na atoms towards the empty atomic site, which results in a tensile stress on the supercell, hence a negative value of the relaxation volume.

3.1.5 Defect Formation Energies

As mentioned previously in Section 3.1.2, we have studied Na, Nb and O vacancies. In addition to the formation energies of single vacancies, we have also computed the formation energy of the defect complex formed by one oxygen vacancy and two neighboring sodium vacancies, in three different charge states (-1, 0, +1) and two possible configurations, as displayed in Figure 3.3b.
The calculated formation energies of the intrinsic point defects in the different thermodynamic conditions from A to E (reported in Table 3.3) are plotted as a function of the Fermi level in Figure 3.6, as we have described in Section 2.4.3. As most commonly adopted in the literature, we have chosen to plot the formation energies treating the Fermi level as a free parameter. We have chosen to name it as "Fermi level" instead of "μ_e" in the plots in order to distinguish it from the self-consistently calculated electron chemical potential, which is not a free parameter, but is determined by the charge neutrality condition (Eq. 2.50). This quantity is displayed in the plots by the black vertical dashed line. The charge transition level (CTL)s for all defects are displayed in Figure 3.4. The formation energy of Nb vacancy is found to be the largest amongst all defect types in all five thermodynamic reservoirs, even in the Nb-poor ones (C and D). The CTLs associated with Nb vacancy are spread across the whole band gap. As expected, the Nb vacancy is an acceptor-type defect. Oxygen vacancies have much lower formation energies. In O-poor conditions (A and B), they are the most stable defect across all the band gap. The most stable charge state is +2 across most part of the band gap, resulting in a donor-type defect, which confirmed expectations. There are two close charge transitions, (+2/+1) and (+1/0), which are placed at 0.85 eV and 0.25 eV below the conduction band minimum (CBM), respectively. The (0/-1) CTL is located within the CB states. In their study of photocatalytic activity of bulk and reduced $NaNbO_3$, Yang *et al*[120] reported that the oxygen CTL is at circa 1 eV below the CBM, which is in reasonable agreement with our findings. It should be noted that, although in their work $NaNbO_3$ is in its room-temperature phase, the distance between the O CTL and the CBM is comparable to the cubic phase

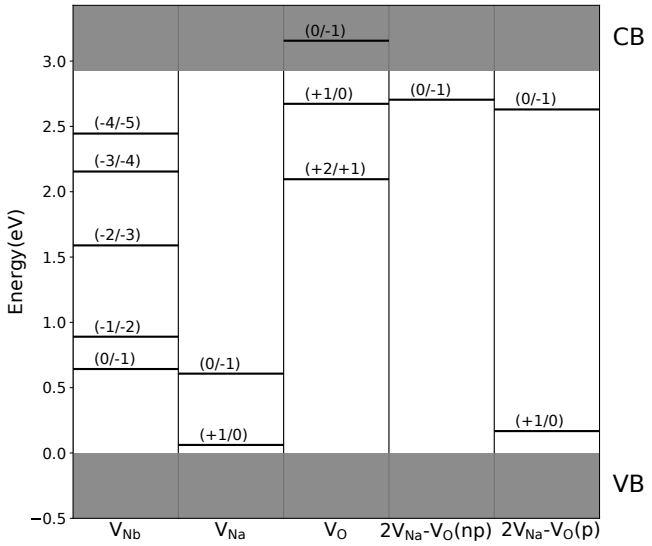

Figure 3.4: Charge transition levels for single vacancies and the vacancy complex $2V_{Na} - V_O$ in its two configurations. The energy levels in the VB and the CB are indicated by the gray shaded areas.

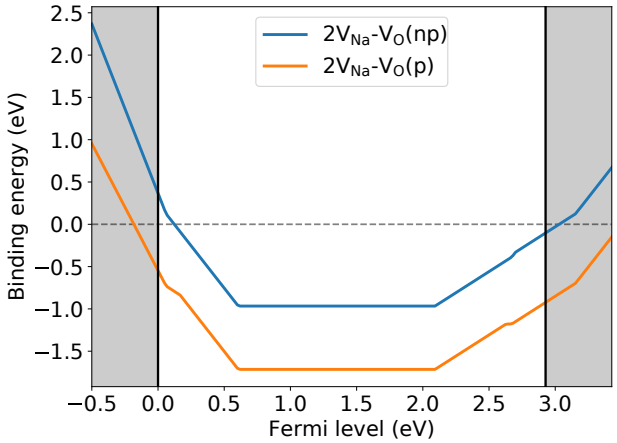

Figure 3.5: Binding energy for the two configurations of the $2V_{Na} - V_O$ vacancy complex as a function of the Fermi level. The kinks correspond to charge transition points of the isolated defects.

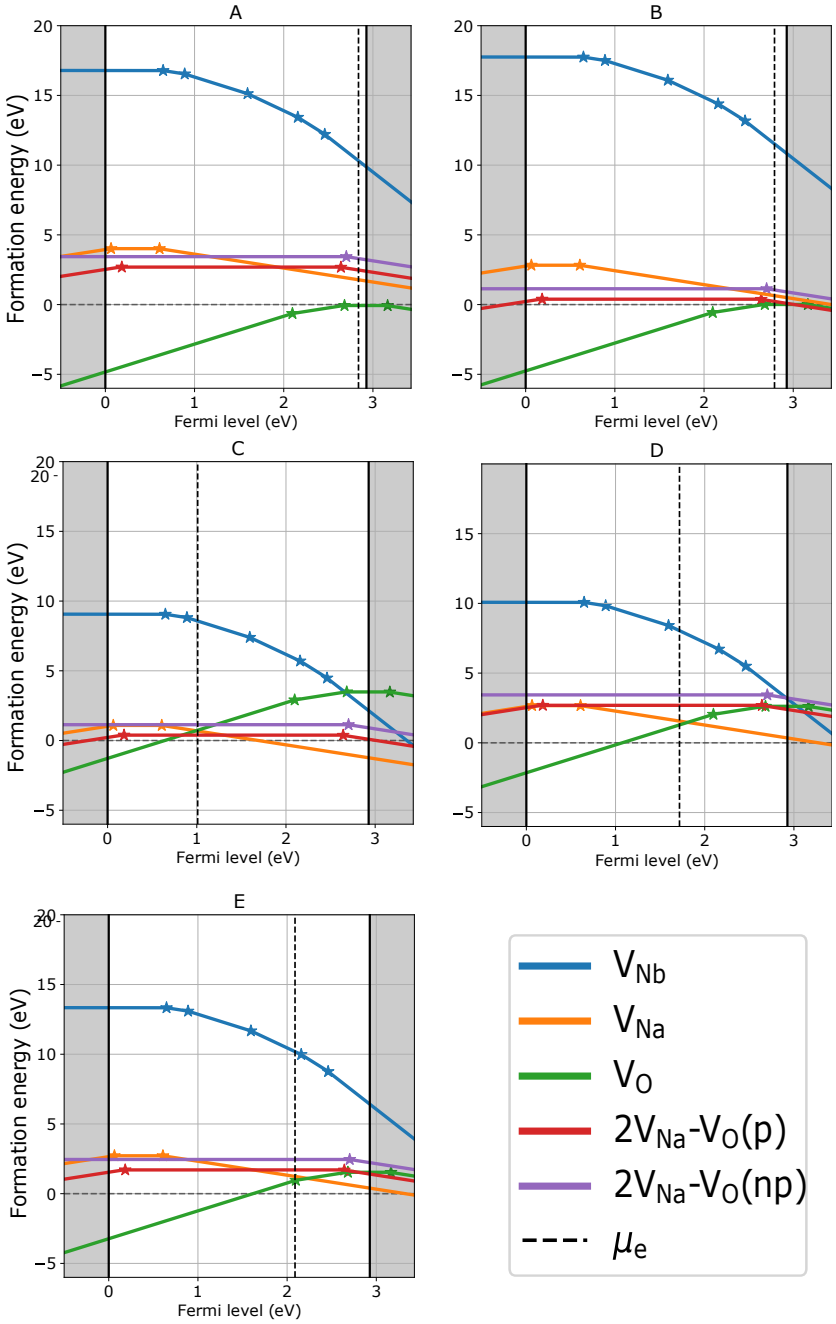

Figure 3.6: Defect formation energies in cubic NN as a function of the Fermi level position for representative thermodynamic conditions A, B, C, D, E (shown in Figure 3.2). The stars on the formation energy curves represent charge transitions. The calculated position of the electron chemical potential μ_e at 950 K is displayed by the dashed vertical line.

studied in current work. In fact, in both cases (room-temperature orthorhombic phase and high-temperature cubic phase) the top of the VB is mainly constituted of O $2p$ states, while the bottom of the CB contains mainly Nb $4d$ states. Hence, the character of the band structure is preserved, and the relative distance of the O CTL with respect to the bottom of the CB can be safely compared in different phases. The formation energies of Na vacancies are much closer to the ones of oxygen than to that of Nb. In Na-poor conditions (C), Na vacancies are more stable than O vacancies across most part of the band gap. The CTL are close to the valence band maximum (VBM), with the -1 charge state being stable starting from 0.6 eV above the VBM, making Na vacancies an acceptor-type defect. The last computed defect is the defect complex formed by one O vacancy and two Na vacancies. The binding energy of a complex of vacancies is defined by the difference between its formation energy and the formation energies of the isolated vacancies. It is therefore independent of the chemical potentials. In this specific case, the binding energy is given by:

$$E_b = \Delta E^f_{2V_{Na}-V_O} - (2\Delta E^f_{V_{Na}} + \Delta E^f_{V_O}), \tag{3.1}$$

where $\Delta E^f_{2V_{Na}-V_O}$ is the formation energy of the complex, $\Delta E^f_{V_{Na}}$ and $\Delta E^f_{V_O}$ are the formation energies of isolated Na and O vacancies, respectively. Figure 3.5 shows the binding energy E_b of the defect complex, in the two configurations (as previously described) as a function of the Fermi level position. It is clear from the plot that the binding energy of the polar configuration is more negative than the non-polar one. In particular, there is an energy gain of 0.75 eV when the system goes from non-polar to polar configuration. The values of E_b are negative throughout the most part of the band gap, which means that the formation of the vacancy complexes are more probable with respect to isolated vacancies. The position of the Fermi level at which the binding energies are most negative is at approximately the middle of the gap. The associated charges of single Na and O vacancies in this region are -1 and +2, respectively. This means that in the presence of the defect complex, there will be a strong interaction between the charges of the vacancies, which reduces the overall energy of the system with respect to the isolated vacancies.

Additionally, we have computed the formation energies fixing the chemical potential of oxygen according to the experimental conditions during the synthesis. As described in Section 3.1.3, we have calculated $\Delta\mu_O$ at $T = 950$ K and $p_{O_2} = 0.2$ atm, which allowed us to define the thermodynamic reservoirs X1, X2, X3 in Table 3.3. The formation energies in these conditions are reported in Figure 3.7.

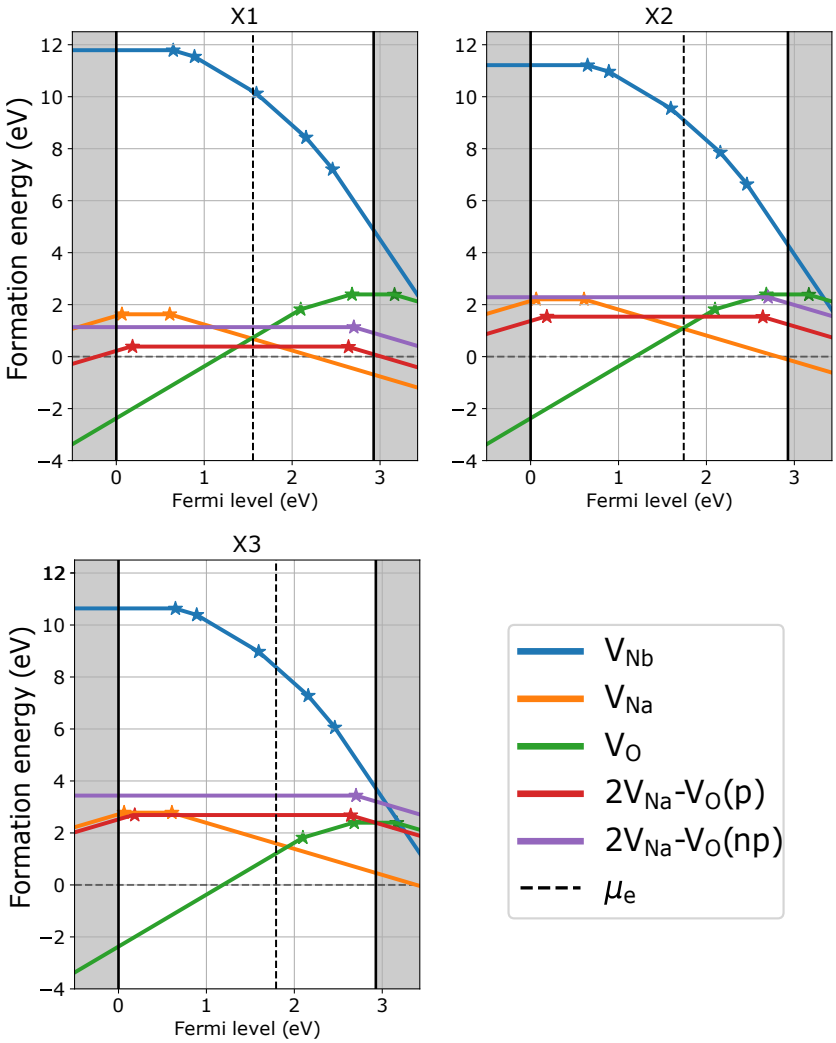

Figure 3.7: Defect formation energies in cubic NN as a function of the Fermi level position in the thermodynamic reservoirs with $\Delta\mu_O$ fixed to -1.09 eV (shown in Figure 3.2). The stars on the formation energy curves represent charge transitions. The calculated position of the electron chemical potential μ_e at 950 K is displayed by the dashed vertical line.

Niobium vacancies have the higher formation energies between all defect types as in the previous case. In all three reservoirs Na and O vacancies are the most stable defects throughout the band gap. The complexes of vacancies have comparable formation energies and have the smallest formation energy values in Na-poor conditions (X1).

Reservoir	μ_e (eV)
A	2.84
B	2.81
C	1.01
D	1.72
E	2.09
X1	1.55
X2	1.74
X3	1.79

Table 3.5: Position of the electron chemical potential dictated by the charge neutrality conditions in cubic NN, in all the thermodynamic reservoirs shown in Figure 3.2, computed with the method described in Section 2.4.5.

Electron Chemical Potential

We have determined the position of the electron chemical potential (μ_e), dictated by the charge neutrality condition, for all thermodynamic reservoirs listed in Table 3.3, with the method described in Section 2.4.5. We have chosen to compute μ_e at a temperature of 950 K, in order to evaluate the system's behaviour when it is close to the synthesis temperature. As already mentioned, this is most likely the condition where the most part of intrinsic defects are installed. The results are reported in Table 3.5 and displayed in Figure 3.7. For all reservoirs apart from C, the position of μ_e closer to the CBM suggests that the material is an n-type semiconductor. In reservoir C (Na-poor), we register an opposite behaviour with μ_e being closer to the VBM and the semiconductor being more p-type. This is due to the lower formation energies of Na vacancies in Na-poor conditions. In the case of the other three reservoirs with fixed $\Delta\mu_O$, the position of μ_e is closer to the middle of the gap. Going from Na-poor (X1) to Na-rich (X3) conditions, the electron chemical potential shifts in the direction of the CBM, indicating that the system behaves more as a donor.

Dependency on Oxygen Partial Pressure

As already mentioned in Section 2.4.5, experimentally the oxygen chemical potential can be controlled by varying the oxygen partial pressure. Therefore it is useful to calculate the defect concentrations and the electron chemical potential as a function of the partial pressure, in order to be able to relate computational

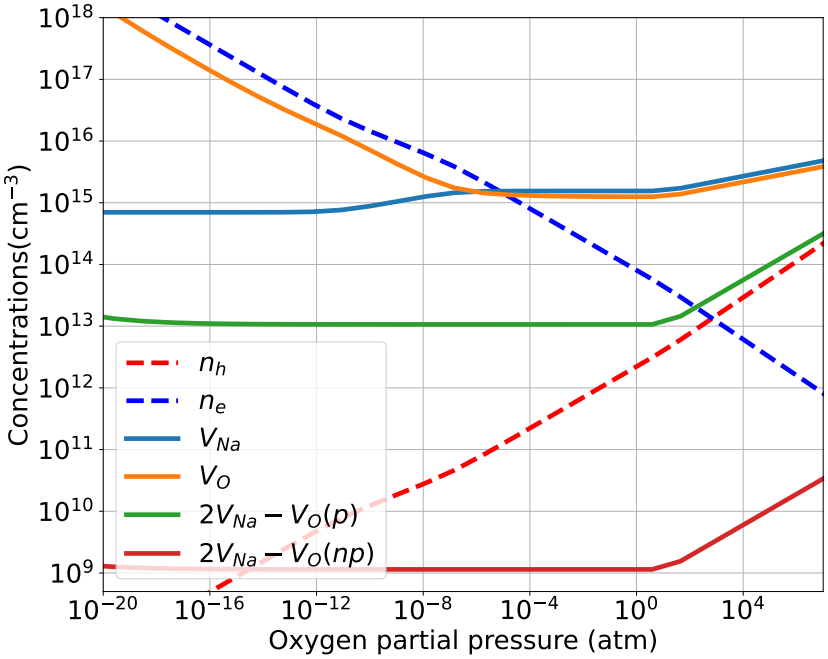

Figure 3.8: Concentrations of Na and O vacancies and vacancy complexes in cubic NN as a function of oxygen partial pressure at T = 950 K.

and experimental data. To this day, there is still not reported experimental data of defect concentrations in pure $NaNbO_3$.
We have converted the values of $\Delta\mu_O$ in oxygen partial pressures using Eq. 2.35, keeping the constraints of the stability over competing phases, which restricts the range of $\Delta\mu_O$. We have reported the values of the mostly relevant concentrations of Na and O vacancies as a function of partial pressure in Figure 3.8. For low values of oxygen partial pressure (p_{O_2}), the dominant defect is the O vacancy, mostly in the +2 charge state. As p_{O_2} increases, we move into more oxygen-rich conditions, where $\Delta\mu_O$ increases. This leads to a decrease in the concentration of V_O, while the concentrations of Na vacancies grows considerably to reach a condition where the concentrations of V_{Na} and V_O have the same order of magnitude. For high values of p_{O_2}, the behaviour of O vacancies changes, starting to increase again in concentration as partial pressure increases. This is due to the fact that, as the conditions get more oxygen-rich, the electron chemical potential

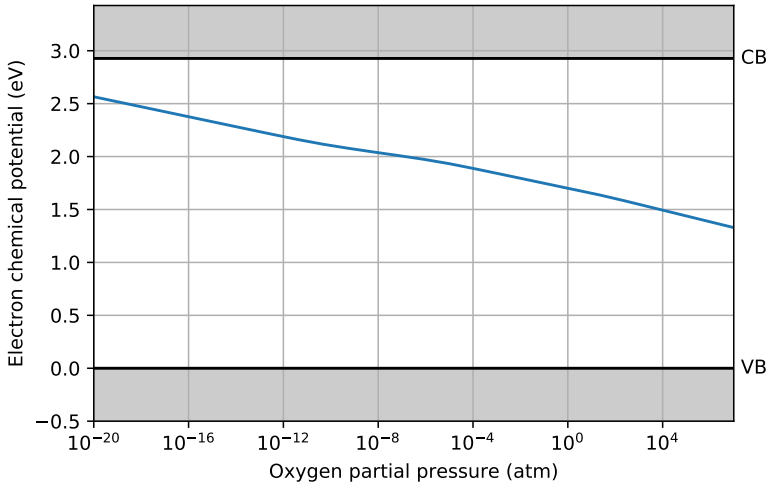

Figure 3.9: Electron chemical potential determined self-consistently as a function of the oxygen partial pressure at T = 950 K.

shifts in the direction of the VBM, in which the formation energies of V_O decrease. This behaviour of μ_e is shown in Figure 3.9. For low p_{O_2} values the system is an n-type semiconductor, with a value of μ_e less than 0.5 eV close to the CBM. As p_{O_2} increases, the electron chemical potential shifts to lower values, to reach the high p_{O_2} condition where it is approximately in the middle of the gap.

3.2 Orthorhombic Phase

The orthorhombic phase (space group *Pbcm*) is the main focus of our research on $NaNbO_3$, since it is stable at room temperature (from 173 K to 633 K). Therefore, in addition to vacancies, we studied the effect of extrinsic defects on the material. In particular, starting from the results reviewed in Section 1.5, we focused on the presence of Ca, Sr and Sn dopants, including the investigation on the presence of defect complexes.

3.2.1 Computational Details

The main details regarding the software used to carry out DFT calculations are consistent with the ones reported in Section 3.1.1. Since the crystal structure has changed, some parameters need to be adjusted. In particular, all defect calculations were performed using a $2\times2\times1$ supercell, containing 160 atoms. The plane wave basis set was expanded up to a 550 eV cutoff energy. The Brillouin zone integration was performed using a Γ-centered $4\times4\times2$ k-mesh for unit-cell calculations and a $2\times2\times2$ k-mesh for supercell calculations. The atomic positions were relaxed until the Hellmann-Feynman forces on each atom were below 0.05 eV/Å. The density of states (DOS) were calculated using a Γ-centered $12\times12\times6$ k-mesh. As far as the exchange-correlation functional is concerned, in light of the high number of calculations required to study the intrinsic and extrinsic defects, including defect complexes, to employ hybrid functionals would be too computationally expensive. Therefore, for these calculations, we employed the PBE-GGA[56] approach.

3.2.2 Electronic Structure

As we have already seen for the cubic phase (Section 3.1.2), the relaxed bulk structure and the electronic structure need to be determined. In fact, the total energy of the bulk supercell and the VBM are required for the evaluation of defect formation energies (Eq. 2.26), while the DOS is used in the computation of electrons and holes concentrations (Eq. 2.52 and Eq. 2.53). The computed values of lattice parameters and energy gap are reported and compared with literature in Table 3.6.
The edge of the valence band is mainly given by O p states, while the edge of the conduction band is mainly composed of Nb d states. The VBM is in the S point, with the Γ-point being very close in energy, and the CBM is in the Γ-point, yielding an indirect gap of 2.48 eV. It is well known that the semi-local nature of the PBE functional tends to underestimate the band gap. However, it does not constitute a big problem for defect equilibrium calculations, because the biggest contributions in the defect equilibrium are given by the curvature of the bands near the band edges, and by the relative distance of the thermodynamic charge transition levels to the band edges.

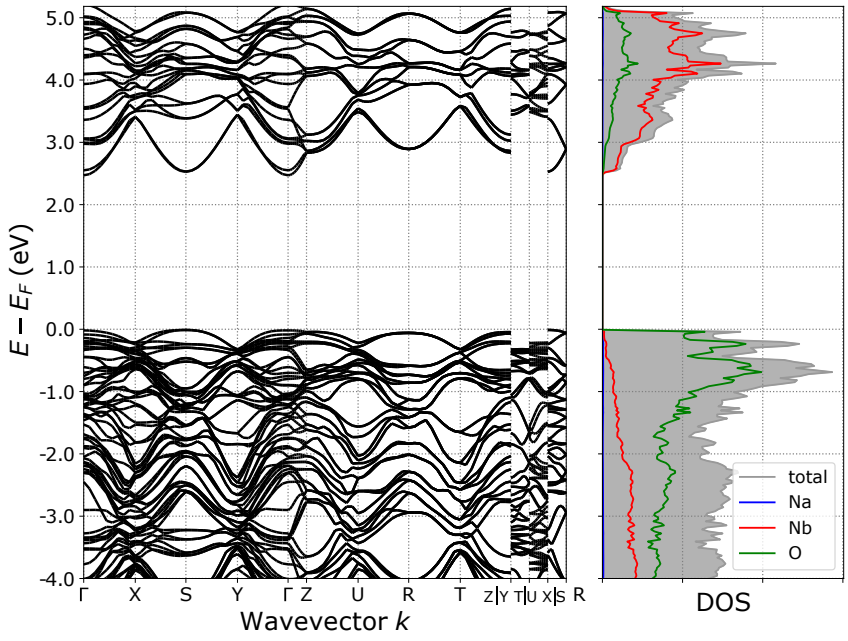

Figure 3.10: Band structure and density of states of orthorhombic $NaNbO_3$ (space group *Pbcm*).

	a(Å)	b(Å)	c(Å)	$E_g(eV)$
PBE	5.569	5.677	15.571	2.48
Ref PBE [121]	5.560	5.629	15.552	2.34
MP Database (PBE) [116,117]	5.598	5.687	15.681	2.36
Exp	5.532 [17]	5.563 [17]	15.645 [17]	3.42 [118]

Table 3.6: Values of lattice constants a, b, c (Å) and energy gap E_g (eV) of orthorhombic $NaNbO_3$ (space group *Pbcm*, No. 57), computed with the PBE [56] exchange-correlation functional and confronted with computational data by Shigemi and Wada [121], the Materials Project database [116,117] and experimental data.

Composition	Structure	Formation energy (eV/atom)
$Nb_{12}O_{29}$	Orthorhombic (Cmcm)	-3.05
NaO_2	Orthorhombic (Pnnm)	-0.91
Nb_2O_5	Monoclinic (P2)	-3.05
Na_2O_2	Hexagonal ($P\bar{6}2m$)	-1.31
$NaNb_{10}O_{18}$	Monoclinic ($P2_1/c$)	-2.79
Na_2O	Cubic ($Fm\bar{3}m$)	-1.45
Nb	Cubic ($Im\bar{3}m$)	0
NbO_2	Tetragonal ($I4_1/a$)	-2.91
$NaNb_{13}O_{33}$	Triclinic (P1)	-3.03
$NaNb_3O_8$	Orthorhombic (Pmmn)	-2.97
Na	Hexagonal ($P6_3/mmc$)	0
$Na_2Nb_3O_6$	Trigonal ($P\bar{3}1c$)	-2.67
O_2	Monoclinic (C2/m)	0
$NaNbO_2$	Hexagonal ($P6_3/mmc$)	-2.54
Na_5NbO_5	Monoclinic (C2/c)	-2.25
NbO	Cubic ($Pm\bar{3}m$)	-2.29
$NaNbO_3$	Orthorhombic (Pbcm)	-2.83
Na_3NbO_4	Monoclinic (C2/m)	-2.52

Table 3.7: Formation energy per atom for all the compounds used to compute the stability diagram.

3.2.3 Chemical Potentials

The chemical potentials were calculated from the data reported in the Materials Project database,[116,117] whose set of parameters is consistent with the ones we have used in this work. The phase stability diagram was constructed for the orthorhombic phase of $NaNbO_3$, using the python materials genomics (Pymatgen) library.[102,122] The stability diagram is reported in Figure 3.11, and the stable phases in Table 3.7. The defect formation energies were computed for different thermodynamic reservoirs, represented in the figure by the labels from A to D and X. Regions from A to D are generic limits of stability, which space from O-rich conditions (point C) to Na-rich and Nb-rich conditions (point B). It is also of interest to evaluate the formation energies using a thermodynamic reservoir that represents the experimental conditions. In particular, we fix the oxygen chemical potential ($\Delta\mu_O$) to its value at the conditions of temperature and partial pressure of the sintering process, according to the work of Zhang *et al*[23] (T =

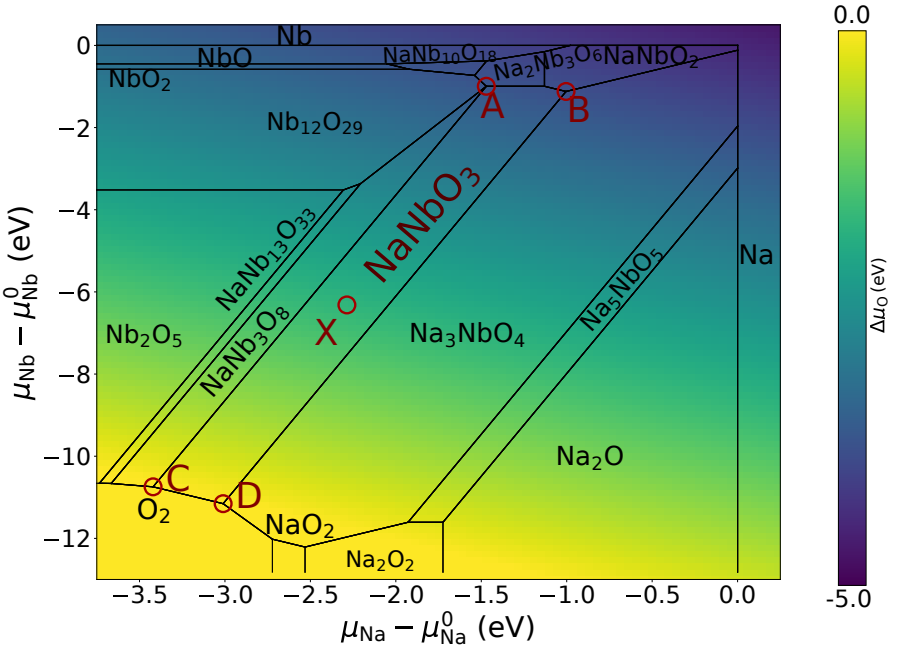

Figure 3.11: Stability diagram of the ternary Na-Nb-O system, as derived from the data in Table 3.7. The defect formation energies are discussed in terms of the chemical potentials at the points from A to D and point X, as reported in Table 3.8.

1633 K, p_{O_2} = 0.2 atm). For details on the calculation of this quantity we refer to Eq. 2.35, described in Section 2.4.5. With this procedure we obtain $\Delta\mu_O$ = -1.92 eV, which is indicated by the point X in Figure 3.11. In order to obtain the chemical potential of the extrinsic elements (Ca, Sr and Sn), we have generated the stability diagrams for $CaSnO_3$ and $SrSnO_3$ in the same fashion as for $NaNbO_3$. The reference elemental phases of Sr, Ca and Sn are trigonal ($R\bar{3}m$), hexagonal ($P6_3/mmc$) and cubic ($Fd\bar{3}m$), respectively. Since the range of stability varies for every compound, we have evaluated the chemical potential of the elements in O-poor and O-rich regions, assigning the former to reservoirs A and B and the latter to reservoirs C and D.
In region X, the values are taken from the center of the stability region, having fixed $\Delta\mu_O$ to -1.92 eV. This procedure is carried out mainly to be able to compare the formation energies of the extrinsic defects with the intrinsic ones. However, when we solve the charge neutrality, extrinsic defects in $NaNbO_3$ are not free to exchange particles with a reservoir, as their concentrations are fixed to the

Reservoir	$\Delta\mu_O$	$\Delta\mu_{Nb}$	$\Delta\mu_{Na}$	$\Delta\mu_{Sr}$	$\Delta\mu_{Ca}$	$\Delta\mu_{Sn}$
A	-3.94	-0.90	-1.49	-3.50	-4	0
B	-4.06	-1.08	-0.96	-3.50	-4	0
C	0	-10.72	-3.49	-6.50	-7	-6
D	0	-11.22	-2.99	-6.50	-7	-6
X	-1.92	-6.15	-2.26	-5.79	-5.92	-4.19

Table 3.8: Values in eV of the chemical potentials of the individual elements for each of the labelled regions in the stability diagram (Figure 3.11).

experimental values. The chemical potential values associated to the labeled regions in the stability diagram are reported in Table 3.8.

3.2.4 Relaxation Volumes

Just as we have already seen for the cubic phase in Section 3.1.4, it is interesting to evaluate how the lattice reacts to the formation of a defect. We have applied the methodology described in Section 2.4.6 and Section 3.1.4 for neutral defects. The relaxation volumes and elastic dipole tensor for both single defects and defect complexes are reported in Table 3.9. As opposed to the cubic case, all relaxation volumes are negative, meaning that all defects are overall negative dilatation centers. The relaxation volume is particularly negative for the case of Nb vacancies, where the missing atom at the center of the octahedron produces a shrinkage of the atoms on the vertices, just like in the cubic phase (Figure 3.3c). For the other defects, however, the relaxation mechanism of octahedra tilting is no longer available, since the RT stable orthorhombic phase already displays tilted octahedra. This means that the structural relaxation present in the cubic phase is no longer happening, where in this case the defect is a negative relaxation center. It is also interesting to notice that the relaxation volume is negative also in case of substitutional defects, also in the cases where the substituting atom has a greater radius.

3.2.5 Defect Formation Energies

In this study, we have computed defect formation energies according to Eq. 2.26, in the different regions of the stability diagram reported in Figure 3.11 and Table 3.8. Because of the finite size of the supercell, we have corrected the unphysical

	$P_{11}(eV)$	$P_{22}(eV)$	$P_{33}(eV)$	$P_{12}(eV)$	$P_{13}(eV)$	$P_{23}(eV)$	$\Delta V(\text{Å}^3)$
Ca_{Na}	0.30	3.43	-9.91	-0.00	-0.00	0.54	-2.01
V_{Na}	-0.31	0.01	-4.98	-0.00	-0.00	0.35	-1.72
V_{Nb}	-9.01	-8.54	-19.52	-0.52	-0.69	-0.06	-12.06
V_O	-0.59	4.62	-11.24	3.62	0.33	-0.16	-2.34
Sn_{Nb}	-1.54	0.17	-9.45	0.03	0.05	0.02	-3.52
Sr_{Na}	-3.85	-0.18	-14.32	-0.00	-0.00	0.97	-5.97
$Ca_{Na} - V_{Na}$	-0.60	-0.40	-4.11	0.59	-0.00	-0.00	-1.66
$Sr_{Na} - V_{Na}$	-5.19	-3.41	-9.81	-0.00	-0.00	-0.00	-5.99
$Sn_{Nb} - V_O$	-1.88	-0.99	-6.77	-2.17	-0.68	-0.17	-3.13
$V_{Na} - V_O$	-2.23	1.90	-7.63	2.91	0.35	-0.07	-2.59

Table 3.9: Relaxation volumes and elastic dipole tensor of neutral defects in orthorhombic NN.

electrostatic interactions between charged defect replicas, using the method proposed by Kumagai *et al.*[84] For each defect, we have computed all possible charge states, in order to obtain the charge transition levels (Eq. 2.28), and to properly describe the contribution of each defect species to the charge neutrality condition. As far as intrinsic defects are concerned, we have studied the formation energies of Na, Nb and O vacancies and the complex formed by a sodium and an oxygen vacancy (V_{Na}-V_O). Regarding extrinsic defects, we have evaluated the substitution on the Na-site with Sr and Ca (Sr_{Na}, Ca_{Na}) and on the Nb-site with Sn (Sn_{Nb}). Additionally, we have computed the formation energies of defect complexes. In particular, the complexes formed by the substitution on the Na-site with a neighbouring Na vacancy (Sr_{Na}-V_{Na} and Ca_{Na}-V_{Na}) and by Sn on the Nb-site with a neighbouring O-vacancy (Sn_{Nb}-V_O). In order to limit the number of possible combinations, and therefore the number of required DFT calculations, we have restricted out study to complexes formed by a maximum of two point defects. However, we do not exclude the possibility of complexes formed by three point defects, as we have found previously[107] that the complex V_{Na}-V_O-V_{Na} is likely present in cubic $NaNbO_3$ (Section 3.1).
The formation energies computed in the boundary regions of the stability diagram are plotted as a function of the Fermi level in Figure 3.16. The stars in the plot represent the charge transition levels, which are plotted separately in Figure 3.12. As far as intrinsic defects are concerned, Na vacancies are acceptors as expected, being stable in charge state of -1 across almost all the band gap. O vacancies are mostly donors in charge state +2, however they display a deep transition level from

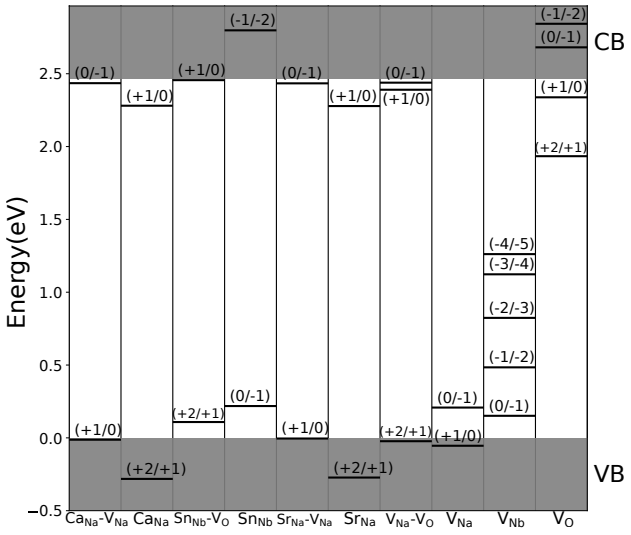

Figure 3.12: Charge transition levels in orthorhombic NN. The energy levels in the VB and the CB are indicated by the grey shaded areas.

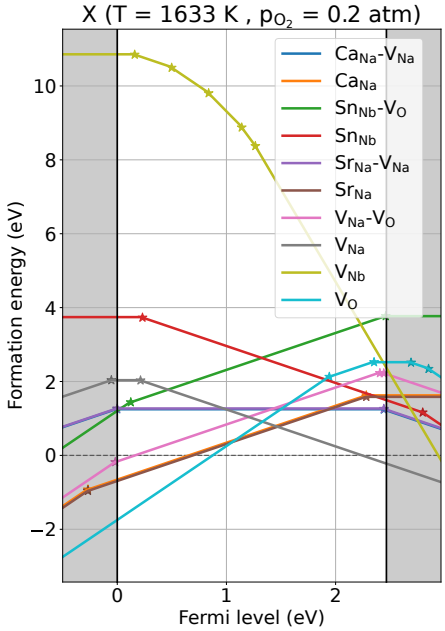

Figure 3.13: Defect formation energies in orthorhombic NN as a function of the Fermi level position for thermodynamic conditions representative of the experimental conditions (reported in Table 3.8). The stars on the formation energy curves represent charge transitions.

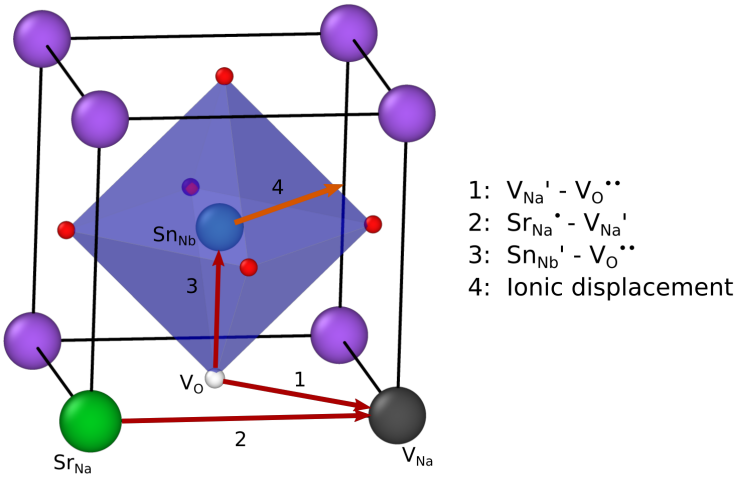

Figure 3.14: Configurations of the defect dipoles in the pseudo-cubic unit cell of $NaNbO_3$. The directions are compared with the ionic displacement in the center of the oxygen octahedron in the orthorhombic phase ($[110]_{PC}$).

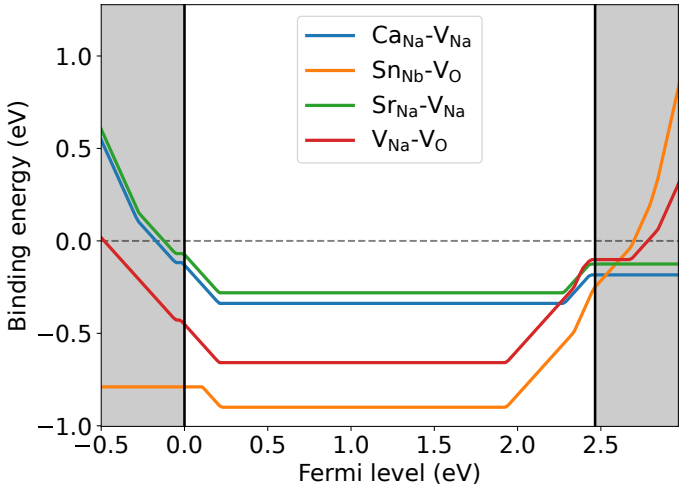

Figure 3.15: Binding energy of the defect complexes as a function of the Fermi level. The kinks correspond to charge transition points of the isolated defects.

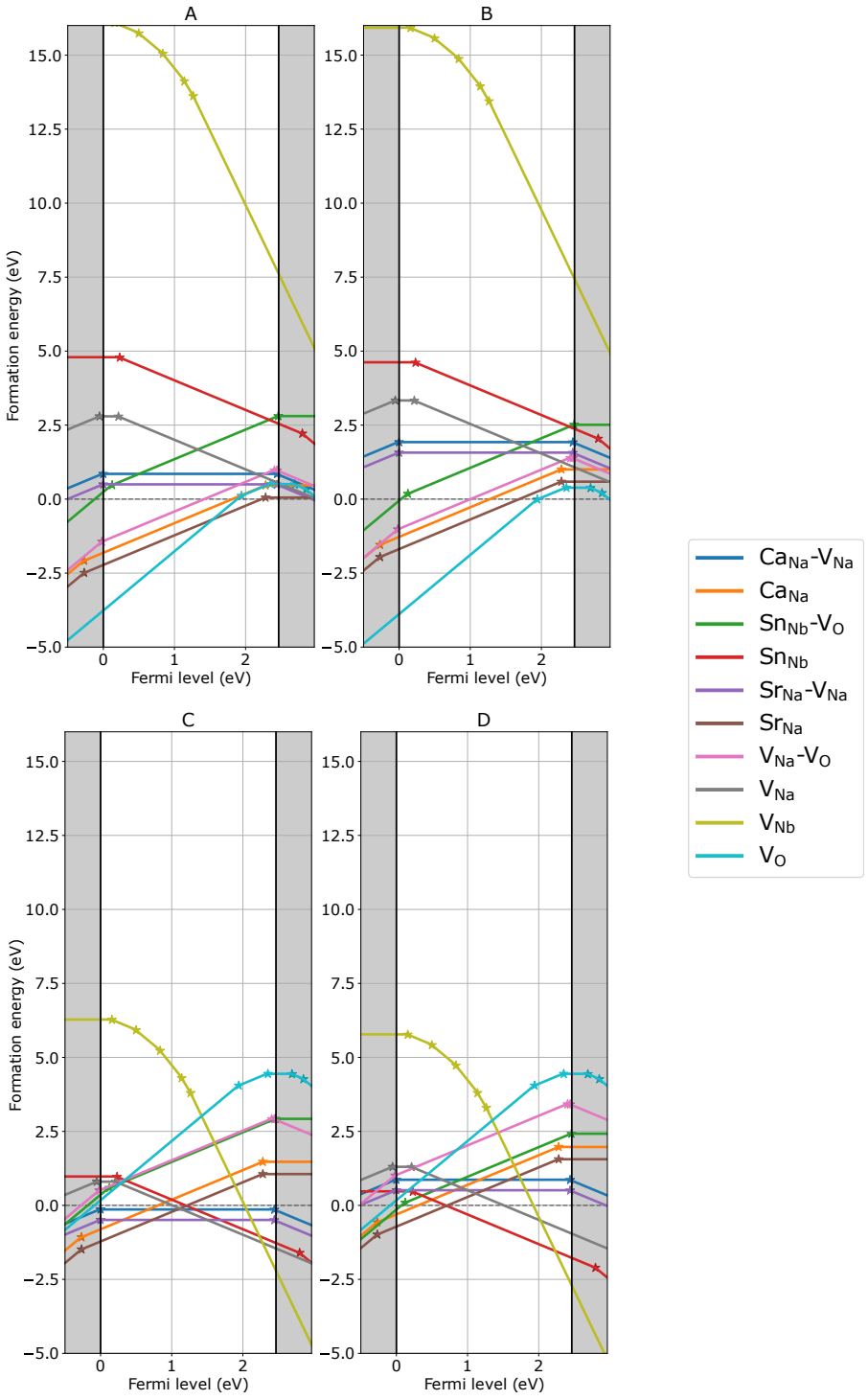

Figure 3.16: Defect formation energies in orthorhombic NN as a function of the Fermi level position for representative thermodynamic conditions A, B, C and D (shown in Figure 3.11). The stars on the formation energy curves represent charge transitions.

+2 to +1 at 0.5 eV below the CBM, with a shallower transition from +1 to 0 (0.1 eV below the CBM). Nb vacancies presents more scattered transitions across the gap, with -5 being the most stable from approximately mid-gap to the CBM. The stable charges of extrinsic defects also follow the behaviour of their common oxidation states. In fact both Sr_{Na} and Ca_{Na} are both donors with +1 charge state. They both present a +1/0 transition at 0.2 eV below CBM. Sn_{Nb} is an acceptor, with a 0/-1 transition at 0.2 eV above the VBM. Regarding the defect complexes, Sr_{Na}-V_{Na} and Ca_{Na}-V_{Na} are neutral, while Sn_{Nb}-V_O and V_{Na}-V_O are both donors in +1 charge state. In all reservoirs, we notice that defects involving Sr have lower formation energies than Ca, both for single substitutions and complexes. In oxygen-poor conditions (A and B) intrinsic defects are dominated by oxygen vacancies. The formation energy is low also for the V_{Na}-V_O complex, indicating its presence in large concentrations. Nb vacancies show considerably high formation energies, which implies a negligible contribution in these conditions. The substitution involving the Na-site presents low formation energies, especially Sr_{Na}. Oxygen-rich conditions present a different situation, with Na vacancies dominating the intrinsic defects, and Nb vacancies which show considerably lower formation energies with respect to O-poor conditions. This is due to the large range of $\Delta\mu_{Nb}$ between the extrema of the stability diagram (more than 10 eV). The balance shifts also for extrinsic defects, with Sn_{Nb} having mostly the lowest formation energies. In these points of the phase diagram, some of the defects can display formation energies which are particularly small (Sr_{Na} in point A) or even negative (Sr_{Na}-V_{Na} and Ca_{Na}-V_{Na} in point C). This is due to the fact that the reservoirs used for the calculations are at the boundary of stability of $NaNbO_3$. Computing the formation energies in these regions is useful to present a complete picture at the edges of stability of $NaNbO_3$. However, they are only hypothetical conditions and do not represent the experimental conditions during the synthesis of the material. To bridge this gap, we have computed the formation energies for temperature and pressure conditions that are present during sintering of $NaNbO_3$ (X point in Table 3.8). Figure 3.13 shows the result. We notice that none of the defects present extremely low formation energies, which is in line with our expectation, since we are mimicking the real conditions. However, it is interesting how the formation energies of V_{Na}, V_O and V_{Na}-V_O are still relatively low, which confirms their stability and that they will have an important contribution on charge neutrality. Moreover, extrinsic defects display energies within the same range, indicating their stability during the synthesis process. This explains how it is possible to push the doping with $SrSnO_3$ to large concentration values (up to 5% wt).[23]

3.2.6 Binding Energies

As already mentioned in Section 2.4.1, we have studied different defect complexes. Because the defects are charged, when they associate defect dipoles are formed. For simplicity, we show the configurations in the pseudo-cubic structure of $NaNbO_3$ in Figure 3.14. The arrows represent the directions of the defect dipoles, as well as the ionic displacement of the B-site (Nb and Sn_{Nb}) along the [110] pseudo-cubic direction.[2,123]
The key quantity to understand the stability of defect complexes is the binding energy (E_b), as in Eq. 2.27. It is therefore independent of the chemical potentials. It indicates the energy cost or gain that is correlated to the defects association. We show the binding energy as a function of the Fermi level for the four computed defect complexes in Figure 3.15. The change in slope are associated with the charge transitions of the different defect species. In particular, it can be seen that the donor complexes (Sn_{Nb}-V_O and V_{Na}-V_O) become less stable when approaching the CBM. It is interesting to notice that all complexes display a negative binding energy, indicating that single defects gain energy when they associate. This stability indicates that defect dipoles might be present in large concentration. Moreover, introducing a dopant, like $SrSnO_3$, introduces new types of complexes with respect to the bulk phase.

3.2.7 Dependency on Oxygen Partial Pressure

Bulk Case

As already shown for the cubic phase (Section 3.2.7), we can solve the charge neutrality condition for different oxygen partial pressure, to compute the Brouwer diagrams. At first, we have looked at the case of undoped $NaNbO_3$, in order to understand how the intrinsic defects behave, and to shed some light onto the defect equilibrium at the synthesis stage. We have limited the analysis only to single vacancies, thus excluding the charged V_{Na}-V_O complex, with the aim of comparing the intrinsic defect chemistry between orthorhombic and cubic phase (Section 3.1.5). We have reported the values of the concentrations of holes (n_h), electrons (n_e), and defect concentrations a function of oxygen partial pressure at sintering temperature (1633 K), as well as the self-consistently determined values of the electron chemical potential as a function of the oxygen partial pressure in Figure 3.17. The defect equilibrium in the orthorhombic phase follows the same trend as in the cubic phase. In fact, at low p_{O_2} O vacancies dominate, pushing

(a)

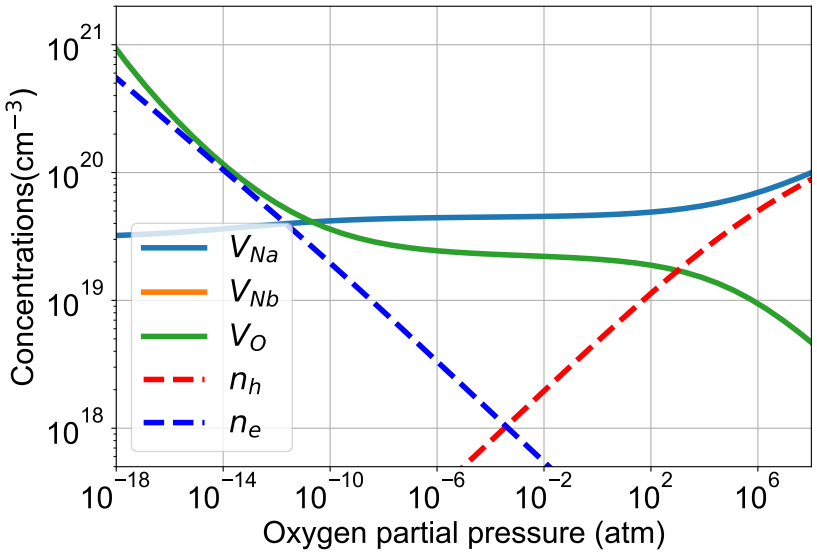

(b)

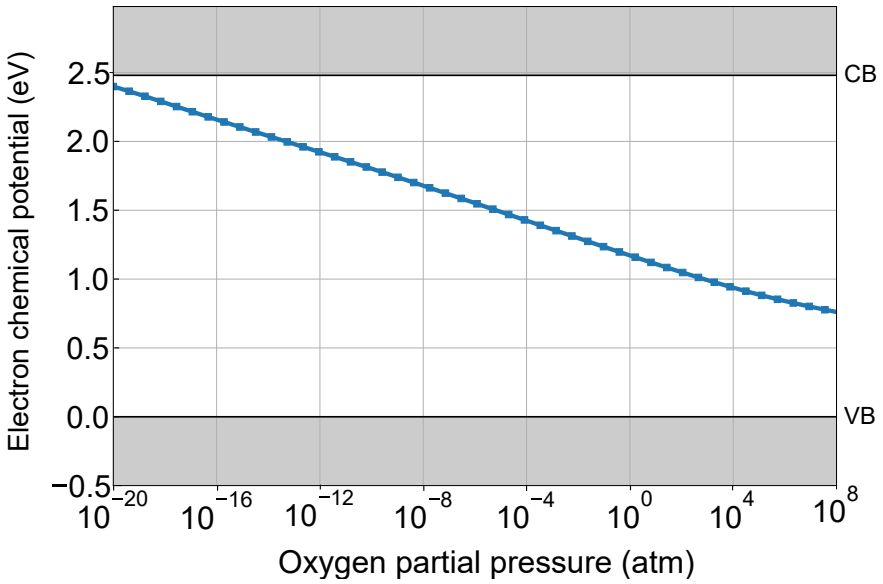

Figure 3.17: a) Concentrations of defects, electrons (n_e) and holes (n_h) in pure orthorhombic NN, as a function of the oxygen partial pressure at T = 1633 K. b) Electron chemical potential determined self-consistently as a function of the oxygen partial pressure.

μ_e close to the CBM. With increasing p_{O_2}, the balance shifts in favour of Na vacancies, thus shifting μ_e down towards mid-gap. Even though the energy gaps of the two phases are different (because of the different phases and the different xc-functionals), the relative positions of μ_e with respect to the band edges are following the same tendency. We show in Figure 3.18 the Brouwer diagram relative to the individual charged defects, rather than the total concentrations. It is interesting to observe that, for low p_{O_2}, O vacancies are mostly +1 charge. In the middle region, the more common situation with $V_{Na}{}'$ and $V_O^{\bullet\bullet}$ dominates. In the high p_{O_2} region, V_{Na} is still mostly in -1 charge state, but its neutral defect (V_{Na}^{x}) appears in increasingly large concentrations.
In order to study the electron chemical potential in the situation where defects are quenched (the concentrations at high temperature are preserved at low temperature), we have applied the method we have described in Section 2.4.8. In this method, even though the total concentrations of the defect spieces are fixed, their charge state can still change. This means that the relative concentrations of different charge states for every defect are not constant and can change with μ_e. We have shown in Figure 3.19 the Brouwer diagram relative to the quenched vacancies, and the values of electron chemical potential at high temperature (1633 K), room temperature (300 K) and in quenched conditions. We notice immediately that the quenched case is more intricate than the two equilibrated ones (Figure 3.19b). In fact, with increasing p_{O_2}, μ_e starts very close to the CBM, shows two "jumps", and ends very close to the VBM. The origin of these jumps can be found in the concentrations in Figure 3.19a. With low p_{O_2}, the concentration of V_O imposed by the high temperature is so high that, to compensate for it at low temperature, the electron chemical potential is pushed very close to the CBM. This has the effect of introducing many electrons into the system, and at the same time of stabilizing V_O^X. When p_{O_2} is increased, at 10^{-10} atm circa, the decrease in $[V_O]$ from the high temperature regime causes the first μ_e drop, making the neutral O vacancies change their charge state to +2. When p_{O_2} is further increased, $[V_{Na}]$ gets progressively larger in the high temperature, up to the point (10^{-3} atm circa) where the whole system changes from n-type to p-type (μ_e is below mid-gap). This dominance of V_{Na} causes the second and biggest jump in μ_e in the quenched system. In fact, at lower temperature, the number of charge carriers to compensate for the abundance of V_{Na} is much smaller than at high temperature. The equilibrium is thus reached when μ_e is much closer to the valence band and a number of Na vacancies are in neutral charge state, as we can see from the big increase in the concentration of V_{Na}^X in Figure 3.19a. At the same time, the shift in μ_e means that $V_O^{\bullet}$ becomes unstable in favour of $V_O^{\bullet\bullet}$, as shown by the fast

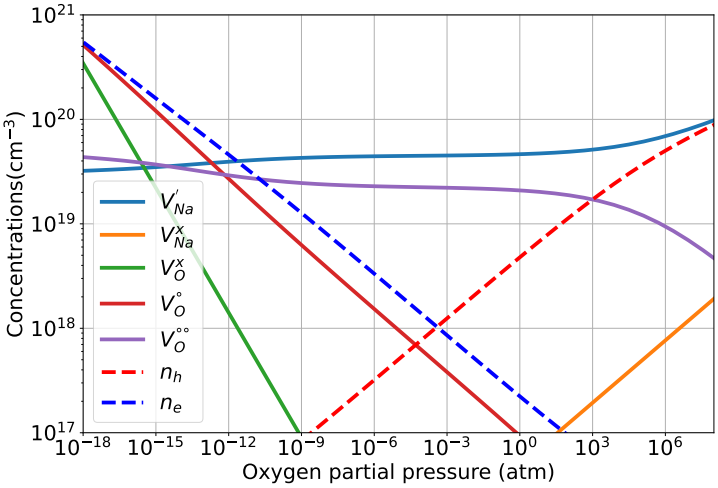

Figure 3.18: Concentrations Na and O vacancies at T = 1633 K in their different charge states, electrons (n_e) and holes (n_h) in pure orthorhombic NN, as a function of the oxygen partial pressure.

drop of $V_O^\bullet$ concentrations.
This analysis with vacancies in NN showcases the importance of including charge state dependencies when fixing concentrations, under the assumption that electronic defects can reach equilibrium even in quenched conditions. In fact, it shows that defect species altering their charge state is a decisive factor in the charge compensation mechanisms, ultimately determining the position of the electron chemical potential and the concentration of charge carriers.

Doped Case

The next step of this study is of course to include extrinsic defects and defect complexes into the charge neutrality condition. Moreover, we have studied different quenched situations, in order to obtain a picture of the possible limit conditions. More specifically, we have considered the equilibrium cases at high and low temperature, the case where all oxygen vacancies are free to equilibrate and Na and Nb vacancies are completely quenched from high to low T, the one where all O vacancies are quenched but the rest are allowed to equilibrate, and finally the one where all intrinsic defects are quenched. As we have already described in Section 2.4.8, all extrinsic defects are fixed to the experimental concentration

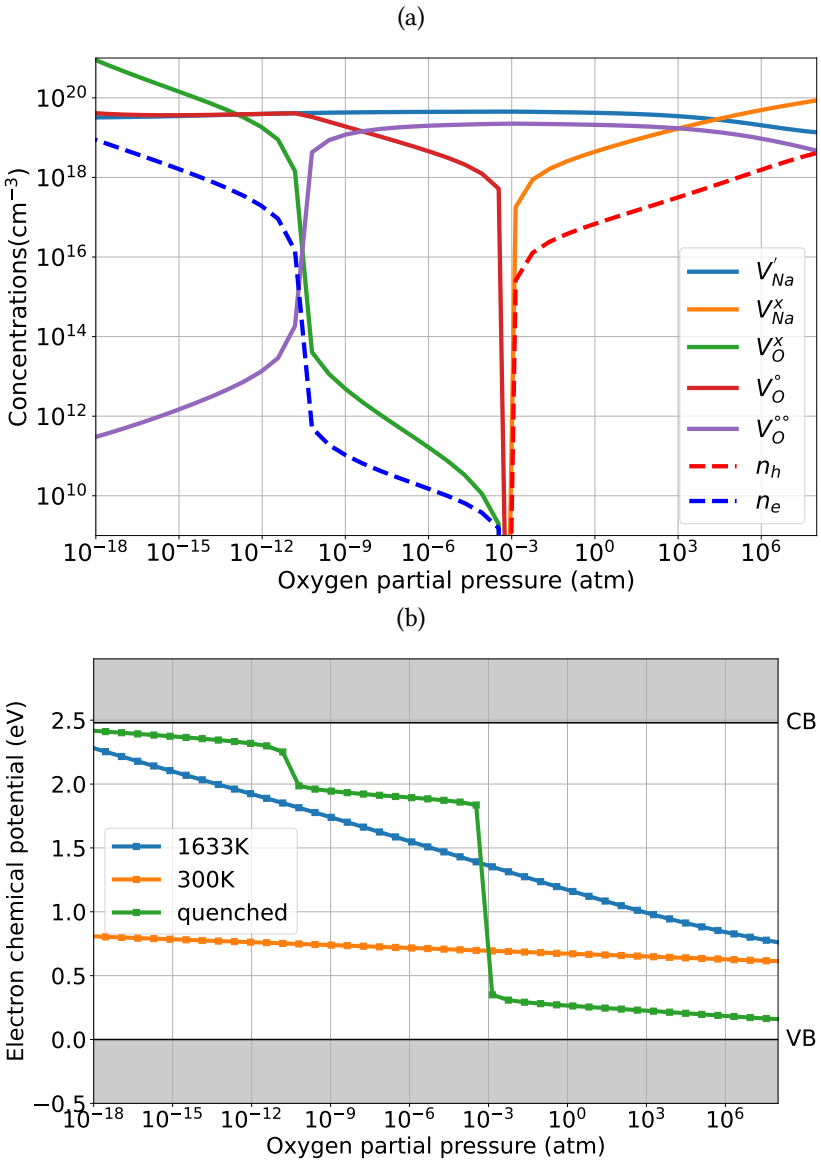

Figure 3.19: a) Concentrations of electrons (n_e), holes (n_h) and defects (quenched from 1633 K to room temperature) in their different charge states, in pure orthorhombic NN, as a function of the oxygen partial pressure. b) Electron chemical potential determined self-consistently as a function of the oxygen partial pressure in high temperature (1633 K), room temperature (300 K) and quenched conditions.

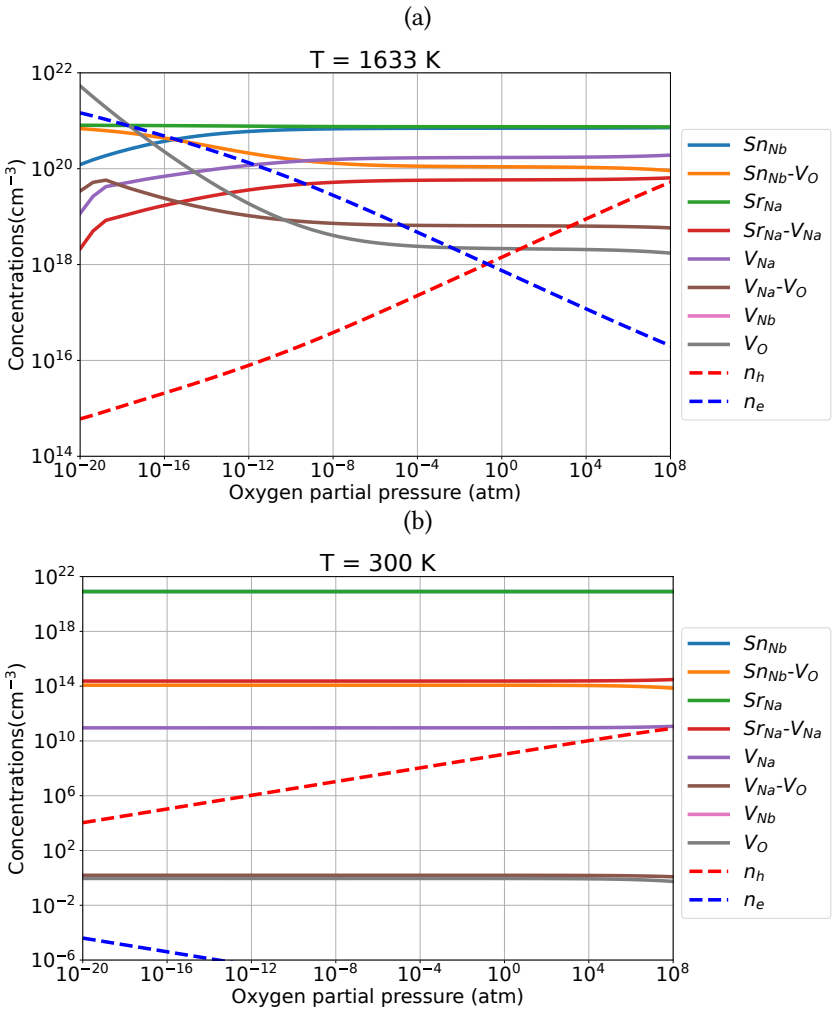

Figure 3.20: Concentrations of defects, electrons (n_e) and holes (n_h) as a function of the oxygen partial pressure, in doped orthorhombic NN, at high temperature (**a**) and room temperature (**b**) conditions.

of $SrSnO_3$ in sodium niobate. It is important to point out that all of these cases represent extreme situations, almost surely none of those would properly describe reality. However, they are useful because the experimental conditions lie within these limits, which provide a full picture on how quenching of different species influences the defect equilibrium. The results are shown in Figure 3.21.
At high temperature and low p_{O_2} (Figure 3.20a), oxygen vacancies (V_O) and the Sn_{Nb}-V_O complex show the highest concentrations. Both species are donors, re-

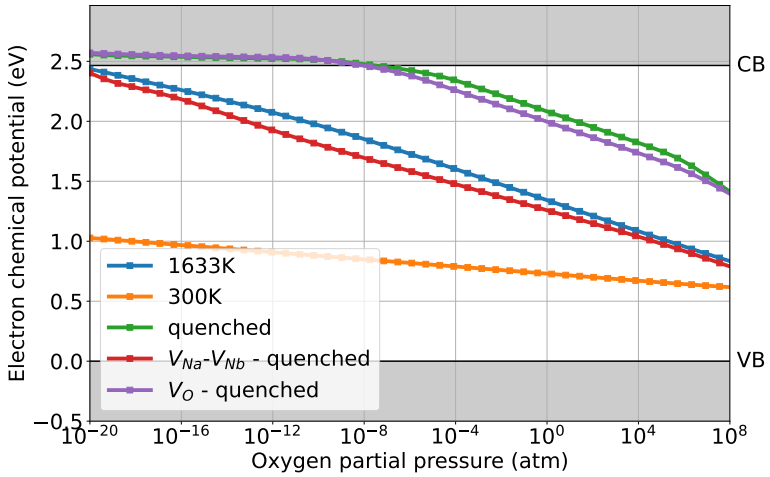

Figure 3.21: Electron chemical potential determined self-consistently in doped orthorhombic NN as a function of the oxygen partial pressure.

sulting in high free electrons concentrations. With increasing p_{O_2}, [V_{Na}] increases while the donors concentrations decrease, which results in greater free holes concentrations. The behaviour switches from *n*-type to *p*-type at p_{O_2} close to 1 atm. At lower temperature (Figure 3.20b), the dependence of the concentrations on p_{O_2} is less prominent, with [V_{Na}] being the dominant among the charged defects. This results in *p*-type behaviour for all p_{O_2} conditions. For both high and low temperatures the charges of the donor Sr_{Na} and the acceptor Sn_{Nb} compensate each other, having fixed the concentrations of the dopants. The concentrations of defect complexes are large, especially at high temperatures, confirming the expectations given by the negative binding energies (Section 3.2.6). The computed electron chemical potentials, at which the concentrations in Figure 3.20a and Figure 3.20b have been determined, are shown in Figure 3.21 by the blue and orange line, respectively. It is interesting to evaluate how the situation changes when we introduce quenching conditions. When we quench Na and Nb vacancies, μ_e follows the same trend of the high temperature equilibrium, with a slight shift towards the VBM, as a result of the higher concentration of the acceptor V_{Na} in the low temperature conditions. The equilibrium is modified dramatically if we quench O vacancies. In fact, as it can be seen from Figure 3.21, μ_e is shifted upwards towards the CBM, even above CBM for low p_{O_2}. This is a result of

combined donor contributions which are present in high concentrations in the quenched system, namely V_O, Sn_{Nb}-V_O and V_{Na}-V_O. The donors dominate even when we quench all defect species, as shown by the green line in Figure 3.21. In this case μ_e still follows the same trend, but it is slightly shifted upwards by the greater acceptor contribution of V_{Na}.

3.3 Trigonal Phase

In order to provide a complete picture for all temperature regimes, it is useful to compute the vacancies formation energies for the low temperature phase as well. However, this condition will not be explored in reality, where instead both the cubic and orthorhombic phases play a role. As outlined in Section 1.4, experimentally the low temperature phase of $NaNbO_3$ is trigonal. Both space groups *R3c* and $R\bar{3}$ have been reported.[124,125] At a DFT-level, the most stable phase at 0 K is the $R\bar{3}$,[116] with a small energy difference of 0.011 eV/atom. Since the two structures are very close to each other, we have chosen to investigate the $R\bar{3}$ phase, in order to avoid effects due to the slight lattice instability of the phase at 0 K. We will go deeper into this topic in Section 3.5. This decision, however, will not impact on the defect formation energies, since the difference between the two structures is practically negligible.

3.3.1 Computational Details

The details regarding the software used to carry out DFT calculations are consistent with Section 3.2.1. The chosen exchange-correlation functional is PBE-GGA.[56] All defect calculations were performed using a $2\times2\times2$ supercell, containing 80 atoms. The plane wave basis set was expanded up to a 550 eV cutoff energy. The Brillouin zone integration was performed using a Γ-centered $3\times3\times2$ k-mesh for unit-cell calculations and a $2\times2\times2$ k-mesh for supercell calculations. The atomic positions were relaxed until the Hellmann-Feynman forces on each atom were below 0.05 eV/Å. The density of states (DOS) were calculated using a Γ-centered $9\times9\times6$ k-mesh.

3.3.2 Electronic Structure

The band structure is shown in Figure 3.22. The character of the orbitals and the dispersion of the bad structure is similar to the case of the orthorhombic phase

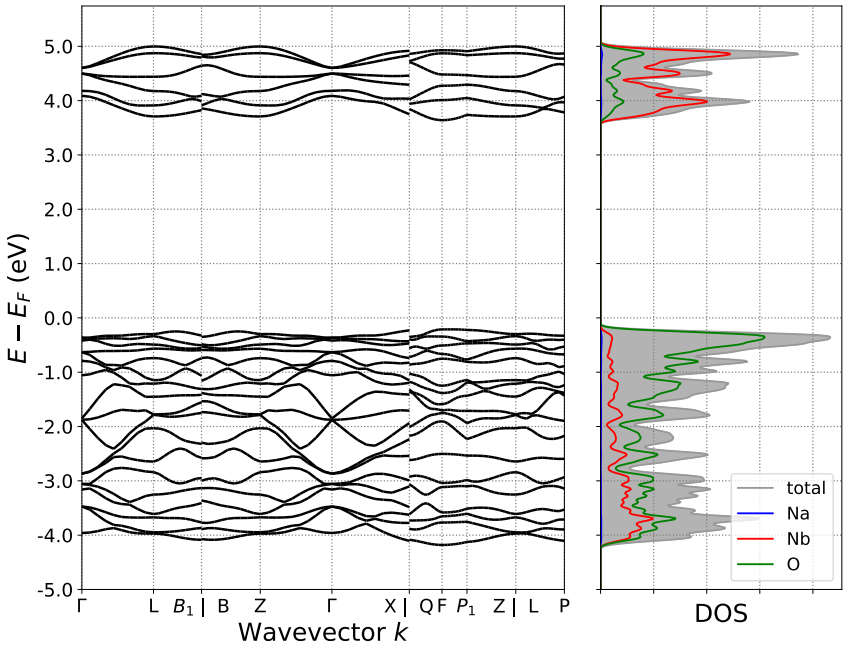

Figure 3.22: Band structure and density of states of trigonal $NaNbO_3$ (space group $R\bar{3}$).

	$\Delta\mu_{Na}$	$\Delta\mu_{Nb}$	$\Delta\mu_{O}$
A	-1.53	-0.76	-4.00
B	-0.89	-1.00	-4.13
C	-3.60	-10.69	0.00
D	-2.95	-11.33	0.00
X	-3.20	-10.64	-0.15

Table 3.10: Values in eV of the chemical potentials of the individual elements for each of the labelled regions in the stability diagram (Figure 3.11).

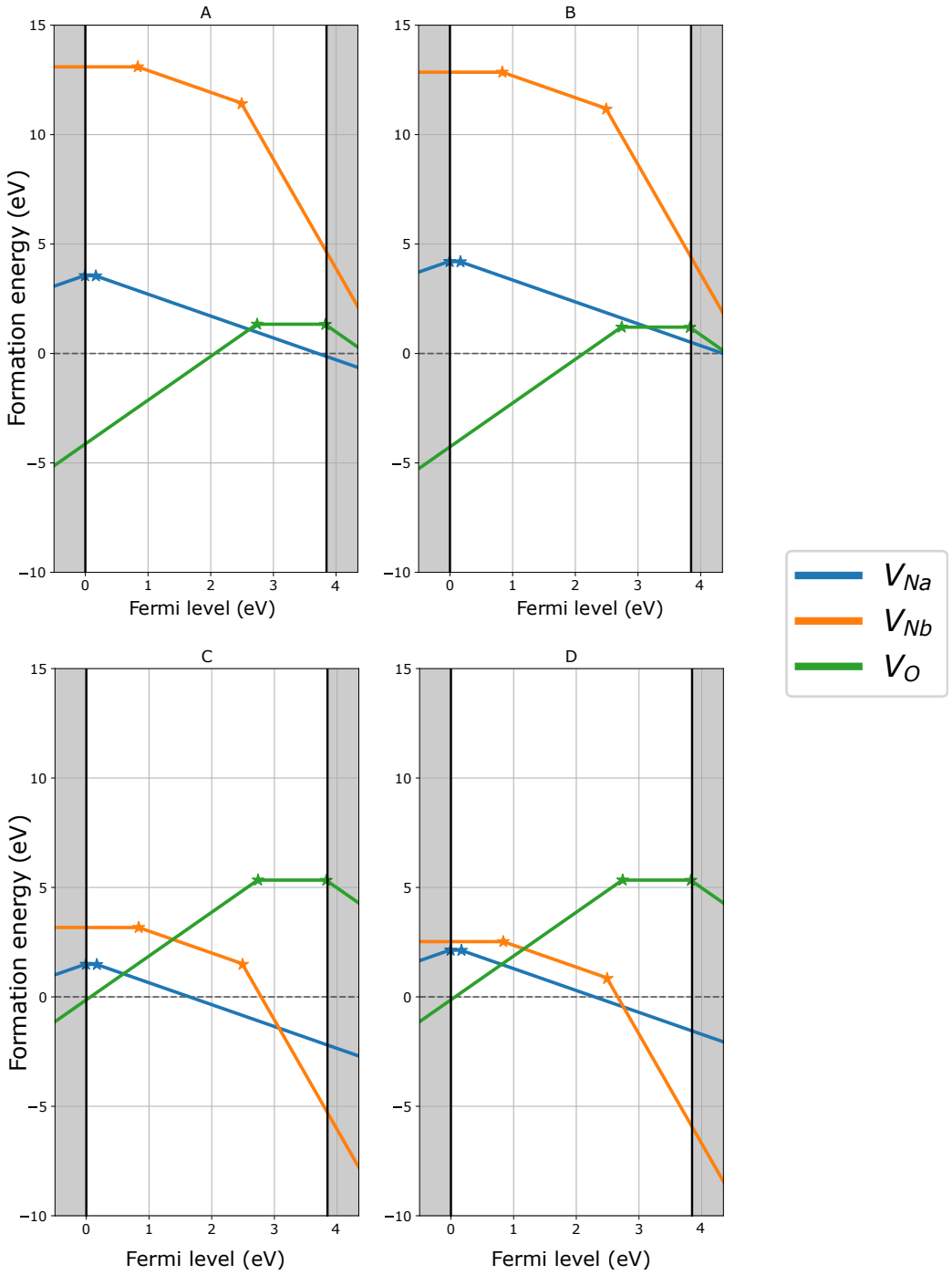

Figure 3.23: Defect formation energies in the trigonal phase of $NaNbO_3$, as a function of the Fermi level position for representative thermodynamic conditions A, B, C and D (shown in Figure 3.11). The stars on the formation energy curves represent charge transitions.

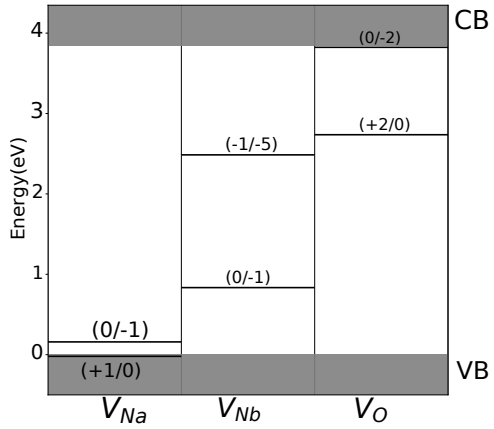

Figure 3.24: Charge transition levels of trigonal $NaNbO_3$. The energy levels in the VB and the CB are indicated by the grey shaded areas.

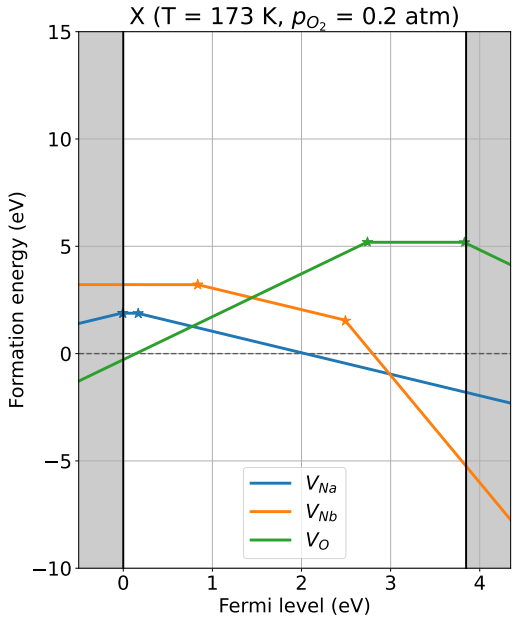

Figure 3.25: Defect formation energies in the trigonal phase of $NaNbO_3$, as a function of the Fermi level position for thermodynamic conditions representative of the experimental conditions (reported in Table 3.10). The stars on the formation energy curves represent charge transitions.

(Figure 3.10). In fact, the oxygen p orbitals constitute mainly the valence band, while the conduction band is made for the most part by niobium d orbitals. The main difference is in the energy gap, which for the trigonal phase is 3.85 eV, as opposed to the 2.48 eV of the orthorhombic phase.

3.3.3 Chemical Potentials

The thermodynamic reservoir used to compute the formation energies follow the same labelling systems as for the orthorhombic phase (Figure 3.11). Because at zero Kelvin the trigonal phase is more stable than the orthorhombic phase, the stability region of $NaNbO_3$ is slightly larger for the trigonal phase. The values are shown in Table 3.10. As for the two previous cases, we have computed the formation energies at the experimental conditions of $T = 173$ K and $p_{O_2} = 0.2$ atm, which are shown with the label X in Table 3.10.

3.3.4 Formation Energies

The formation energies computed in the boundary regions of the stability diagram are plotted as a function of the Fermi level in Figure 3.23. The formation energies in the experimental conditions are shown in Figure 3.25. The stars in the plot represent the charge transition levels, which are plotted separately in Figure 3.24. Just like for the other two phases, Na vacancies are acceptors as expected, being stable in charge state of -1 across almost all the band gap. O vacancies are mostly donors in charge state +2, and they display a considerably deep transition level from +2 to +1 at 1.1 eV below the CBM. The case of Nb vacancies deviates from the cubic and orthorhombic cases, with the formation energies being much smaller and in the same range of the other two defects, also for reservoir X. Moreover, it shows only two charge transition levels: from 0 to -1 and from -1 to -5, as opposed to the case of the other phases where we had many CTLs scattered across the energy gap.

3.4 Migration Barriers

As discussed in the previous sections, the assumption that the system is always able to reach thermodynamic equilibrium is not always appropriate. In fact, this would mean that the mobility of defects is large enough to allow diffusive processes in the bulk to bring compositional variations. While this is the case for

electronic defects (holes and electrons), it might not hold true for atomic defects. The diffusity of defects depends on the migration enthalpy ΔH_m:

$$D = D_0 e^{-\frac{\Delta S_m}{k_B}} e^{-\beta \Delta H_m} \tag{3.2}$$

where D_0 is the diffusion coefficient, ΔS_m is the migration entropy and β is $1/k_B T$. Therefore, the determination of the migration barrier will help us understand which defect species are more mobile, and therefore more likely to reach equilibrium, and which species are more likely to be quenched from the synthesis stage due to their low mobility. Therefore, we have studied the migration energies of the relevant Na and O vacancies in their most stable charges (-1 and +2, respectively) in the cubic, orthorhombic and trigonal phases, with the method described in Section 2.3. The results are shown in Table 3.11. In the cubic and orthorhombic phases O vacancies are more mobile than Na vacancies, which follows the expectations, given that O atoms have much smaller radius than Na atoms. The barrier for V_O is particularly small (0.4 and 0.3 eV, respectively), which indicates that it will be considerably mobile and it is unlikely to be completely quenched. Na vacancies, on the other hand, display a higher barrier (1.4 eV in both cases), which means a lower mobility and a higher probability to be frozen at

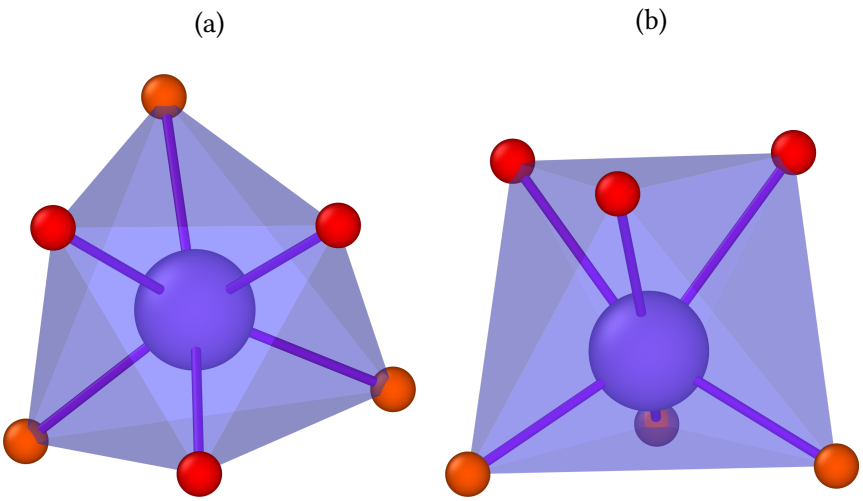

Figure 3.26: Environment of Na in the trigonal phase of $NaNbO_3$. The O atoms with shorter Na-O bond leng are shown in red, the more distant O atoms from Na are shown in orange. (a) Projection down the triad axis of the distorted trigonal prism. (b) Three dimensional view of the trigonal prism.

	$\Delta E^m_{V_O}$ (eV)	$\Delta E^m_{V_{Na}}$ (eV)
trigonal	0.7	0.5
orthorhombic	0.3	1.4
cubic	0.4	1.4

Table 3.11: Computed vacancy migration energies of O and Na vacancies in different phases of $NaNbO_3$ in units of eV.

room temperature. Therefore, for the cubic and orthorhombic phases, we expect that the real case would be closer to the situation where V_{Na} is quenched (shown by the red line in Figure 3.21), where quenching leads to the increase in acceptors concentrations and consequently to a shift of the electron chemical potential towards the VBM.
The result is more surprising in the case of the trigonal phase, where the migration barrier of the Na vacancy drops to 0.5 eV, and the barrier of the O vacancy increases to 0.7 eV. The low barrier of the Na vacancy is particularly interesting. Given the size of Na, we expect the diffusion energy barrier to be higher, as moving around a larger atom in the lattice is energetically expensive. A possible explanation for this phenomenon can be found in the local environment of the Na ions. In fact, the environment of Na atoms in the trigonal phase is irregular and unusual.[124] Their coordination number is 6, instead of 12-fold coordination of the typical perovskite structure. Moreover, the polygon that Na forms with the coordinated O atoms is not an octahedron, but it can be best described as a distorted trigonal prism. A recreation with the software OVITO[119] of the figures found in Ref. 124 are shown in Figure 3.26. As shown by the different colors in the figure, in this atomic arrangement the Na-O distances are uneven, with three O atoms being closer (shown in red) and the remaining three further apart (orange). This unstable structure is imposed by the displacements of the Nb atoms, which for this lattice symmetry are along the same direction. This unbalanced relaxed position of the Na ion can be a factor contributing to its low barrier. If the start- and end-points of the migration path are higher in energy, the distance to the top of the energy barrier is smaller. Additionally, the volume of the orthorhombic phase is smaller than that of the trigonal phase, because of the smaller volume associated with Na.[124] Therefore, a migrating atom in the trigonal phase will have more space to diffuse, leading to a smaller barrier. In any case, in order to shed more light onto this topic and confirm these reasons, more calculations should be conducted. In particular, given the uneven distances between the atoms in

this structure, different NEB calculations for different atoms of the same species should be performed, as the vacancy barrier may depend on which atom is chosen for the computation. Such a detailed dive into vacancy migration in $NaNbO_3$, however, goes behond the scope of this work. Lastly, even though the low temperature phase is an interesting case study, it will not have an influence in our studies of the impact of defects on AFE properties, as the two phases of interest are the ones stable at high temperature (at the synthesis stage) and room temperature.

3.5 Influence of Phase Stability on Defect Properties

In the earlier sections, we have presented our defect thermodynamics studies for three different phases of $NaNbO_3$, namely the trigonal (space group $R\bar{3}$), orthorhombic (s.g. *Pbcm*) and cubic (s.g. $Pm\bar{3}m$) phases, stable in low temperature, room temperature and high temperature conditions, respectively. In Section 3.3 we have introduced the importance of lattice instability for the high temperature phases with DFT. In fact, in our calculations we rely on static lattice relaxation (0 K), which looks for a minimum in the energy landscape determined by solving the Kohn-Sham equations (Section 2.2). Without temperature contributions, the high temperature phases will be unstable with respect to the structure stable at 0 K. Therefore, in the absence of symmetry constraints, the high temperature phases would relax to the 0 K structure. For these reasons, when we compute the high temperature phases, we constrain the symmetry to that of the input structure space group, as implemented by the software VASP[103] (Section 3.1.1). However, when we introduce defects, the relaxation of the local environment around the defect might result in additional energy gain, which is dictated by the instability of the structure with respect to the phase stable at 0 K. To put it simpler, introducing a defect is less expensive because the initial phase is only a local minimum in the energy landscape.
As an example, let us consider the case of perovskites with pseudo-cubic structures, like $NaNbO_3$. The stable phase at high temperature has a cubic perovskite structure, with perfectly aligned Nb-O octahedra, as visualized in Figure 3.27. As we decrease temperature, the Nb atoms will displace from the center of the octahedron, and the O-octahedra will tilt with respect to each other, as we observe in the orthorhombic and trigonal phase.[19] When we introduce an oxygen vacancy, in the vicinity of the defect the structure relaxes by introducing O-octahedra tilting, which is the signature of the lower temperature phases (Figure 3.27).

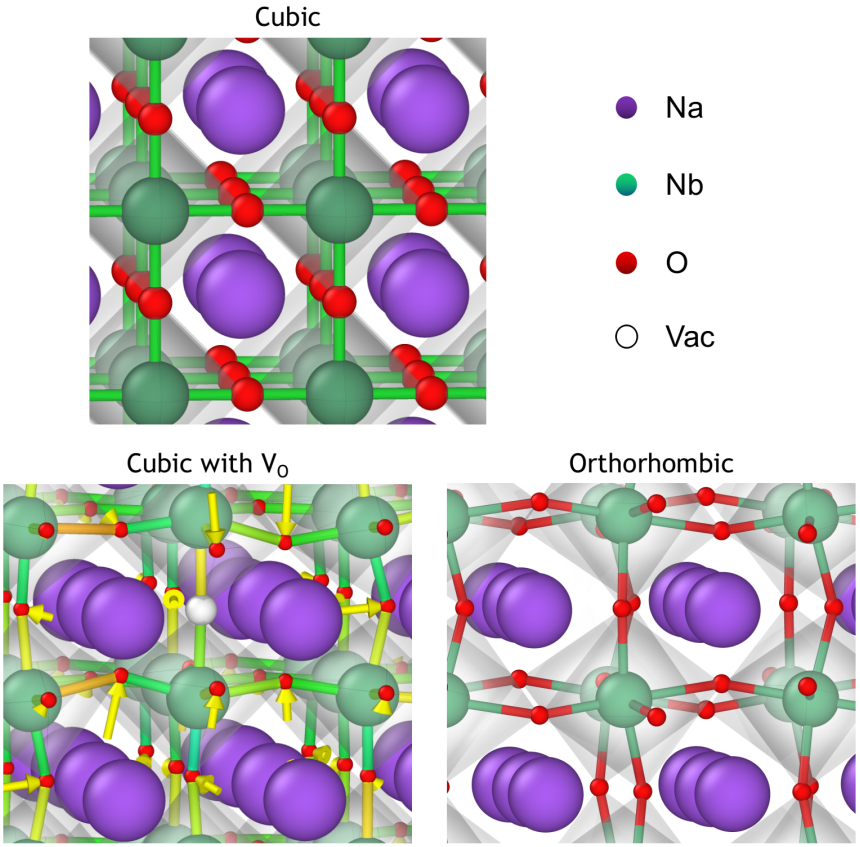

Figure 3.27: Structures stable at high temperatures will show lattice instabilities with static (0 K) DFT. When introducing an O vacancy in the high temperature phase (cubic), the local environment relaxes by tilting the O-octahedra, which are a prerogative of the low temperature phases (*e.g.* orthorhombic). This relaxation process yields a total energy gain which translates in lower defect formation energies.

The energy gained by this relaxation process makes the defect energetically less expensive, which translates in lower defect formation energies. To our knowledge, this problem has not yet been systematically addressed in the *ab initio* defects thermodynamics community. In our case, the main focus of this study is the RT orthorhombic phase, which is already very close in energy with the trigonal phase stable at 0 K (the energy difference is 15 meV). Nonetheless, it is interesting to compare the formation energies (ΔE^f) and charge transition levels (CTL) of vacancies in the three phases we have presented in the previous

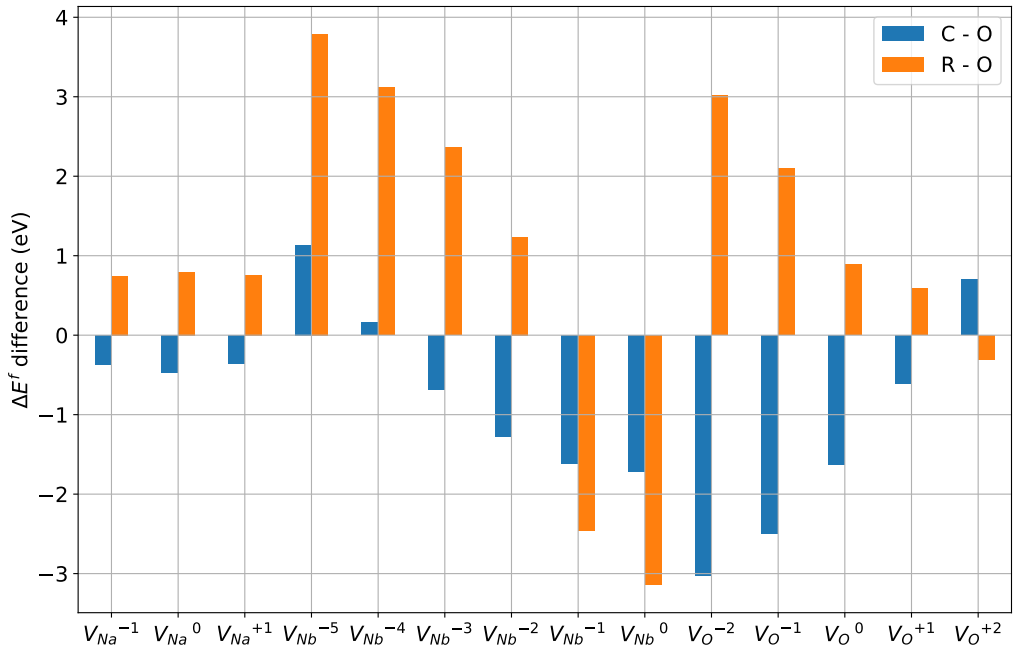

Figure 3.28: Difference in formation energies of vacancies between the cubic (C), orthorhombic (O) and trigonal (R) phases in $NaNbO_3$. The orthorhombic phase is used as reference.

sections. For consistency of the xc-functional, we have repeated the calculations of the C phase with the PBE functional. We show in Figure 3.28 comparison of the formation energies. We have taken the RT orthorhombic (O) phase as a reference and computed the ΔE_f difference with the cubic (C) and trigonal (R) phases. It is worth noting that, in this calculation, the only terms in Eq. 2.26 which do not cancel out are the total energies and the image-charge corrections. In the first place, we can observe that for Na and O in their more relevant charge states (-1 and +2, respectively) the ΔE^f is relatively small (< 1 eV). The situation is different for Nb vacancies, where, given the large scattering of CTLs across the gap (Figure 3.4 and 3.12), is also impossible to define which of the charge states is more relevant. Secondly, we notice that, excluding three cases, the formation energies of the R phase are the largest. Additionally, we see that there is a trend where the formation energy of the O phase lies in the middle between ΔE^f_R and ΔE^f_C ,with the exception of V_{Nb} in charge states -5,-1 and 0. Lastly, we can observe that, for V_{Nb} and V_O, ΔE^f_R increases with increasing negative charge, while for ΔE^f_C the situation is the opposite. As a first quantitative approach to

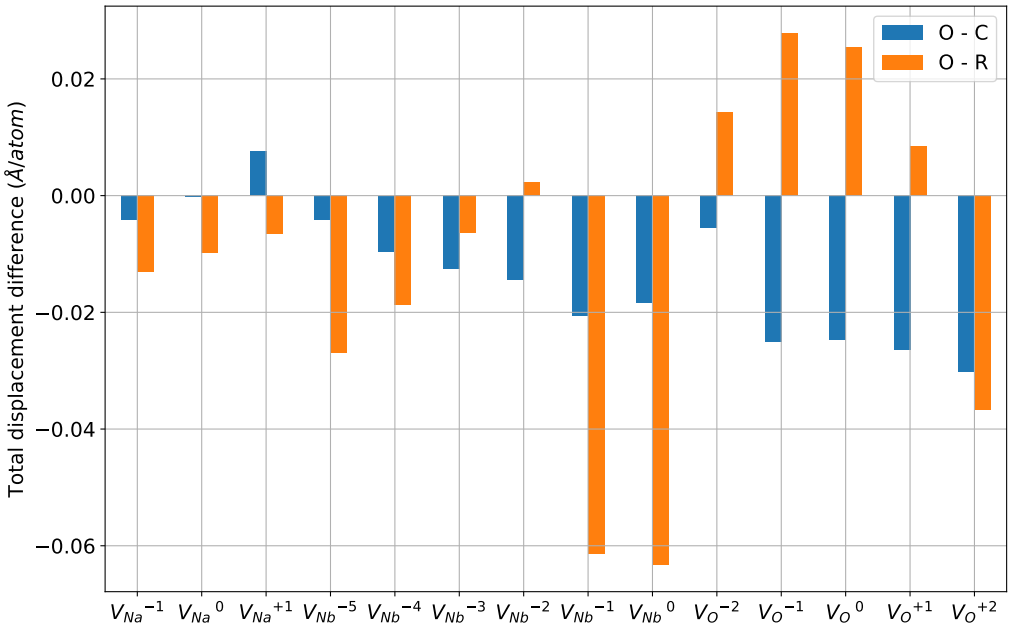

Figure 3.29: Difference in the sum of all atomic displacements (per atom) in the final relaxed structure relative to the initial unrelaxed one, between the cubic (C), orthorhombic (O) and trigonal (R) phases in $NaNbO_3$. The orthorhombic phase is used as reference.

the previous discussion regarding lattice relaxation, we have computed the sum of all atomic displacements (per atom) in the final relaxed structure relative to the initial unrelaxed one, in order to provide a measure of how much the lattice has relaxed to adapt for the presence of the defect. The results are shown in Figure 3.29. Unfortunately, this approach is inconclusive, as a clear trend of comparinson with the difference in formation energies is not visible. The behaviour across the defect species is very diverse, and it is heavily dependent of the charge states of the defects. This is not surprising, as the deciding factor is not the magnitude of the displacement itself, rather the quality of it, this meaning the path in the energy landscape. Therefore, a deeper look into the displacive mechanisms is required. Moreover, more factors should be taken into consideration for a more detailed analysis, such as the relaxation volumes of charged defects, localization/delocalization of the defect charge, *et cetera*. This analysis, however, would require extensive calculations which are outside of the scope of this work. In conclusion, with the exception of V_{Nb}^{0}, V_{Nb}^{-1} and $V_{O_2}^{+2}$, we can generally conclude that formation energies get progressively higher when going from high temperature

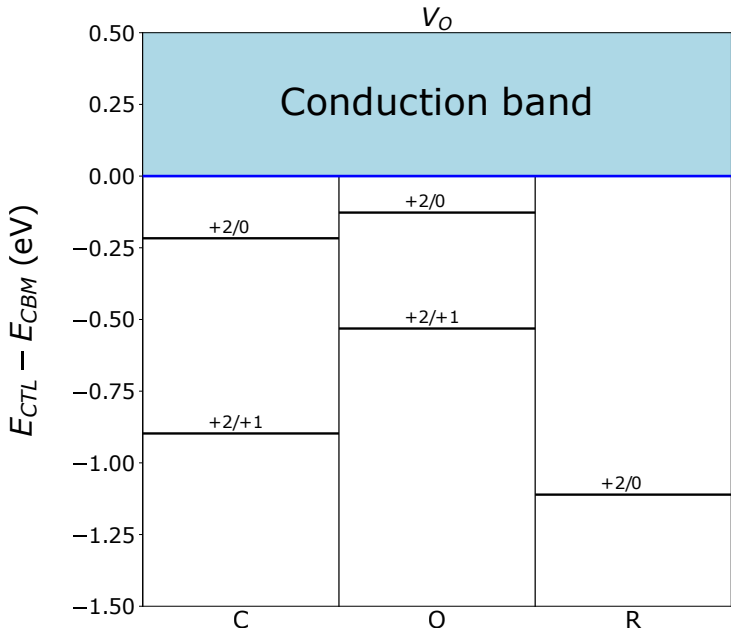

(a)

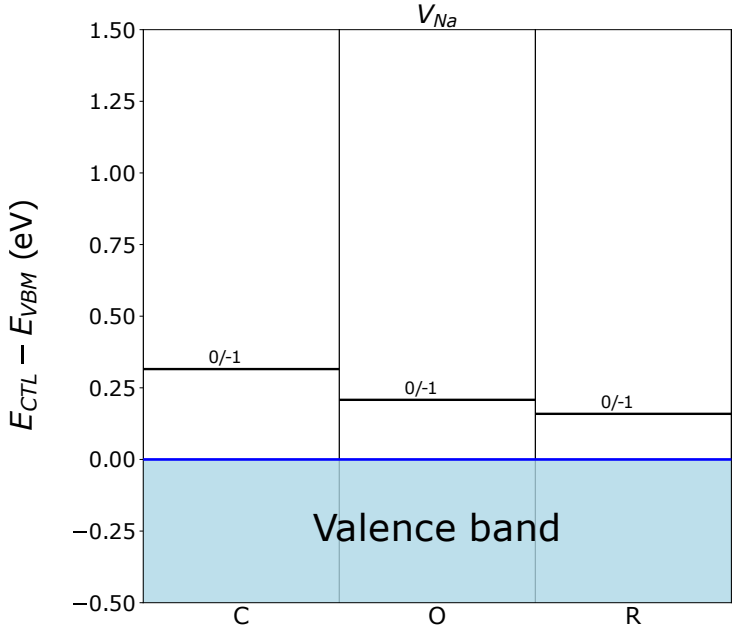

(b)

Figure 3.30: Distance from the band edges of the most relevant charge transition levels (CTL) for oxygen (**a**) and Na (**b**) vacancies for the cubic (C), orthorhombic (O) and trigonal (R) phases in $NaNbO_3$.

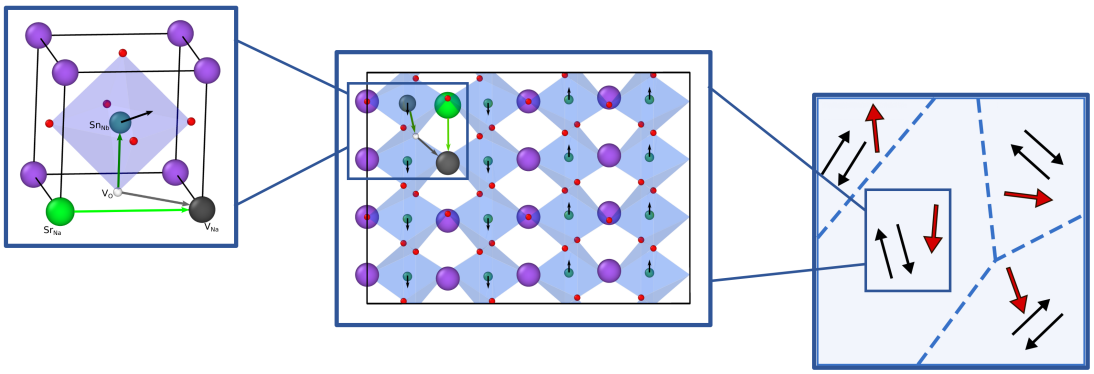

(a) Multiscale representation of defect dipoles, ionic displacements and lattice polarization. The first picture on the left shows the pseudo cubic cell. The image in the center shows a 2x2x1 supercell of the orthorhombic cell (space group *Pbcm*) with the antiparallel displacements of Nb atoms and defect dipoles. The picture on the right represents schematically the antiferroelectric phase with defect dipoles in different domains.

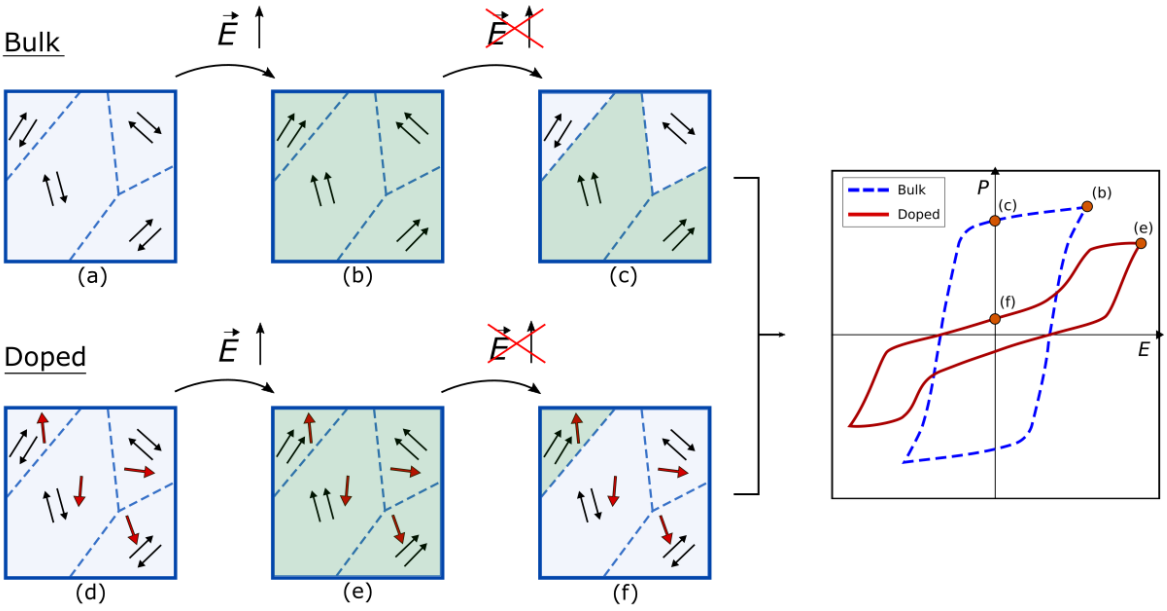

(b) Field switching mechanisms in bulk and doped $NaNbO_3$. In the bulk material, once the electric field is applied, the system undergoes the AFE-FE phase transition (point **b**). When the field is removed, since the FE phase is metastable, not all dipoles can be switched back to an AFE configuration, which results in remanent polirization (point **c**). In the doped case, when the field is removed, the defect dipoles provide an additional restoring force which increases the reversibility of the FE-AFE phase transition (point **f**) and decreases the remanent polarization.

Figure 3.31: Schematic representation of the influence of defect dipoles on the *P-E* loops, arising from their interaction with lattice polarization and external field, with consequent contribution in the switching mechanisms.

to low temperature phases. However, the exceptions and the dependencies on the charge states still need to be understood, calling for a deeper investigation on this topic.
Charge transition levels (CTL) are another important quantity which is interesting to compare. The energy gaps are different among the three phases. What is most interesting, however, are the distances between the CTLs and the band edges. The main CTLs for Na and O vacancies are shown in Figure 3.30. The first observation is that for O vacancies (Figure 3.30a) the trigonal phase (R) does not display a window of stability for the +1 charge states, where both the cubic (C) and orthorhombic phase also show a +2/+1 transition level. The +2/0 CTL is shown also for these phases for comparison. Moreover, in the R phase the +2/0 is much deeper (further from the CBM), by almost 1 eV, while for the C and O phase is shallower (closer to the CBM). The +2/+1 level is deep in both the C and O phases, and in the C phase is circa 0.4 eV deeper. In the case of Na vacancies (Figure 3.30b), the 0/-1 CTL is much closer for all three phases. Moreover, they are relatively shallow and get progressively shallower from the C to the R phase (from 0.3 to 0.15 eV distance from the VBM).

3.6 Defect Dipoles

In Section 3.2.6 we have seen how single point defects in $NaNbO_3$ can associate, thus forming a defect complex. In particular, by analysing the binding energy (Eq. 2.27, Figure 3.15), we have discovered that the defects shown in Figure 3.14 gain energy by associating, which means that the complexes are stable and present in large concentrations (Figure 3.20). When charged defects form associates, they introduce electric dipoles. Defect dipoles interact with the lattice polarization in the AFE and FE structures of $NaNbO_3$, as well as with an external electric field. Hence, the presence of defect dipoles is a factor that influences the field switching mechanisms, which ultimately can alter the *P-E* loops, as it has been already suggested both for ferroelectrics and antiferroelectrics [11,21,126] (Section 1.7.1). Figure 3.31 shows a schematic representation of these concepts. In the bulk material, once the electric field is applied, the system undergoes the AFE-FE phase transition (point **b** in Figure 3.31b). When the field is removed, since the FE phase (Q) is metastable, not all dipoles can be switched back to an AFE configuration,[22,127] which results in remanent polarization (point **c**) and a ferroelectric-like *P-E* loop. Now we look at the doped material. Because in the AFE phase the internal electric field is absent, a distribution of randomly

oriented defect dipoles is installed. Moreover, we assume that the kinetics of dipole switching is too slow to be able to follow the electric field, since all the dipoles require multiple diffusion steps to switch direction. In this situation, when the field is removed, the defect dipoles provide an additional restoring force, which increases the reversibility of the FE-AFE phase transition (point **f**). Therefore the remanent polarization is decreased, which consequently increases the recoverable energy.

3.7 Conclusion

In sodium niobate, the intrinsic defects equilibrium is dominated by Na vacancies (singly charged acceptor) and O vacancies (doubly charged donor), which are present in high concentrations. The position of the Fermi level at sintering temperature depends on the oxygen partial pressure (p_{O_2}). The character of the semiconductor shifts from n- to p-type with increasing p_{O_2}. When doped with Sr and Sn, at high temperature and low p_{O_2} NN is an n-type semiconductor, while for high p_{O_2} the system becomes p-type. At room temperature the material is p-type. When all defects (or just O vacancies) are quenched from high temperature, the Fermi level shifts towards the CBM, while quenching Na and Nb vacancies produces a less pronounced shift towards the VBM.
While these results represent a solid foundation in the understanding of defect thermodynamics in $NaNbO_3$, it is nonetheless important to stress some important limitations of the computational methods we have employed. In order to analyse the orthorhombic and cubic phase of $NaNbO_3$, we performed total energy defect calculations on structures that are stable at finite temperatures, but only metastable at 0 K. Structural instability at 0 K with might introduce additional relaxation mechanisms, leading to energy contributions which would not be present at finite-temperature. In Section 3.5, we presented only a preliminary analysis on the connection between phase hierarchy and formation energies. In order to find a descriptor for this phenomenon, and possibly introduce corrections, a more systematical and detailed analysis is necessary. Another important aspect to keep in mind is that the formalism of point defects thermodynamics[69–71] is physically meaningful only when the number of point defects is much smaller than the number of available sites, so that defects do not interact with each other (also for the case of defect complexes, which are treated as an individual species). In other words, is valid only for ideal solutions. This assumption is unfortunately not always true. In fact, in the field of ferroelectric/antiferroelectrics, more of-

ten than not, chemical modification is much closer to creating solid solutions rather than doping, meaning the concentration of extrinsic defects are much closer to parts per hundred rather than parts per milion. In such a context, if the interaction between defects is not negligible, the current point defect formalism might fail. On the other hand, approaching the problem from the perspective of solid solutions, rather than that of a doped system with an ideal solution of point defects, would increase the complexity and the computational cost, with the limitation of of not being able to capture properly the physics and compensation mechanisms of charged defects. A possible approach to tackle these limitations is discussed in Section 5.1.

We encounter additional challenges when comparing these results to the experiment, since $NaNbO_3$ is a very complex ceramic. In fact, its properties are extremely sensitive to the sample's history. Due to the high synthesis temperature, the volatilization of Na produces a deviation of the composition from the originally designed stoichiometry and causes the dielectric properties of the sintered samples to deteriorate.[16] Furthermore, we know from our experimental colleagues that the particle density and grain size of NN depend on which polymorph of Nb_2O_5 is used at the synthesis stage, which is unfortunately (to our knowledge) not discussed in publications. Moreover, measurements of defect concentrations in NN are not reported in the literature, most likely due to the aforementioned complications in this system, which makes a direct comparison between experimental and computational data impossible. Bein *et al*[128] have measured the Fermi level with x-ray photoelectron spectroscopy (XPS) and the conductivity in bulk, Sr- and Ca-doped NN. However, since experimentally the system is in contact with a substrate, they can only measure a range in which the Fermi level lies, depending on the nature of the substrate. Additionally, since the defect concentrations are unknown, we do not know the influence of the processing history of the sample on its defect distribution and Fermi level. The same considerations apply also for the conductivity measurements. In this case, we have the additional complication that the conductivity is a result of the combination of a multitude of conduction mechanisms, which can be hard or even impossible to decouple. On top of that, calculating the conductivity computationally requires several additional calculations, *e.g.* diffusion barriers of all defects species and phonon frequencies, which go outside the scope of this work. Last but not least, the *P-E* loops measured experimentally are the result of an even more complicated combination of effects, concerning different length scales. In particular, it is possible that point defects, line defects, domain size, grain size, particle density, etc., all have an impact on the antiferroelectric properties, thus making

extremely challenging to directly correlate the defect chemistry to the measured *P-E* loops. Studying the impact of defect dipoles on the AFE loops might be a step in this direction, since there is a direct correlation between defect dipoles, displacive dipoles and the applied external field. Of course, this would require a model which describes length scales that DFT cannot capture. A possible solution would be to start from the computed concentrations and integrate the defect dipoles in a phase-field approach which can model the switching mechanisms, as the one presented by Liu and Xu.[129]

4 Silver Niobate

Just like sodium niobate (NN), silver niobate (AN) is a candidate as a lead-free antiferroelectric (AFE) material for energy storage (Chapter 1). We have chosen to study defects in two phases of interest: the high temperature cubic phase (space group $Pm\bar{3}m$) and the room temperature orthorhombic phase ($Pbcm$), with additional focus on the latter. As opposed to NN, no low temperature phase of AN has yet been observed experimentally.[16]

4.1 Chemical Potentials

As we have seen in the previous sections, we need to define the thermodynamic conditions which enter the calculation of the defect formation energies. Obtaining the ranges for the chemical potentials for AN, however, presents some complications. Table 4.1 reports the stable phases in the ternary Ag-Nb-O phase diagram reported by the Materials Project Database,[116,117] with the addition of $AgNbO_3$. The value of the energy above the convex hull shows that, according to DFT, $AgNbO_3$ (AN) is not stable with respect to the competing phases, in particular to the decomposition in Ag_2O and Nb_2O_5. Experimentally, however, AN can be synthesized. The reasons behind this discrepancy are to be found in the nature of DFT, which cannot take into account the effects of temperature and kinetics. This is important especially in the case of AN, where it is known that kinetics plays a very important role in the synthesis process (Section 1.4).[24] Moreover, the value of the energy above the convex hull for AN is small (0.038 eV), which further confirms that phase stability can be altered with the contribution of kinetics and temperature. This phase instability means that AN will not be present in the Ag-Nb-O ternary diagram, meaning that the approach to compute chemical potentials used in the previous chapter (described in Section 2.4.5) is not accessible. On the other hand, we know that the precursors for the synthesis of $AgNbO_3$ are Ag and Nb_2O_5.[25] Therefore, since $AgNbO_3$ is in contact with these

two compounds at the synthesis stage, we can use them to obtain the values of the chemical potentials:

$$\begin{cases} \Delta E^f[\mathrm{Ag}] = \Delta\mu_{\mathrm{Ag}} = 0 \\ \Delta E^f[\mathrm{Nb_2O_5}] = 2\Delta\mu_{\mathrm{Nb}} + 5\Delta\mu_{\mathrm{O}} \end{cases} \tag{4.1}$$

The methodology used to obtain the dependency on the oxygen partial pressure remains identical to the one described in Section 2.4.5. The computed chemical potentials are reported in Table 4.2

Phase	Space Group	Formation energy (eV/atom)	E above CH (eV)
$Nb_{12}O_{29}$	Cmcm, 63	-3.05	0
NbO_2	$I4_1/a$, 88	-2.91	0
Nb	$Im\bar{3}m$, 2	0	0
Ag_2O	$Pn\bar{3}m$, 224	-0.33	0
AgO	Cccm, 66	-0.45	0
Ag	$R\bar{3}m$, 166	0	0
Nb_2O_5	P2, 3	-3.05	0
O_2	C2/m, 12	0	0
Ag_3O_4	$P2_1/c$, 14	-0.41	0
NbO	$Pm\bar{3}m$, 221	-2.29	0
$AgNbO_3$	Pbcm, 57	-2.19	0.038

Table 4.1: Stable phases in the ternary Ag-Nb-O phase diagram reported by the Materials Project Database (PBE).[116,117] The shaded row gives the comparison with $AgNbO_3$, which is unstable with respect to the decomposition in Ag_2O and Nb_2O_5 by 38 meV.

Reservoir	$\Delta\mu_{\mathrm{Ag}}$	$\Delta\mu_{\mathrm{Mn}}$	$\Delta\mu_{\mathrm{Nb}}$	$\Delta\mu_{\mathrm{O}}$
$AgNbO_3$-Ag-Nb_2O_5	0.0	-2.86	-7.4	-1.3

Table 4.2: Values in eV of the chemical potentials of the individual elements for $AgNbO_3$ in contact with Ag and Nb_2O_5.

4.2 Cubic Phase

4.2.1 Computational Details

The methodology used to carry out the density functional theory (DFT) calculations is consistent with the one used for $NaNbO_3$ (Section 3.2.1). The chosen exchange-correlation functional is PBE-GGA.[56] All defect calculations were performed using a 3×3×3 supercell, containing 135 atoms. The plane wave basis set was expanded up to a 500 eV cutoff energy. The Brillouin zone integration was performed using a Γ-centered 6×6×6 k-mesh for unit-cell calculations and a 2×2×2 k-mesh for supercell calculations. The atomic positions were relaxed until the Hellmann-Feynman forces on each atom were below 0.05 eV/Å. Like for NN (Section 3.1.1, Section 3.5), the symmetry was constrained to that of the input space group, as implemented by VASP. The density of states (DOS) were calculated using a Γ-centered 16×16×16 k-mesh.

4.2.2 Electronic Structure

As for sodium niobate (NN), the first step in our methodology is the determination of the relaxed bulk structure and the electronic structure. The computed values of lattice parameters and energy gap are reported and compared with literature in Table 4.3. The band structure and the density of states (DOS) are shown in Figure 4.1.
Contrary to the situation in NN, not only the O p states but also the A-site atom (Ag d) states contribute to the edge of the valence band. As in the NN case, the edge of the conduction band is mainly composed of Nb d states. The valence band maximum (VBM) is in the M point, and the conduction band minimum (CBM) is in the X point, yielding an indirect gap of 1.4 eV. To our knowledge, no experiments have been reported in the literature where the optical band gap as been measured. It is well known that the semi-local nature of the PBE functional tends to underestimate the band gap. However, as discussed in Section 3.2.2, it is not a decisive problem for defect equilibrium calculations, since mostly the curvature of the bands near the band edges, and the relative distance of the thermodynamic charge transition levels to the band edges are decisive for the determination of the defect equilibrium.

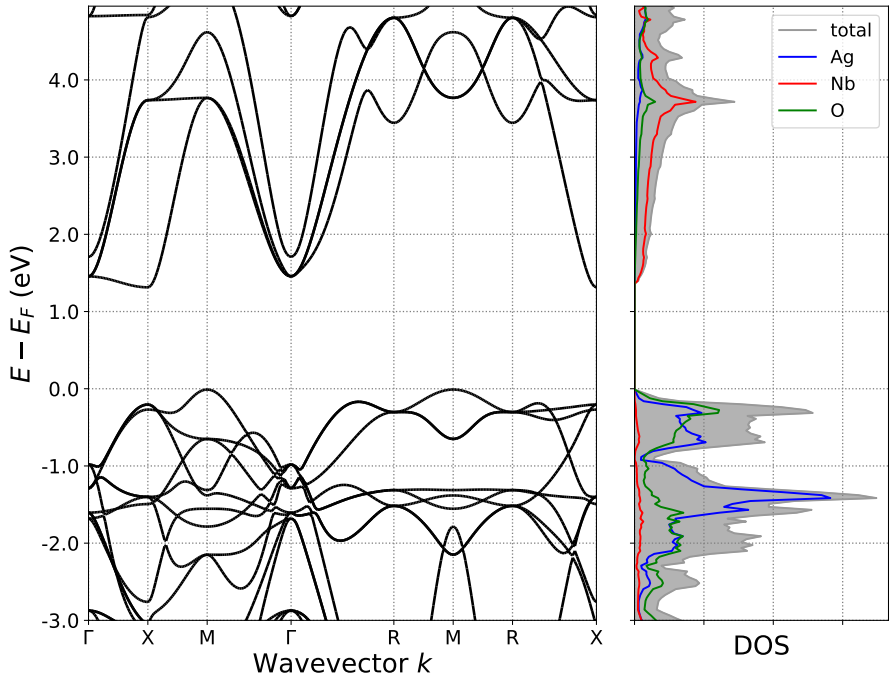

Figure 4.1: Band structure and density of states (DOS) of cubic $AgNbO_3$.

	a(Å)	$E_g^{ind}(eV)$
PBE	4.02	1.40
Ref PBE[130]	3.98	1.51
MP Database (PBE)[116,117]	4.02	1.33
Exp[27]	3.960	

Table 4.3: Values of lattice constant a (Å) and energy gap E_g (eV), calculated with different exchange-correlation functionals and confronted with computational data by Shigemi and Wada,[130] the Materials Project database[116,117] and experimental data.[27]

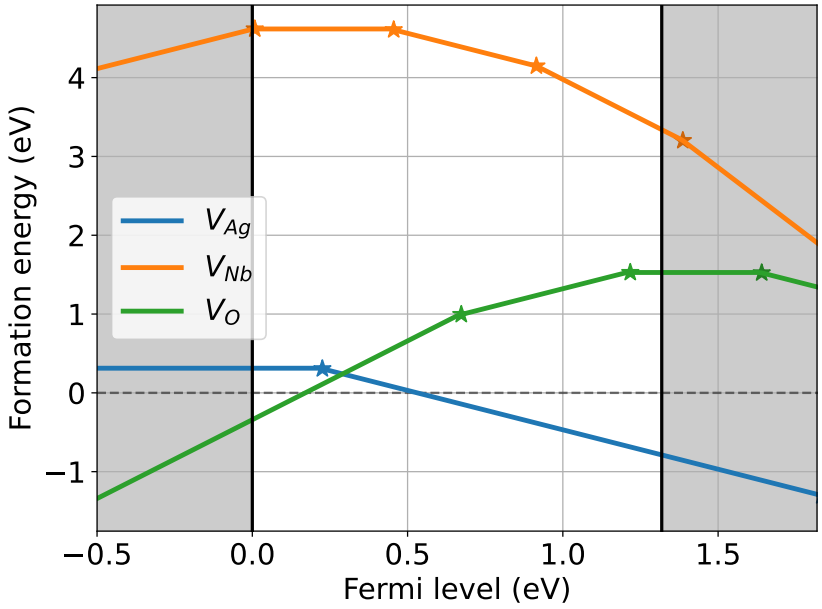

Figure 4.2: Defect formation energies of cubic $AgNbO_3$ as a function of the Fermi level position for thermodynamic conditions representative of the experimental conditions (reported in Table 3.10). The stars on the formation energy curves represent charge transitions.

4.2.3 Formation Energies

The calculated formation energies of Ag, Nb and O vacancies in the thermodynamic conditions reported in Table 4.2, are shown in Figure 4.2. The formation energies, with applied Kumagai charge corrections (Section 2.4.4), have been computed for multiple charge states for Ag vacancies (charge states from -2 to 0), Nb vacancies (from -5 to +1) and O vacancies (from -2 to +2). The charge transition levels are shown in Figure 4.3. The stable charge state of Ag vacancies is -1, as expected from the +1 oxidation state of silver. Nb vacancies present several charge transitions, ranging from +1 to -3. Hence, both defects are acceptor-type. In the case of O vacancies, the most stable charge state across most of the band gap is +2, but with the presence of the deep +2/+1 transition and the shallower +1/0. The sign of the charge indicates that the O vacancies are donor-type defects across most of the gap, as expected. The formation energies of Nb vacancies are

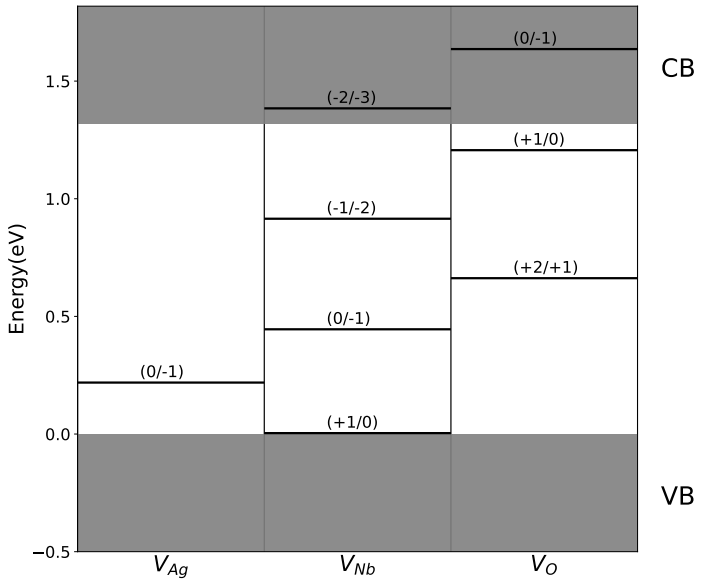

Figure 4.3: Charge transition levels of cubic $AgNbO_3$. The energy levels in the valence band (VB) and the conduction band (CB) are indicated by the grey shaded areas.

larger than the ones of V_{Ag} and V_O. However, the difference in energy is not as prominent as for cubic and orthorhombic $NaNbO_3$, meaning that V_{Nb} could play a role in the compensation mechanisms. This situation is different from what proposed for cubic AN by Moriwake *et al.*[131]

4.3 Orthorhombic Phase

4.3.1 Computational details

Again the methodology for DFT calculations is consistent with the one used for $NaNbO_3$ (Section 3.2.1). The chosen exchange-correlation functional is PBE-GGA.[56] All defect calculations were performed using a $2\times2\times1$ supercell, containing 160 atoms. The plane wave basis set was expanded up to a 550 eV cutoff energy. The Brillouin zone integration was performed using a Γ-centered $4\times4\times2$

k-mesh for unit-cell calculations and a $2\times2\times2$ k-mesh for supercell calculations. The atomic positions were relaxed until the Hellmann-Feynman forces on each atom were below 0.05 eV/Å. The density of states (DOS) were calculated using a Γ-centered $12\times12\times6$ k-mesh.

4.3.2 Electronic Structure

The computed values of lattice parameters and energy gap are reported and compared with literature in Table 4.4. The band structure and the density of states (DOS) are shown in Figure 4.4. While the curvature of the bands is different from the cubic phase (Figure 4.1), the characters of the top of the valence band and the bottom of the conduction band are the same. In fact, the valence band is mainly composed of O p states and Ag d states, while Nb d state constitute the conduction band. The band gap is larger than the one of the cubic phase (Table 4.3). The discussion relative to the band gap and the functional performance is identical as for cubic AN (Section 4.2.2).

	a(Å)	b(Å)	c(Å)	$E_g(eV)$
PBE	5.65	5.75	15.75	1.69
Ref PBE [130]	5.60	5.69	15.60	1.95
MP Database (PBE) [116,117]	5.67	5.75	15.76	1.79
Exp [27]	5.54	5.60	15.56	

Table 4.4: Values of lattice constants a, b, c (Å) and energy gap E_g (eV) of orthorhombic $AgNbO_3$ (space group *Pbcm*, No. 57), computed with the PBE [56] exchange-correlation functional and confronted with computational data by Shigemi and Wada, [121] the Materials Project database [116,117] and experimental data. [27]

4.3.3 Formation Energies

As discussed in Section 1.4, AN shows double *P-E* loops in its natural composition. However, it has been shown that a chemical modification of $AgNbO_3$ with Mn can further reduce the remnant polarization and increase the recoverable energy [39] (Section 1.5). Therefore, in addition to vacancies, we have studied also the case of Mn substitution on both the Ag-site and Nb-site. The calculated formation

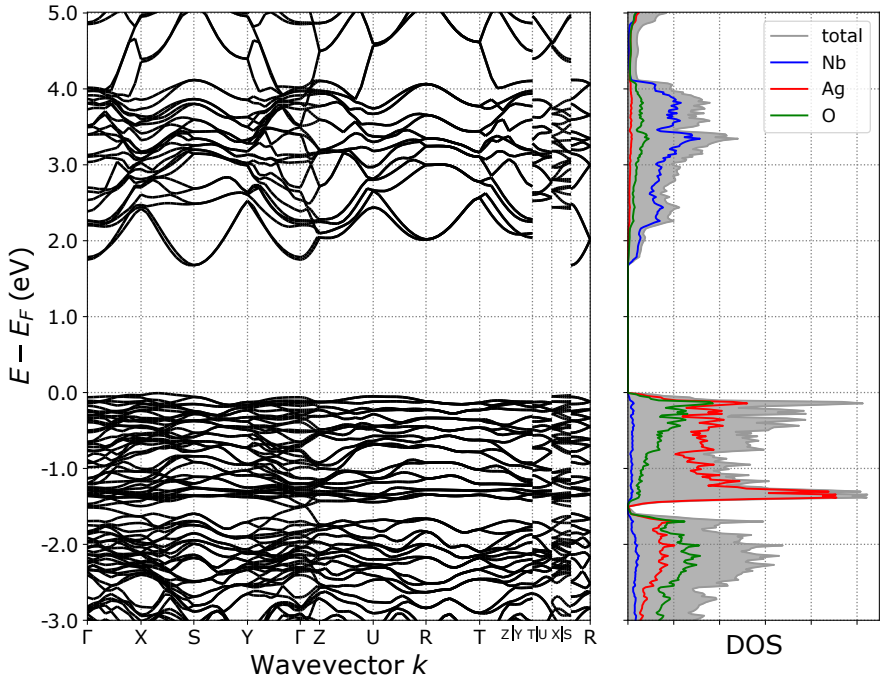

Figure 4.4: Band structure and density of states (DOS) of orthorhombic $AgNbO_3$.

energies of the intrinsic point defects and the Mn-substitutional defect, in the thermodynamic conditions reported in Table 4.2, are shown in Figure 4.5. The charge transition levels are shown in Figure 4.6. The formation energies, with applied Kumagai charge corrections (Section 2.4.4), have been computed for multiple charge states for Ag vacancies (charge states from -2 to 0), Nb vacancies (from -5 to 0) and O vacancies (from -2 to +2). In the case Ag and Nb vacancies, the stable charge states across the band gap are -1 and from -1 to -3, respectively. Hence, both defects are acceptor-type. In the case of O vacancies the most stable charge state across most of the band gap is +2. However, the transition between +2 to 0 state is present at circa 0.5 eV below the conduction band minimum, contrary to the cubic case where the deep transition +2/+1 is followed by a shallow +1/0. The sign of the charge indicates that the O vacancies are donor-type defects across most of the gap, as expected. The formation energies of Nb vacancies are larger than the ones of V_{Ag} and V_O. On the other hand, also for the orthorhombic phase

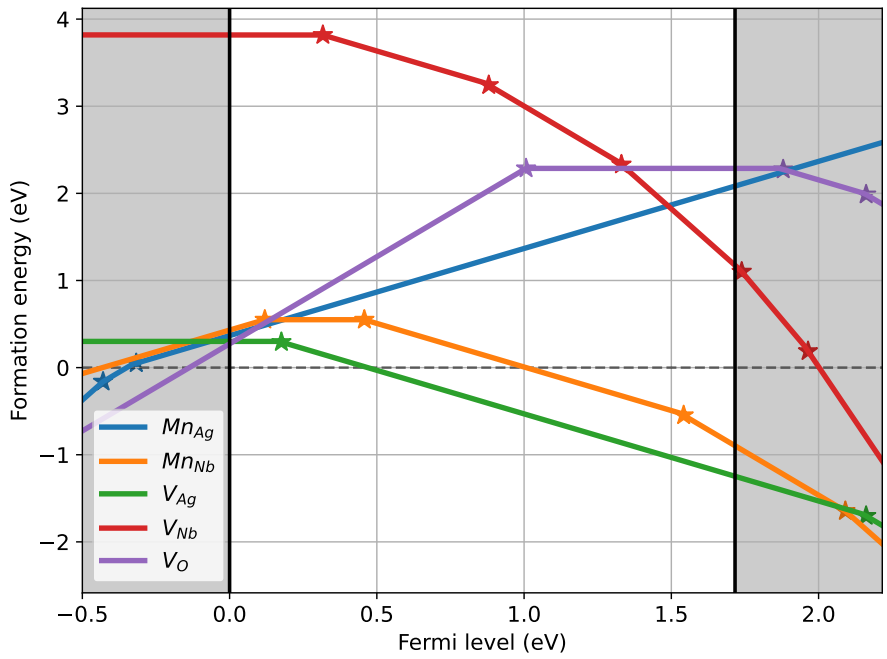

Figure 4.5: Defect formation energies of orthorhombic $AgNbO_3$ as a function of the Fermi level position for thermodynamic conditions representative of the experimental conditions (reported in Table 3.10). The stars on the formation energy curves represent charge transitions.

the difference in energy is not as large as for orthorhombic $NaNbO_3$.
In order to understand how the chemical modification with Mn affects the defect properties of $AgNbO_3$, we have computed the formation energy of the Mn-substitutional defects with the same method applied for the vacancies. In the aforementioned study by Zhao *et al*,[39] it is proposed that the substitution behaviour of Mn into AN is complex. In fact, it is suggested that the Mn-ions can exist in multiple valence states (Mn^{2+}, Mn^{3+}, Mn^{4+}) and that the substitution could be for both Ag^+ on the A-site and Nb^{5+} on the B-site. In order to investigate this complex behaviour of Mn-substitution, we have computed the formation energies of Mn-substitutional defects on both the A-site (Mn_{Ag}) and the B-site (Mn_{Nb}), considering many possible oxidation states of Mn (from +2 to +7). The results are shown in Figure 4.5. The chemical potential for Mn has been calculated by

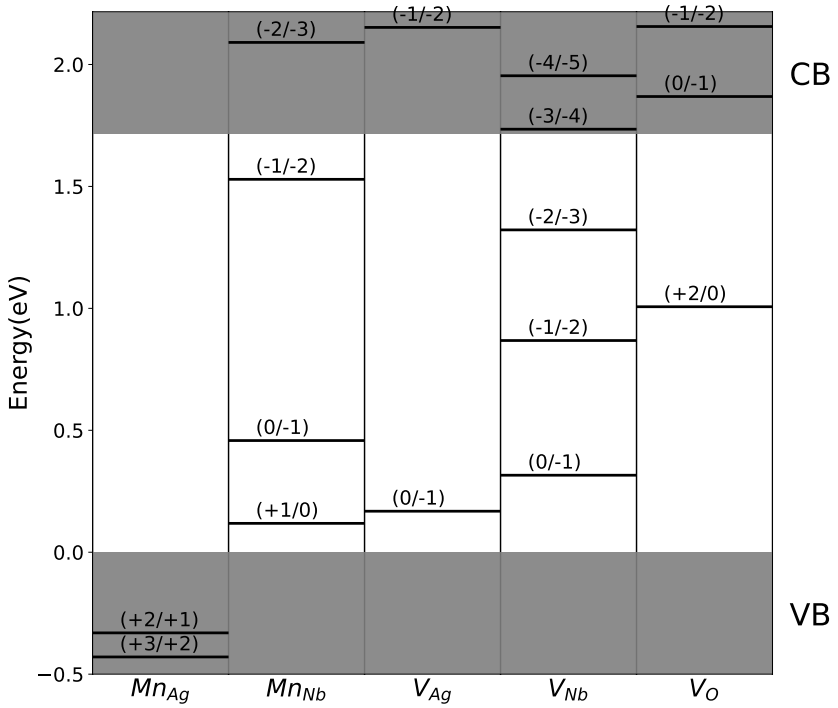

Figure 4.6: Charge transition levels of orthorhombic $AgNbO_3$. The energy levels in the VB and the CB are indicated by the grey shaded areas.

considering the system in contact with MnO_2, to reproduce experimental conditions.[39] Nonetheless it is important to remember that the total concentration of Mn is independent of μ_{Mn}, as it is imposed fixed to the experimental value. The relative concentrations of Mn on the A and B-sites, however, depend on the chemical potentials of Mn, Ag and Nb.

A first observation is that, excluding the region close to the VBM, the formation energies of Mn_{Ag} are larger than for Mn_{Nb} across most of the band gap. A possible explanation for this can be found by looking at the Mn, Ag and Nb ionic radii. The dimensions of Mn^{2+} (0.83 Å), Mn^{3+} (0.65 Å) and Mn^{4+} (0.53 Å) ions are more compatible with Nb^{5+} (0.64 Å), then Ag^{+} (1.28 Å).[39] This is clearly a reasonable but only preliminary explanation, which calls for further investigation on this matter.

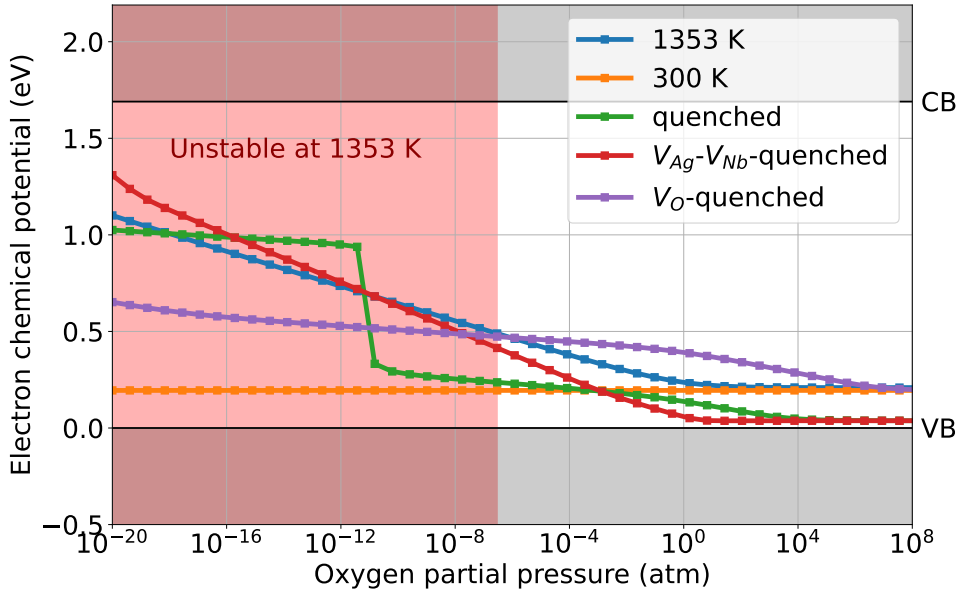

Figure 4.7: Electron chemical potential determined self-consistently in orthorhombic $AgNbO_3$, as a function of the oxygen partial pressure in high temperature (1353 K), room temperature (300 K) and in quenched conditions.

In the case of Mn_{Nb}, the stable charge states are -2,-1,0 and +1, corresponding to the Mn oxidation states of +3,+4,+5 and +6, respectively. This reveals interesting and not yet predicted features of the Mn-substitution in AN, which are to be traced to the multitude of oxidation states which can be attributed to manganese. As shown by the charge transition levels in Figure 4.6, the acceptor behaviour of the Mn^{3+} is in competition with the donor behaviour of Mn^{6+}. Therefore, the position of the electron chemical potential dictates if Mn_{Nb} is a donor or an acceptor. On the other hand, the case of Mn_{Ag} is much simpler, where the charge state +1 is stable across all the band gap. This charge state corresponds to the Mn oxidation state of +2.

4.3.4 Dependency on Oxygen Partial Pressure

The next step in our analysis is the solution of the charge neutrality condition for different oxygen partial pressure, in order to compute the Brouwer diagrams

(Section 2.4.7). We have computed defect concentrations at the sintering temperature (1353 K)[25] and room temperature. The results are shown in Figure 4.8. As for $NaNbO_3$, we have evaluated the electron chemical potential (μ_e) for both equilibrated and quenched conditions, and the results are shown in Figure 4.7.
The first observation is that, at sintering temperature, the material is unstable for oxygen partial pressure (p_{O_2}) lower than $0.5 \cdot 10^{-6}$ atm, as highlighted by the red region in Figure 4.8a. In fact, the concentration of Ag vacancies is greater than the concentration of available sites, which is clearly unphysical and indicates the instability of the material in this p_{O_2} region. This finding is compatible with the experimental observations. In recent years, several works have reported that the reaction to form AN is not possible in low p_{O_2} conditions.[25,26,132] Moreover, it has been revealed that, after synthesis, the material tends to be non-stochiometric due to Ag deficiency,[26] which was confirmed by our experimental colleagues (the manuscript is currently still in preparation), and validates the low V_{Ag} formation energy in our data (Figure 4.5). With increasing p_{O_2} we get in the stable region, where the concentration of V_{Ag} and V_O decreases.
The second consideration is that the preferred lattice site for Mn substitution is p_{O_2}- dependent at high temperatures. In fact, while for low p_{O_2} Mn sits mostly on the Ag site, the balance changes for increasing p_{O_2}, until Mn is found mostly on the Nb site for high p_{O_2}. The crossover point where $[Mn_{Nb}]$ exceeds $[Mn_{Ag}]$ is located at 10 atm circa. It is useful to remember that the total concentration of Mn atoms has been fixed to the experimental value of 0.3% wt, but its distribution on the different lattice sites still depends on T and μ_e (Section 2.4.8). Because of the dominance of Ag vacancies, the resulting behaviour is p-type, as shown in Figure 4.7. At low temperature (Figure 4.8b) the situation does not show an important dependency on p_{O_2}, with V_{Ag} and Mn_{Nb} dominating over the entire range, which gives a constant μ_e close to the VBM. The balance can be shifted when defects are quenched from the high temperature phase into the low temperature one. When all defects are quenched, the dominating Ag vacancies push μ_e very close to the VBM (green line in Figure 4.7). When only V_{Ag} and V_{Nb} are quenched (red line), with V_O free to equilibrate, the behaviour at high p_{O_2} is equivalent to the quenched case, but the free O vacancies yield a similar μ_e-dependency to the high temperature case. On the other hand, when only V_O are quenched (violet line), μ_e at ambient pressure moves further away from the VBM, following a slope similar to the quenched case, while at high p_{O_2} the electron chemical potential is equivalent to the equilibrated one at high and low temperatures.
The last, and arguably most important, observation is that, in the case of $AgNbO_3$, the quenching conditions have smaller impact on the final position of the elec-

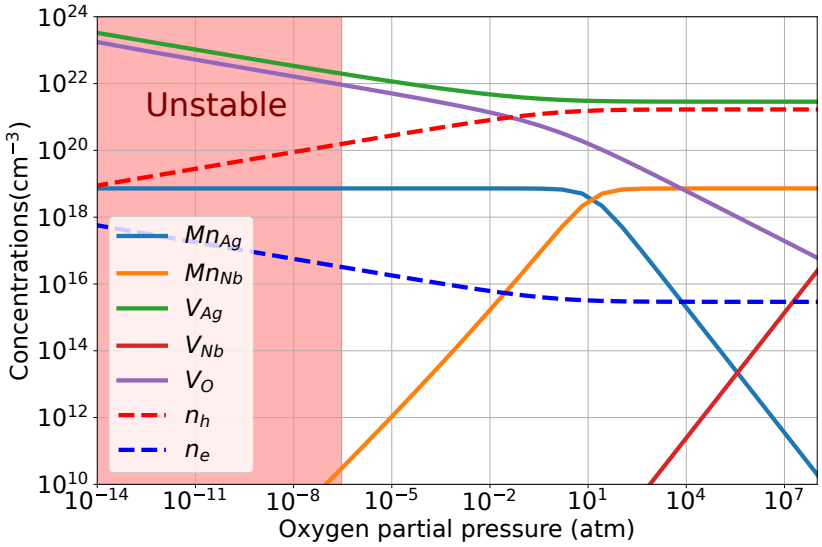

(a) T = 1353 K

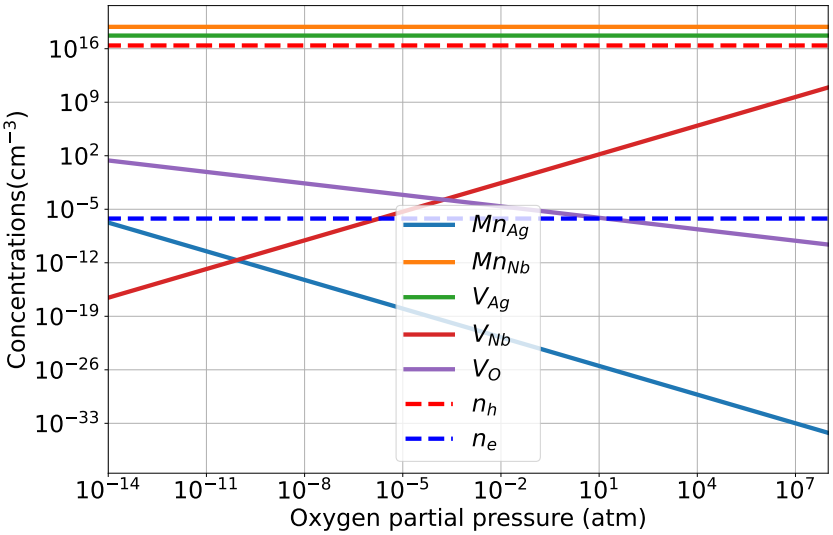

(b) T = 300 K

Figure 4.8: Concentrations of defects, electrons (n_e) and holes (n_h) in orthorhombic $AgNbO_3$, as a function of the oxygen partial pressure in high temperature (**a**) and room temperature (**b**) conditions.

tron chemical potential than for NN. In fact, while for $NaNbO_3$ the quenching conditions could determine whether the material was n-type or p-type, in the case of silver niobate, μ_e is always closer to the VBM. The semiconductor is thus p-type for all quenching conditions, which influence only the distance from μ_e to the VBM. The motivation behind this difference is to be attributed to the aforementioned low formation energies of Ag vacancies, which are acceptors and yield a p-type behaviour.

4.4 Conclusion

In pure silver niobate, Ag vacancies and O vacancies regulate the defect equilibrium. V_{Ag} are acceptors with charge state -1 and neutral if the Fermi level is near the VBM. V_O are donors in charge state +2 with a deep transition level to the neutral state. Like for $NaNbO_3$, V_{Nb} shows charge states from -5 to neutral with scattered transition levels. The formation energies of V_{Ag} are particularly low. As a consequence, V_{Ag} is the dominating defect over the whole oxygen partial pressure (p_{O_2}) range. Moreover, at low oxygen partial pressure (p_{O_2} < 10^{-6} atm) and high temperature, the material is unstable due to the unphysically large V_{Ag} concentrations, which is in line with the experimental observations that AN tends to be Ag deficient and cannot be synthesized in low p_{O_2}.[25,26,132] When Mn is introduced into the system, it can occupy both the Ag- and Nb-site. Mn_{Ag} is a single-charged donor, while Mn_{Nb} can be a donor or an acceptor based on the Fermi level position. It is a single-charged donor only when the Fermi level is close to the VBM, otherwise is either neutral or an acceptor. At high temperature and low p_{O_2}, Mn is found on the Ag-site, while, for p_{O_2} larger than 10 atm, Mn is stable on the Nb-site. At room temperature, Mn is found only on the Nb-site.
The considerations, regarding the limitations of the computational model and the problems in the comparison with the experiment, we have expressed for $NaNbO_3$ are true also for $AgNbO_3$, and can be found in Section 3.7. In the case of AN, the A-site deficiency and instability of the material are even more concerning problems than for NN, and agree with our computational findings that AN is metastable and only stabilzed kinetically, and that the material is unstable at sintering temperature and low p_{O_2} pressure due to Ag-deficiency (negative V_{Ag} formation energies).

5 Summary and outlook

5.1 Summary

Antiferroelectric materials provide a solution to increase the energy density in capacitors, while preserving a high efficiency. $NaNbO_3$ (NN) and $AgNbO_3$ (AN) are two of the most promising lead-free candidates to replace toxic lead-based compunds already on the market.[2,14] Chemical modification has been used extensively to improve their antiferroelectric properties, specifically to lower their remnant polarization.[23,39] In this work, we have therefore investigated, with density functional theory, how doping and synthesis conditions modify the electronic properties of NN and AN, with focus on the Fermi level. In particular, we have determined the thermodynamic defect equilibrium by solving the charge neutrality condition, accounting for the impact of extrisic defects on the compensation mechanisms. Moreover, we have developed a novel scheme to account for quenching of defects within the established point defect thermodynamics. Additionally, we have determined with the nudged elastic band (NEB) method the diffusion barriers of vacancies in NN. Through this effort, we have addressed the questions reported in Section 1.9:

- ***Which defects are forming in these materials?***
  - **$NaNbO_3$**: Na and O vacancies show low formation energies in all phases and all thermodynamic conditions. Nb vacancies display much higher formation energies. This translates in high V_{Na} and V_O concentrations. V_{Na} are mostly acceptors with charge state -1, and neutral if the Fermi level is near the valence band maximum (VBM), while V_O are donors in charge state +2 and +1, and neutral near the conduction band minimum (CBM). V_{Nb} display a wider variaty of charge states, ranging from -5 to neutral. Therefore, the dominating compensation mechanism involves V_{Na} and V_O, and which species is dominating

depends on the oxygen partial pressure (p_{O_2}). Moreover, defect associates formed by Na and O vacancies in their charged states are found to be stable, both as a triple neutral complex (V_{Na}-V_O-V_{Na}) and donor (charge +1) double complex (V_{Na}-V_O). The dopants Sr and Sn are introduced on the Na- and Nb-site, respectively. Sr_{Na} is mostly a single-charged donor, and neutral near the CBM. Sn_{Nb} is a single-charged acceptor, while neutral near the VBM. When in contact with a reservoir of $SrSnO_3$, extrinsic defects show low formation energies, in the same range of V_{Na} and V_O, which justifies how it is experimentally possible to incorporate $SrSnO_3$ in NN up to 5 %wt, before phase segregation occurs. Extrinsic defects introduce new stable defect complexes. In fact, the neutral complex Sr_{Na}-V_{Na} and the single-charged donor complex Sr_{Nb}-V_O show negative binding energies.

- **$AgNbO_3$**: Ag vacancies show extremely low formation energies. V_{Ag} are acceptors with charge state -1 and neutral if the Fermi level is near the VBM. V_O are donors in charge state +2 with a deep transition level to the neutral state. Like for $NaNbO_3$, V_{Nb} shows charge states from -5 to neutral with scattered transition levels. The main compensation mechanism concerns V_{Ag} and V_O, with V_{Ag} dominating over the whole p_{O_2} range. Moreover, at high temperature and low oxygen partial pressure (p_{O_2} < 10^{-6} atm), the material is unstable due to the unphysically large V_{Ag} concentrations, which is in line with the experimental observations that AN tends to be Ag deficient and cannot be synthesized in low p_{O_2}.[25,26,132] Doping with Mn was studied on the Ag-site and Nb-site. Manganese can be found in both sites. Mn_{Ag} is a single-charged donor, while Mn_{Nb} can be a donor or an acceptor based on the Fermi level position. It is a single-charged donor only when the Fermi level is close to the VBM, otherwise is either neutral or an acceptor. At high temperature and low p_{O_2}, Mn is found on the Ag-site, while, for p_{O_2} > 10 atm, Mn is stable on the Nb-site. At room temperature, Mn is found only on the Nb-site.

- ***Where is the Fermi level? What is the influence of doping conditions?***

  - **$NaNbO_3$**: At high temperature and low p_{O_2}, the doped material is a n-type semiconductor, while for high p_{O_2} the system becomes p-type. In fact, the Fermi level decreases almost linearly with p_{O_2}, from the edge of the CBM to a distance of approximately 1 eV to the VBM. At room

temperature, the material is p-type over the whole p_{O_2} range, with the Fermi level ranging approximately from 1 eV to 0.5 eV above the VBM. When all defects are quenched, the frozen donor species dominate, and the Fermi level shifts towards the CBM. The same situation happens when only O vacancies are quenched. Quenching only Na and Nb vacancies produces a less pronounced shift towards the VBM. Since V_O shows a diffusion barrier of only 0.3 eV, while the barrier of V_{Na} is much larger (1.4 eV), it is more likely that experimentally V_{Na} are frozen from the high temperature regime, while V_O can reach thermodynamic equilibrium.

- **$AgNbO_3$**: The Fermi level in Mn-doped AN is always close to the VBM, both at high and room temperature and for all quenching conditions, meaning the material is always a p-type semiconductor. This is due to the dominating Ag vacancies, which are single-charged acceptors. At high temperature, V_{Ag} are partially compensated by O vacancies, while at room temperature the compensation mechanism involves Mn_{Nb}, which acts as donor. In contrast to NN, different quenching conditions modify only slightly the slope of the Fermi level dependency on p_{O_2}, without having a significant impact on the overall behaviour of the semiconductor.

- ***What role do defects associates play in the AFE properties?***

  - We have investigated the presence of defect complexes in $NaNbO_3$. We have found that several associates between defects on the Na-, Nb- and O-sites show negative binding energies, and are present in large concentrations. Because they are formed by charged defects, they introduce dipoles into the system, which can interact with the spontaneous FE/AFE displacements and with an external field. Since the zero-field RT-stable phase of NN is antiferroelectric, there is no preferencial orientation for the dipoles, hence they assume a random distribution of orientations. Therefore, like already proposed for FE materials,[11,36] we posit that defect dipoles introduce a restoring force which enhances the reversibility of the FE-AFE phase transition, thus reducing the remnant polarization in AFE materials, which improves the quality of double *P-E* loops.

5.2 Outlook

Despite the achievements of this doctoral work, there still remain unresolved scientific problems, theories to be further investigated, and methods to be extended and improved. We sort our thoughts into three different groups. Firstly, we address the impact of lattice instability on the defect formation energies within density functional theory (DFT). Secondly, we explore the shortcomings of the thermodynamics of point defects employed in this work. Lastly, we discuss the possible future research, to better understand the correlation between doping and antiferroelectric properties.

Lattice instability and formation energies

In this work, we have only scratched the surface on the fact that, when performing total energy defect calculations, structural instability at 0 K with might introduce additional relaxation mechanisms, leading to an energy gain which would not be present at finite-temperature. To our knowledge, this topic has not been addressed yet in the literature. In this thesis, we presented only a preliminary analysis on the connection between phase hierarchy and formation energies. In order to find a descriptor for this phenomenon, and possibly introduce corrections, a more systematical and detailed analysis is necessary. Particularly, it would be interesting to study the influence of the phase on the relaxation volumes and atomic displacements of charged defects. Moreover, the impact of the exchange-correlation functional and charge localization on the relaxation is another aspect that should be considered. Lastly, it should be explored whether the defect charge transition levels are modified and, if the answer is yes, whether it is possible to find a descriptor.

Point defects: from the dilute limit to phase formation

The established point defects thermodynamics[69–71] used in this work is valid only for ideal solutions. In other words, it relies on the fundamental assumption that the number of point defects is much smaller than the number of available sites, so that defects do not interact with each other. This assumption is unfortunately not always true. In fact, in the field of ferroelectric/antiferroelectrics, more often than not, chemical modification is much closer to creating solid solutions rather than doping, meaning the concentration of extrinsic defects are much closer to parts per hundred rather than parts per milion. In such a context, if the interaction

between defects is not negligible, the current point defect formalism might fail. Therefore, future work could be invested in developing a formalism to describe the crossover from the dilute limit to hyperdoping and phase formation. In particular, such an approach would combine DFT supercell calculations with cluster expansion methods, which would allow to treat effectively solid solutions of defects. Moreover, the formalism needs to include the dependency of the cluster expansion on the Fermi level, such that the thermodynamics of defect equilirbium is properly captured.

Tayloring antiferroelectric properties via doping

During this doctoral thesis we have made significant progress in understanding the connection between doping (and its impact on the Fermi level) and the properties of antiferroelectric materials. However, the story is far from being complete. In fact, a method to determine *a priori* if a material will display antiferroelectric distortions is still missing. One way to achieve this is to look at the phonon spectra of the cubic perovskite parent phase, checking if the unstable modes corrispond to antiferroelectric distortions. This method is not only computationally expensive, but also fails to provide a theory on the origin of antiferroelectricity. As a matter of fact, if we approach the proplem with first-order perturbation theory, the answer on the nature of the distortions hides in the band structure of the parent phase. Unfortunately, such a clear, universal descriptor is still missing. Its discovery would allow to systematically search with cheap computational methods for new compositions of promosing antiferroelectric materials, like $NaNbO_3$ and $AgNbO_3$. Once the compositions are identified, the same approach used in this doctoral thesis can be used to identify which doping and synthesis conditions might be used to further improve the antiferroelectric properties, with the ultimate goal to create usable materials in commercially available devices.

Curriculum Vitæ

Research Experience

since 2019 — Scientific staff member (*Wissenschaftlicher Mitarbeiter*)
Materials Modelling group
Prof. Dr. rer. nat. Karsten Albe,
Technische Universität Darmstadt, Germany
LOEWE project "FLAME" - "*Fermi Level Engineering of Antiferroelectric Materials for Energy Storage and Insulation Systems*"

Education

2016 - 2019 — Master of Science in Materials Science
Università degli Studi di Milano-Bicocca, Italy

2017 - 2018 — Erasmus$^+$ semester
Technische Universität Darmstadt, Germany

2013 - 2016 — Bachelor of Science in Materials Science
Università degli Studi di Milano-Bicocca, Italy

Peer Reviewed Articles

L. Villa, E. Ghorbani, and K. Albe, *Role of intrinsic defects in cubic $NaNbO_3$: A computational study based on hybrid density-functional theory*, Journal of Applied Physics 131, 124106 (2022)

E. Ghorbani, L. Villa, P. Erhart, A. Klein, and K. Albe, *Self-consistent calculations of charge self-trapping energies: A comparative study of polaron formation and migration in $PbTiO_3$*, Physical Review Materials 6, 074410 (2022), Publisher: American Physical Society

L. Villa and K. Albe, *Role of doping and defect quenching in antiferroelectric $NaNbO_3$ from first principles*, Physical Review B 106, 134101 (2022), Publisher: American Physical Society

M.-H. Zhang, H. Ding, S. Egert, C. Zhao, L. Villa, L. Fulanović, P. B. Groszewicz, G. Buntkowsky, H.-J. Kleebe, K. Albe, A. Klein, and J. Koruza, *Tailoring high-energy storage $NaNbO_3$-based materials from antiferroelectric to relaxor states*, Nature Communications 14, 1525 (2023), Number: 1 Publisher: Nature Publishing Group

Oral Presentations at International Conferences

09/2022, MSE Congress, Darmstadt, Germany, '*Quenched defect thermodynamics in $SrSnO_3$-doped $NaNbO_3$*', L. Villa, K. Albe

06/2022, ISAF-PFM-ECAPD Joint Conference, Tour, France, '*Quenched defect thermodynamics in $SrSnO_3$-doped $NaNbO_3$*', L. Villa, K. Albe

01/2022, EMA, Online Conference, '*Intrinsic point defects in Sodium Niobate studied with hybrid density-functional theory.*', L. Villa, E. Ghorbani, K. Albe

08/2020, Electroceramics XVII, Online Conference, '*Intrinsic point defects in Sodium Niobate studied with hybrid density-functional theory.*', L. Villa, E. Ghorbani, K. Albe

03/2020 (cancelled), DPG-Frühjahrstagung, Regensburg, Germany, '*First principles calculation on intrinsic defects properties of Sodium Niobate*', L. Villa, E. Ghorbani, K. Albe

Bibliography

[1] L. Yang, X. Kong, F. Li, H. Hao, Z. Cheng, H. Liu, J.-F. Li, and S. Zhang, *Perovskite lead-free dielectrics for energy storage applications*, Progress in Materials Science 102, 72–108 (2019).

[2] Z. Liu, T. Lu, J. Ye, G. Wang, X. Dong, R. Withers, and Y. Liu, *Antiferroelectrics for Energy Storage Applications: a Review*, Advanced Materials Technologies 3, 1800111 (2018).

[3] M. S. Whittingham, *Materials Challenges Facing Electrical Energy Storage*, MRS Bulletin 33, 411–419 (2008), Publisher: Cambridge University Press.

[4] A. J. Moulson and J. M. Herbert, *Electroceramics: Materials, Properties, Applications*, 2nd edition ed., Wiley, June 2003.

[5] *Physics of Ferroelectrics: A Modern Perspective*, Topics in Applied Physics, vol. 105, Springer, Berlin, Heidelberg, 2007.

[6] J. Schröder and D. C. Lupascu (eds.), *Ferroic Functional Materials*, CISM International Centre for Mechanical Sciences, vol. 581, Springer International Publishing, Cham, 2018.

[7] C. Kittel, *Theory of Antiferroelectric Crystals*, Physical Review 82, 729–732 (1951), Publisher: American Physical Society.

[8] X. Hao, J. Zhai, L. B. Kong, and Z. Xu, *A comprehensive review on the progress of lead zirconate-based antiferroelectric materials*, Progress in Materials Science 63, 1–57 (2014), Publisher: Pergamon Press.

[9] K. M. Rabe, *Antiferroelectricity in Oxides: A Reexamination*, Functional Metal Oxides, John Wiley & Sons, Ltd, 2013, Section: 7 _eprint: https://onlinelibrary.wiley.com/doi/pdf/10.1002/9783527654864.ch7, pp. 221–244.

[10] G. Shirane, *Ferroelectricity and Antiferroelectricity in Ceramic PbZr$_{\textrm{3}}$ Containing Ba or Sr*, Physical Review 86, 219–227 (1952), Publisher: American Physical Society.

[11] J. Hao, Z. Xu, R. Chu, W. Li, J. Du, P. Fu, and G. Li, *Electric Field Cycling Induced Large Electrostrain in Aged (K0.5Na0.5)NbO3–Cu Lead-Free Piezoelectric Ceramics*, Journal of the American Ceramic Society 99, 402–405 (2016), _eprint: https://onlinelibrary.wiley.com/doi/pdf/10.1111/jace.14067.

[12] G. L. Yuan, Y. Yang, and S. W. Or, *Aging-induced double ferroelectric hysteresis loops in BiFeO3 multiferroic ceramic*, Applied Physics Letters 91, 122907 (2007), Publisher: American Institute of Physics.

[13] R. J. D. Tilley, *Perovskites: Structure-Property Relationships*, 1st edition ed., Wiley, Chichester, West Sussex, United Kingdom, May 2016.

[14] C. A. Randall, Z. Fan, I. Reaney, L.-Q. Chen, and S. Trolier-McKinstry, *Antiferroelectrics: History, fundamentals, crystal chemistry, crystal structures, size effects, and applications*, Journal of the American Ceramic Society 104, 3775–3810 (2021), _eprint: https://ceramics.onlinelibrary.wiley.com/doi/pdf/10.1111/jace.17834.

[15] World Health Organization (WHO), *Lead Poisoning and Health*, https://www.who.int/news-room/fact-sheets/detail/lead-poisoning-and-health.

[16] D. Yang, J. Gao, L. Shu, Y.-X. Liu, J. Yu, Y. Zhang, X. Wang, B.-P. Zhang, and J.-F. Li, *Lead-free antiferroelectric niobates $AgNbO_3$ and $NaNbO_3$ for energy storage applications*, Journal of Materials Chemistry A 8, 23724–23737 (2020).

[17] J. Koruza, J. Tellier, V. Bobnar, and M. Kosec, *Phase transitions of sodium niobate powder and ceramics, prepared by solid state synthesis*, J. Appl. Phys. 108, 10 (2010).

[18] D. Fritsch, *Electronic and Optical Properties of Sodium Niobate: A Density Functional Theory Study*, Advances in Materials Science and Engineering, 6416057 (2018).

[19] H. D. Megaw, *The seven phases of sodium niobate*, Ferroelectrics 7, 87–89 (1974).

[20] R. Machado, M. Sepliarsky, and M. G. Stachiotti, *Relative phase stability and lattice dynamics of NaNbO 3 from first-principles calculations*, Physical Review B 84, 134107 (2011).

[21] L. Jiang, D. C. Mitchell, W. Dmowski, and T. Egami, *Local structure of NaNbO 3 : A neutron scattering study*, Physical Review B 88, 014105 (2013).

[22] H. Guo, H. Shimizu, Y. Mizuno, and C. A. Randall, *Domain configuration changes under electric field-induced antiferroelectric-ferroelectric phase transitions in $NaNbO_3$ -based ceramics*, Journal of Applied Physics 118, 054102 (2015).

[23] M.-H. Zhang, N. Hadaeghi, S. Egert, H. Ding, H. Zhang, P. B. Groszewicz, G. Buntkowsky, A. Klein, and J. Koruza, *Design of Lead-Free Antiferroelectric $(1-x)NaNbO_3-xSrSnO_3$ Compositions Guided by First-Principles Calculations*, Chemistry of Materials 33, 266–274 (2021).

[24] M. Valant, A.-K. Axelsson, and N. Alford, *Review of Ag(Nb, Ta)O3 as a functional material*, Journal of the European Ceramic Society 27, 2549–2560 (2007).

[25] M.-H. Zhang, L. Carstensen, C. Zhao, L. Fulanović, W. Donner, and J. Koruza, *Revealing the solid-state processing mechanisms of antiferroelectric AgNbO3 for energy storage*, Journal of the American Ceramic Society 105, 451–460 (2022), _eprint: https://onlinelibrary.wiley.com/doi/pdf/10.1111/jace.18091.

[26] A. Kania, A. Niewiadomski, S. Miga, I. Jankowska-Sumara, M. Pawlik, Z. Ujma, J. Koperski, and J. Suchanicz, *Silver deficiency and excess effects on quality, dielectric properties and phase transitions of AgNbO3 ceramics*, Journal of the European Ceramic Society 34, 1761–1770 (2014).

[27] P. Sciau, A. Kania, B. Dkhil, E. Suard, and A. Ratuszna, *Structural investigation of $AgNbO_3$ phases using x-ray and neutron diffraction*, Journal of Physics: Condensed Matter 16, 2795–2810 (2004).

[28] I. Levin, V. Krayzman, J. C. Woicik, J. Karapetrova, T. Proffen, M. G. Tucker, and I. M. Reaney, *Structural changes underlying the diffuse dielectric response in AgNbO 3*, Physical Review B 79, 104113 (2009).

[29] M. K. Niranjan and S. Asthana, *First principles study of lead free piezoelectric AgNbO3 and (Ag1-xKx)NbO3 solid solutions*, Solid State Communications 152, 1707–1710 (2012).

[30] H. Shimizu, H. Guo, S. E. Reyes-Lillo, Y. Mizuno, K. M. Rabe, and C. A. Randall, *Lead-free antiferroelectric: xCaZrO3-(1-x)NaNbO3 system*, Dalton Transactions 44, 10763–10772 (2015), Publisher: The Royal Society of Chemistry.

[31] V. M. Goldschmidt, *Die Gesetze der Krystallochemie*, Naturwissenschaften 14, 477–485 (1926).

[32] P. M. Woodward, *Octahedral Tilting in Perovskites. II. Structure Stabilizing Forces*, Acta Crystallographica Section B 53, 44–66 (1997), _eprint: https://onlinelibrary.wiley.com/doi/pdf/10.1107/S0108768196012050.

[33] M. Kunz and I. D. Brown, *Out-of-Center Distortions around Octahedrally Coordinated d0 Transition Metals*, Journal of Solid State Chemistry 115, 395–406 (1995).

[34] C. A. Randall, A. S. Bhalla, T. R. Shrout, and L. E. Cross, *Classification and consequences of complex lead perovskite ferroelectrics with regard to B-site cation order*, Journal of Materials Research 5, 829–834 (1990).

[35] K. K. N. Simon M. Sze, *Physics of Semiconductor Devices*, 1 ed., John Wiley & Sons, Ltd, 2006, _eprint: https://onlinelibrary.wiley.com/doi/pdf/10.1002/0470068329.

[36] D. Lin, K. W. Kwok, and H. L. W. Chan, *Double hysteresis loop in Cu-doped K0.5Na0.5NbO3 lead-free piezoelectric ceramics*, Applied Physics Letters 90, 232903 (2007).

[37] G. Arlt and H. Neumann, *Internal bias in ferroelectric ceramics: Origin and time dependence*, Ferroelectrics 87, 109–120 (1988), Publisher: Taylor & Francis _eprint: https://doi.org/10.1080/00150198808201374.

[38] R. A. Maier, T. A. Pomorski, P. M. Lenahan, and C. A. Randall, *Acceptor-oxygen vacancy defect dipoles and fully coordinated defect centers in a ferroelectric perovskite lattice: Electron paramagnetic resonance analysis of Mn2+ in single crystal BaTiO3*, Journal of Applied Physics 118, 164102 (2015), Publisher: American Institute of Physics.

[39] L. Zhao, Q. Liu, S. Zhang, and J.-F. Li, *Lead-free AgNbO3 anti-ferroelectric ceramics with an enhanced energy storage performance using MnO2 modification*, Journal of Materials Chemistry C 4, 8380–8384 (2016).

[40] Y. Feng, J. Wu, Q. Chi, W. Li, Y. Yu, and W. Fei, *Defects and Aliovalent Doping Engineering in Electroceramics*, Chemical Reviews, acs.chemrev.9b00507 (2020).

[41] L. Gao, H. Guo, S. Zhang, and C. A. Randall, *Stabilized antiferroelectricity in xBiScO$_3$-(1-x)NaNbO $_3$ lead-free ceramics with established double hysteresis loops*, Applied Physics Letters 112, 092905 (2018).

[42] H. Guo, H. Shimizu, Y. Mizuno, and C. A. Randall, *Strategy for stabilization of the antiferroelectric phase (Pbma) over the metastable ferroelectric phase (P2 $_1$ ma) to establish double loop hysteresis in lead-free (1x)NaNbO $_3$ - x SrZrO $_3$ solid solution*, Journal of Applied Physics 117, 214103 (2015).

[43] L. Gao, H. Guo, S. Zhang, and C. A. Randall, *A perovskite lead-free antiferroelectric xCaHfO $_3$ -(1-x) NaNbO $_3$ with induced double hysteresis loops at room temperature*, Journal of Applied Physics 120, 204102 (2016).

[44] J. Ye, G. Wang, X. Chen, F. Cao, and X. Dong, *Enhanced antiferroelectricity and double hysteresis loop observed in lead-free (1-x)NaNbO $_3$ -xCaSnO $_3$ ceramics*, Applied Physics Letters 114, 122901 (2019).

[45] L. Zhao, J. Gao, Q. Liu, S. Zhang, and J.-F. Li, *Silver Niobate Lead-Free Antiferroelectric Ceramics: Enhancing Energy Storage Density by B-Site Doping*, ACS Applied Materials & Interfaces 10, 819–826 (2018).

[46] X. Hu, M. Valant, and D. Suvorov, *Phase transitions and dielectric properties of the Ag1-xBix/3NbO3 system*, Journal of Applied Physics 99, 124109 (2006), Publisher: American Institute of Physics.

[47] P. Hohenberg and W. Kohn, *Inhomogeneous Electron Gas*, Physical Review 136, B864–B871 (1964), Publisher: American Physical Society.

[48] W. Kohn and L. J. Sham, *Self-Consistent Equations Including Exchange and Correlation Effects*, Physical Review 140, A1133–A1138 (1965), Publisher: American Physical Society.

[49] R. M. Martin, *Electronic Structure: Basic Theory and Practical Methods*, Cambridge University Press, Cambridge, 2004.

[50] N. W. Ashcroft and N. D. Mermin, *Solid State Physics*, 1st edition ed., Cengage Learning, New York, January 1976.

[51] D. R. Hamann, M. Schlüter, and C. Chiang, *Norm-Conserving Pseudopotentials*, Physical Review Letters 43, 1494–1497 (1979), Publisher: American Physical Society.

[52] D. Vanderbilt, *Soft self-consistent pseudopotentials in a generalized eigenvalue formalism*, Physical Review B 41, 7892–7895 (1990), Publisher: American Physical Society.

[53] P. E. Blöchl, *Projector augmented-wave method*, Physical Review B 50, 17953–17979 (1994).

[54] *Introduction to the LAPW Method*, Planewaves, Pseudopotentials and the LAPW Method (D. J. Singh and L. Nordström, eds.), Springer US, Boston, MA, 2006, pp. 43–52.

[55] D. M. Ceperley and B. J. Alder, *Ground State of the Electron Gas by a Stochastic Method*, Physical Review Letters 45, 566–569 (1980), Publisher: American Physical Society.

[56] J. P. Perdew, K. Burke, and M. Ernzerhof, *Generalized Gradient Approximation Made Simple*, Physical Review Letters 77, 3865–3868 (1996).

[57] J. P. Perdew, R. G. Parr, M. Levy, and J. L. Balduz, *Density-Functional Theory for Fractional Particle Number: Derivative Discontinuities of the Energy*, Physical Review Letters 49, 1691–1694 (1982).

[58] I. Dabo, A. Ferretti, N. Poilvert, Y. Li, N. Marzari, and M. Cococcioni, *Koopmans' condition for density-functional theory*, Physical Review B 82, 115121 (2010).

[59] S. Lany and A. Zunger, *Polaronic hole localization and multiple hole binding of acceptors in oxide wide-gap semiconductors*, Phys. Rev. B 80, 085202 (2009), Publisher: American Physical Society.

[60] A. D. Becke, *Density-functional thermochemistry. III. The role of exact exchange*, The Journal of Chemical Physics 98, 5648–5652 (1993), Publisher: American Institute of Physics.

[61] C. Adamo and V. Barone, *Toward reliable density functional methods without adjustable parameters: The PBE0 model*, The Journal of Chemical Physics 110, 6158–6170 (1999), Publisher: American Institute of Physics.

[62] J. Heyd, G. E. Scuseria, and M. Ernzerhof, *Hybrid functionals based on a screened Coulomb potential*, J. Chem. Phys. 118, 8207 (2003).

[63] J. Heyd, G. E. Scuseria, and M. Ernzerhof, *Erratum: "Hybrid functionals based on a screened Coulomb potential" [J. Chem. Phys. 118, 8207 (2003)]*, The Journal of Chemical Physics 124, 219906 (2006), Publisher: American Institute of Physics.

[64] T. M. Henderson, J. Paier, and G. E. Scuseria, *Accurate Treatment of Solids with the HSE Screened Hybrid*, Advanced Calculations for Defects in Materials, John Wiley & Sons, Ltd, 2011, Section: 6 _eprint: https://onlinelibrary.wiley.com/doi/pdf/10.1002/9783527638529.ch6, pp. 97–110.

[65] M. Marsman, J. Paier, A. Stroppa, and G. Kresse, *Hybrid functionals applied to extended systems*, Journal of Physics: Condensed Matter 20, 064201 (2008), Publisher: IOP Publishing.

[66] G. Henkelman, G. Jóhannesson, and H. Jónsson, *Methods for Finding Saddle Points and Minimum Energy Paths*, Theoretical Methods in Condensed Phase Chemistry (S. D. Schwartz, ed.), vol. 5, Kluwer Academic Publishers, Dordrecht, 2002, Series Title: Progress in Theoretical Chemistry and Physics, pp. 269–302.

[67] G. Henkelman, B. P. Uberuaga, and H. Jónsson, *A climbing image nudged elastic band method for finding saddle points and minimum energy paths*, The Journal of Chemical Physics 113, 9901–9904 (2000).

[68] *RheoMan - Nudged Elastic Band.*

[69] M. Lannoo and J. Bourgoin, *Thermodynamics of Defects*, Point Defects in Semiconductors I: Theoretical Aspects (M. Lannoo and J. Bourgoin, eds.), Springer Series in Solid-State Sciences, Springer, Berlin, Heidelberg, 1981, pp. 191–218.

[70] C. Freysoldt, B. Grabowski, T. Hickel, J. Neugebauer, G. Kresse, A. Janotti, and C. G. Van de Walle, *First-principles calculations for point defects in solids*, Reviews of Modern Physics 86, 253–305 (2014).

[71] H. V. Keer, *Principles of the solid state*, J. Wiley & Sons, New York, 1993, OCLC: 27014031.

[72] H. B. Callen, *Thermodynamics & an intr. to Thermostatistics*, Wiley India Pvt. Limited, June 2006.

[73] R. M. Nieminen, *Issues in first-principles calculations for defects in semiconductors and oxides*, Modelling and Simulation in Materials Science and Engineering 17, 084001 (2009), Publisher: IOP Publishing.

[74] B. Grabowski, T. Hickel, and J. Neugebauer, *Formation energies of point defects at finite temperatures*, physica status solidi (b) 248, 1295–1308 (2011), _eprint: https://onlinelibrary.wiley.com/doi/pdf/10.1002/pssb.201046302.

[75] J. F. Janak, *Proof that $$\frac{\partial E}{\partial n_i} = \epsilon _i$$ in density-functional theory*, Physical Review B 18, 7165–7168 (1978).

[76] J. Shim, E.-K. Lee, Y. J. Lee, and R. M. Nieminen, *Density-functional calculations of defect formation energies using supercell methods: Defects in diamond*, Physical Review B 71, 035206 (2005), Publisher: American Physical Society.

[77] P. Erhart and K. Albe, *Thermodynamics of mono- and di-vacancies in barium titanate*, Journal of Applied Physics 102, 084111 (2007).

[78] C. G. Van de Walle and J. Neugebauer, *First-principles calculations for defects and impurities: Applications to III-nitrides*, Journal of Applied Physics 95, 3851–3879 (2004), Publisher: American Institute of Physics.

[79] J. Lento, J.-L. Mozos, and R. M. Nieminen, *Charged point defects in semiconductors and the supercell approximation*, Journal of Physics: Condensed Matter 14, 2637 (2002), Publisher: IOP Publishing.

[80] G. Makov and M. C. Payne, *Periodic boundary conditions in ab initio calculations*, Physical Review B 51, 4014–4022 (1995), Publisher: American Physical Society.

[81] N. D. M. Hine, K. Frensch, W. M. C. Foulkes, and M. W. Finnis, *Supercell size scaling of density functional theory formation energies of charged defects*, Physical Review B 79, 024112 (2009), Publisher: American Physical Society.

[82] S. Lany and A. Zunger, *Assessment of correction methods for the band-gap problem and for finite-size effects in supercell defect calculations: Case studies for ZnO and GaAs*, Phys. Rev. B 78, 235104 (2008), Publisher: American Physical Society.

[83] C. Freysoldt, J. Neugebauer, and C. G. V. d. Walle, *Electrostatic interactions between charged defects in supercells*, physica status solidi (b) 248, 1067–1076 (2011).

[84] Y. Kumagai and F. Oba, *Electrostatics-based finite-size corrections for first-principles point defect calculations*, Physical Review B 89, 195205 (2014).

[85] K. J. Laidler and J. H. Meiser, *Physical chemistry*, World Student series, Benjamin/Cummings Pub. Co., Menlo Park, Calif., 1982.

[86] K. Reuter and M. Scheffler, *Composition, structure, and stability of RuO 2 (110) as a function of oxygen pressure*, Physical Review B 65, 035406 (2001).

[87] P. Erhart and K. Albe, *Modeling the electrical conductivity in BaTiO3 on the basis of first-principles calculations*, Journal of Applied Physics 104, 044315 (2008).

[88] D. R. Stull and H. Prophet, *JANAF Thermochemical Tables, 2nd ed.*, 1971.

[89] F. Bruneval and J.-P. Crocombette, *Ab initio formation volume of charged defects*, Physical Review B 86, 140103 (2012).

[90] F. Bruneval, C. Varvenne, J.-P. Crocombette, and E. Clouet, *Pressure, relaxation volume, and elastic interactions in charged simulation cells*, Physical Review B 91, 024107 (2015).

[91] C. G. Van de Walle, *Band lineups and deformation potentials in the model-solid theory*, Physical Review B 39, 1871–1883 (1989), Publisher: American Physical Society.

[92] F. Bruneval, M. Freyss, and J.-P. Crocombette, *Lattice constant in nonstoichiometric uranium dioxide from first principles*, Physical Review Materials 2, 023801 (2018).

[93] L. Koch, *First-principles study of the defect chemistry and conductivity in sodium bismuth titanate*, Ph.D. Thesis, Technische Universität, Darmstadt, 2021.

[94] G. Leibfried and N. Breuer, *Point defects in metals. I. Introduction to the theory* (1978), Publisher: Springer-Verlag New York Inc.,New York.

[95] J. F. Baumard, *Point Defects*, Concise Encyclopedia of Advanced Ceramic Materials (R. Brook, ed.), Pergamon, Oxford, January 1991, pp. 354–360.

[96] G. Brouwer, *A general asymptotic solution of reaction equations common in solid-state chemistry*, Philips Res. Rep. 9, 366–376 (1954).

[97] F. A. Kröger and H. J. Vink, *Relations between the Concentrations of Imperfections in Crystalline Solids*, Solid State Physics (F. Seitz and D. Turnbull, eds.), vol. 3, Academic Press, January 1956, pp. 307–435.

[98] H. Schmalzried, *F. A. Kröger: The Chemistry of Imperfect Crystals, North-Holland Publishing Company-Amsterdam 1964. 1039 Seiten. Preis: hfl. 110,-.*, Berichte der Bunsengesellschaft für physikalische Chemie 68, 608–608 (1964), _eprint: https://onlinelibrary.wiley.com/doi/pdf/10.1002/bbpc.19640680615.

[99] P. Canepa, G. Sai Gautam, D. Broberg, S.-H. Bo, and G. Ceder, *Role of Point Defects in Spinel Mg Chalcogenide Conductors*, Chemistry of Materials 29, 9657–9667 (2017).

[100] S. Shousha, S. Khalil, and M. Youssef, *Tuning metal oxide defect chemistry by thermochemical quenching*, Physical Chemistry Chemical Physics 22, 6308–6317 (2020).

[101] J. Lee and S. Han, *Thermodynamics of native point defects in α-Fe2O3: an ab initio study*, Physical Chemistry Chemical Physics 15, 18906 (2013).

[102] S. P. Ong, W. D. Richards, A. Jain, G. Hautier, M. Kocher, S. Cholia, D. Gunter, V. L. Chevrier, K. A. Persson, and G. Ceder, *Python Materials Genomics (pymatgen): A robust, open-source python library for materials analysis*, Computational Materials Science 68, 314–319 (2013).

[103] G. Kresse and J. Hafner, *Ab initio molecular dynamics for liquid metals*, Physical Review B 47, 558–561 (1993).

[104] G. Kresse and J. Hafner, *Ab initio molecular-dynamics simulation of the liquid-metal–amorphous-semiconductor transition in germanium*, Physical Review B 49, 14251–14269 (1994).

[105] G. Kresse and J. Furthmüller, *Efficiency of ab-initio total energy calculations for metals and semiconductors using a plane-wave basis set*, Computational Materials Science 6, 15–50 (1996).

[106] G. Kresse and J. Furthmüller, *Efficient iterative schemes for ab initio total-energy calculations using a plane-wave basis set*, Physical Review B 54, 11169–11186 (1996).

[107] L. Villa, E. Ghorbani, and K. Albe, *Role of intrinsic defects in cubic $NaNbO_3$: A computational study based on hybrid density-functional theory*, Journal of Applied Physics 131, 124106 (2022).

[108] L. Villa and K. Albe, *Role of doping and defect quenching in antiferroelectric $NaNbO_3$ from first principles*, Physical Review B 106, 134101 (2022), Publisher: American Physical Society.

[109] G. Kresse and D. Joubert, *From ultrasoft pseudopotentials to the projector augmented-wave method*, Physical Review B 59, 1758–1775 (1999).

[110] S. L. Dudarev, G. A. Botton, S. Y. Savrasov, C. J. Humphreys, and A. P. Sutton, *Electron-energy-loss spectra and the structural stability of nickel oxide: An LSDA+U study*, Physical Review B 57, 1505–1509 (1998).

[111] O. Bengone, M. Alouani, P. Blöchl, and J. Hugel, *Implementation of the projector augmented-wave LDA+U method: Application to the electronic structure of NiO*, Physical Review B 62, 16392–16401 (2000).

[112] A. V. Krukau, O. A. Vydrov, A. F. Izmaylov, and G. E. Scuseria, *Influence of the exchange screening parameter on the performance of screened hybrid functionals*, The Journal of Chemical Physics 125, 224106 (2006).

[113] F. Birch, *Finite Elastic Strain of Cubic Crystals*, Physical Review 71, 809–824 (1947).

[114] F. D. Murnaghan, *The Compressibility of Media under Extreme Pressures*, Proceedings of the National Academy of Sciences of the United States of America 30, 244–247 (1944).

[115] V. I. Anisimov, J. Zaanen, and O. K. Andersen, *Band theory and Mott insulators: Hubbard U instead of Stoner I*, Phys. Rev. B 44, 943–954 (1991), Publisher: American Physical Society.

[116] A. Jain, J. Montoya, S. Dwaraknath, N. E. R. Zimmermann, J. Dagdelen, M. Horton, P. Huck, D. Winston, S. Cholia, S. P. Ong, and K. Persson, *The Materials Project: Accelerating Materials Design Through Theory-Driven Data and Tools*, Handbook of Materials Modeling (W. Andreoni and S. Yip, eds.), Springer, Cham, Cham, 2018, pp. 1–34.

[117] S. P. Ong, S. Cholia, A. Jain, M. Brafman, D. Gunter, G. Ceder, and K. A. Persson, *The Materials Application Programming Interface (API): A simple, flexible and efficient API for materials data based on REpresentational State Transfer (REST) principles*, Computational Materials Science 97, 209–215 (2015).

[118] P. Li, S. Ouyang, G. Xi, T. Kako, and J. Ye, *The Effects of Crystal Structure and Electronic Structure on Photocatalytic H_2 Evolution and CO_2 Reduction over Two Phases of Perovskite-Structured $NaNbO_3$*, The Journal of Physical Chemistry C 116, 7621–7628 (2012).

[119] A. Stukowski, *Visualization and analysis of atomistic simulation data with OVITO–the Open Visualization Tool*, Modelling and Simulation in Materials Science and Engineering 18, 015012 (2010).

[120] B. Yang, J. Bian, L. Wang, J. Wang, Y. Du, Z. Wang, C. Wu, and Y. Yang, *Enhanced photocatalytic activity of perovskite $NaNbO_3$ by oxygen vacancy engineering*, Physical Chemistry Chemical Physics 21, 11697–11704 (2019).

[121] A. Shigemi and T. Wada, *Enthalpy of Formation of Various Phases and Formation Energy of Point Defects in Perovskite-Type $NaNbO_3$ by First-Principles Calculation*, Japanese Journal of Applied Physics 43, 6793–6798 (2004).

[122] S. P. Ong, L. Wang, B. Kang, and G. Ceder, *Li-Fe-P-O $_2$ Phase Diagram from First Principles Calculations*, Chemistry of Materials 20, 1798–1807 (2008).

[123] M.-H. Zhang, C. Zhao, L. Fulanović, J. Rödel, N. Novak, A. Schökel, and J. Koruza, *Revealing the mechanism of electric-field-induced phase transition in antiferroelectric NaNbO $_3$ by in situ high-energy x-ray diffraction*, Applied Physics Letters 118, 132903 (2021).

[124] C. N. W. Darlington and H. D. Megaw, *The low-temperature phase transition of sodium niobate and the structure of the low-temperature phase, N*, Acta Crystallographica Section B Structural Crystallography and Crystal Chemistry 29, 2171–2185 (1973).

[125] P. Seidel and W. . Hoffmann, *Verfeinerung der Kristallstruktur von NaNbO $_3$ N. Bestimmung der absoluten Konfiguration und des Zwillingsgesetzes*, Zeitschrift für Kristallographie - Crystalline Materials 143, 444–459 (1976).

[126] X. Ren, *Large electric-field-induced strain in ferroelectric crystals by point-defect-mediated reversible domain switching*, Nature Materials 3, 91–94 (2004).

[127] S. Egert, M.-H. Zhang, J. Koruza, P. B. Groszewicz, and G. Buntkowsky, *23Na NMR Spectroscopic Quantification of the Antiferroelectric–Ferroelectric Phase Coexistence in Sodium Niobate*, The Journal of Physical Chemistry C 124, 23852–23858 (2020), Publisher: American Chemical Society.

[128] N. Bein, B. Kmet, T. Rojac, A. B. Golob, B. Malič, J. Moxter, T. Schneider, L. Fulanovic, M. Azadeh, T. Frömling, S. Egert, H. Wang, P. van Aken, J. Schwarzkopf, and A. Klein, *Fermi energy, electrical conductivity, and the energy gap of ${\mathrm{NaNbO}}_{3}$*, Physical Review Materials 6, 084404 (2022), Publisher: American Physical Society.

[129] Z. Liu and B.-X. Xu, *Insight into perovskite antiferroelectric phases: Landau theory and phase field study*, Scripta Materialia 186, 136–141 (2020).

[130] A. Shigemi and T. Wada, *Crystallographic phase stabilities and electronic structures in AgNbO $_3$ by first-principles calculation*, Molecular Simulation 34, 1105–1114 (2008).

[131] H. Moriwake, C. A. J. Fisher, A. Kuwabara, and D. Fu, *First-Principles Study of Point Defect Formation in AgNbO3*, Japanese Journal of Applied Physics 52, 09KF08 (2013).

[132] M. Valant, A.-K. Axelsson, B. Zou, and N. Alford, *Oxygen transport during formation and decomposition of AgNbO3 and AgTaO3*, Journal of Materials Research 22, 1650–1655 (2007).

[133] E. Ghorbani, L. Villa, P. Erhart, A. Klein, and K. Albe, *Self-consistent calculations of charge self-trapping energies: A comparative study of polaron formation and migration in $PbTiO_3$*, Physical Review Materials 6, 074410 (2022), Publisher: American Physical Society.

[134] M.-H. Zhang, H. Ding, S. Egert, C. Zhao, L. Villa, L. Fulanović, P. B. Groszewicz, G. Buntkowsky, H.-J. Kleebe, K. Albe, A. Klein, and J. Koruza, *Tailoring high-energy storage $NaNbO_3$-based materials from antiferroelectric to relaxor states*, Nature Communications 14, 1525 (2023), Number: 1 Publisher: Nature Publishing Group.